

Bioinspired Functional Materials

Guest Editors: Yongmei Zheng, Jingxia Wang, Yongping Hou, Hao Bai, and Michael Z. Hu





Bioinspired Functional Materials

Journal of Nanomaterials

Bioinspired Functional Materials

Guest Editors: Yongmei Zheng, Jingxia Wang, Yongping Hou,
Hao Bai, and Michael Z. Hu



Copyright © 2014 Hindawi Publishing Corporation. All rights reserved.

This is a special issue published in "Journal of Nanomaterials." All articles are open access articles distributed under the Creative Commons Attribution License, which permits unrestricted use, distribution, and reproduction in any medium, provided the original work is properly cited.

Editorial Board

Katerina E. Aifantis, USA
Nageh K. Allam, USA
Margarida Amaral, Portugal
Xuedong Bai, China
Lavinia Balan, France
Enrico Bergamaschi, Italy
Theodorian Borca-Tasciuc, USA
C. Jeffrey Brinker, USA
Christian Brosseau, France
Xuebo Cao, China
Shafiq Chowdhury, USA
Kwang-Leong Choy, UK
Cui ChunXiang, China
Miguel A. Correa-Duarte, Spain
Shadi A. Dayeh, USA
Ali Eftekhari, USA
Claude Estourns, France
Alan Fuchs, USA
Lian Gao, China
Russell E. Gorga, USA
Hongchen Chen Gu, China
Mustafa O. Guler, Turkey
John Z. Guo, USA
Smrati Gupta, Germany
Michael Harris, USA
Zhongkui Hong, China
Michael Z. Hu, USA
David Hui, USA
Y.-K. Jeong, Republic of Korea
Sheng-Rui Jian, Taiwan
Wanqin Jin, China
Rakesh K. Joshi, UK
Zhenhui Kang, China
Fathallah Karimzadeh, Iran
Alireza Khataee, Iran

Do Kyung Kim, Korea
Alan K. T. Lau, Hong Kong
Burtrand Lee, USA
Jun Li, Singapore
Benxia Li, China
Xing-Jie Liang, China
Shijun Liao, China
Gong-Ru Lin, Taiwan
Tianxi Liu, China
Jun Liu, USA
Songwei Lu, USA
Daniel Lu, China
Jue Lu, USA
Ed Ma, USA
Gaurav Mago, USA
Santanu K. Maiti, India
Sanjay R. Mathur, Germany
Vikas Mittal, UAE
Weihai Ni, China
Sherine Obare, USA
Atsuto Okamoto, Japan
Abdelwahab Omri, Canada
Edward A. Payzant, USA
Kui-Qing Peng, China
Anukorn Phuruangrat, Thailand
Mahendra Rai, India
Suprakas Sinha Ray, South Africa
Ugur Serincan, Turkey
Huaiyu Shao, Japan
Donglu Shi, USA
Vladimir Sivakov, Germany
Marinella Striccoli, Italy
Bohua Sun, South Africa
Saikat Talapatra, USA
Nairong Tao, China

Titipun Thongtem, Thailand
Somchai Thongtem, Thailand
Alexander Tolmachev, Ukraine
Valeri P. Tolstoy, Russia
Tsung-Yen Tsai, Taiwan
Takuya Tsuzuki, Australia
Raquel Verdejo, Spain
Mat U. Wahit, Malaysia
Zhenbo Wang, China
Ruiping Wang, Canada
Shiren Wang, USA
Cheng Wang, China
Yong Wang, USA
Jinquan Wei, China
Ching-Ping Wong, Hong Kong
Xingcai Wu, China
Guodong Xia, Hong Kong
Ping Xiao, UK
Zhi Li Xiao, USA
Yangchuan Xing, USA
Shuangxi Xing, China
Nanping Xu, China
Doron Yadlovker, Israel
Yingkui Yang, China
Khaled Youssef, USA
Kui Yu, Canada
William W. Yu, USA
Haibo Zeng, China
Tianyou Zhai, China
Bin Zhang, China
Renyun Zhang, Sweden
Yanbao Zhao, China
Lianxi Zheng, Singapore
Chunyi Zhi, Hong Kong

Contents

Bioinspired Functional Materials, Yongmei Zheng, Jingxia Wang, Yongping Hou, Hao Bai, and Michael Z. Hu
Volume 2014, Article ID 986815, 2 pages

Scaffolding Biomaterials for Cartilage Regeneration, Zhen Cao, Ce Dou, and Shiwu Dong
Volume 2014, Article ID 489128, 8 pages

Bioactivity Assessment of Poly(ϵ -caprolactone)/Hydroxyapatite Electrospun Fibers for Bone Tissue Engineering Application, Mohd Izzat Hassan, Naznin Sultana, and Salehuddin Hamdan
Volume 2014, Article ID 573238, 6 pages

Structure and Identification of Solenin: A Novel Fibrous Protein from Bivalve *Solen grandis* Ligament, Jun Meng, Gang-Sheng Zhang, and Zeng-Qiong Huang
Volume 2014, Article ID 241975, 7 pages

Alumina Membrane with Hour-Glass Shaped Nanochannels: Tunable Ionic Current Rectification Device Modulated by Ions Gradient, Shengnan Hou, Qinqin Wang, Xia Fan, Zhaoyue Liu, and Jin Zhai
Volume 2014, Article ID 564694, 10 pages

Fabrication of Phase-Change Polymer Colloidal Photonic Crystals, Tianyi Zhao, Youzhan Zhang, Jingxia Wang, Yanlin Song, and Lei Jiang
Volume 2014, Article ID 702089, 7 pages

The Effect of Silver Nanofibers on the Deformation Properties of Blood Vessels: Towards the Development of New Nanotechnologies to Prevent Rupture of Aneurysms, Miguel Gonzalez, Daniel Rivera, Alam Marcelino, Gabriela Agront, Rafael Rodriguez, and Miguel Castro
Volume 2014, Article ID 853120, 8 pages

Visualization of Iron-Binding Micelles in Acidic Recombinant Biom mineralization Protein, MamC, Sanjay Kashyap, Taylor Woehl, Carmen Valverde-Tercedor, Miguel Sánchez-Quesada, Concepción Jiménez López, and Tanya Prozorov
Volume 2014, Article ID 320124, 7 pages

The Promotion of Human Neural Stem Cells Adhesion Using Bioinspired Poly(norepinephrine) Nanoscale Coating, Minah Park, Mikyung Shin, Eunmi Kim, Slgirim Lee, Kook In Park, Haeshin Lee, and Jae-Hyung Jang
Volume 2014, Article ID 793052, 10 pages

Preparation of Amino-Modified PAN Fibers with Triethylenetetramine as Aminating Reagents and Their Application in CO₂ Adsorption, Wenbo Zhao, Biao Liu, and Jian Chen
Volume 2014, Article ID 940908, 7 pages

Variable Responsive Wettability Films via Electrospinning Induced by Solvents, Nü Wang, Fengyun Guo, Jing Wu, Yong Zhao, and Lei Jiang
Volume 2014, Article ID 817418, 7 pages

Editorial

Bioinspired Functional Materials

Yongmei Zheng,¹ Jingxia Wang,² Yongping Hou,¹ Hao Bai,³ and Michael Z. Hu⁴

¹ Key Laboratory of Bio-Inspired Smart Interfacial Science and Technology of Ministry of Education, School of Chemistry and Environment, Beihang University, Xueyuan Road 37, Haidian District, Beijing 100191, China

² Key Laboratory of Green Printing, Institute of Chemistry, Chinese Academy of Sciences, Beijing 100190, China

³ Lawrence Berkeley National Laboratory, 1 Cyclotron Road, MS 62-0227, Berkeley, CA 94720, USA

⁴ Oak Ridge National Laboratory, Oak Ridge, TN 37831, USA

Correspondence should be addressed to Yongmei Zheng; zhengym@buaa.edu.cn

Received 20 October 2014; Accepted 20 October 2014; Published 25 November 2014

Copyright © 2014 Yongmei Zheng et al. This is an open access article distributed under the Creative Commons Attribution License, which permits unrestricted use, distribution, and reproduction in any medium, provided the original work is properly cited.

This special issue is focused on the nanoscale or micro-/nanoscale structures similar to the biological features in multilevels or hierarchy and so on. Research by mimicking biological systems has shown more impact on many applications due to the well-designed micro-/nanostructures inspired from the biological surfaces or interfaces; thus, the materials may achieve the fascinating functionality. The bioinspired functional materials may be fabricated by developing novel technology or methods such as synthesis, self-assembly, and soft lithography at micro- or nanolevel or multilevels and, in addition, the multidisciplinary procedures of physical or chemical methods and nanotechnology to mimic the biological multiscale micro-/nanostructures onto one-/two-dimensional surface materials.

This issue collected these researched works from biological to bioinspired materials as follows.

J. Meng et al. revealed the microstructure of a novel fibrous protein: solenin from *Solen grandis* ligament and identified the protein by MALDI-TOF-TOF-MS and LC-MS-MS analyses and found that the protein fiber has no hierarchical structure and is homologous to keratin type II cytoskeletal 1 and type I cytoskeletal 9-like, containing “SGGG,” “SYGSGGG,” “GS,” and “GSS” repeat sequences; the β -sheet structure and those repeat sequences which form “glycine loops” may give solenin excellent elastic and flexible properties to withstand tensile stress caused by repeating opening and closing of the shell valves in vivo. This paper contributes a novel fibrous protein for the protein materials world.

S. Kashyap et al. reported the in situ visualization of a novel acidic bacterial recombinant protein, MamC,

commonly present in the magnetosome membrane of several magnetotactic bacteria, including *Magnetococcus marinus*, strain MC-1. The findings provided an insight into the self-assembly of MamC and point to formation of the extended protein surface, which is assumed to play an important role in the formation of biotemplated inorganic nanoparticles. The self-organization of MamC is compared to the behavior of another acidic recombinant iron-binding protein, Mms6.

Z. Cao et al. reviewed the article on scaffolding biomaterials for cartilage regeneration. The use of tissue engineering approach in which scaffolds play a vital role to regenerate cartilage has become a new research field. Investigating the advances in biological cartilage scaffolds has been regarded as the main research direction and has great significance for the construction of artificial cartilage. Native biological materials and synthetic polymeric materials have their advantages and disadvantages. The disadvantages can be overcome through either physical modification or biochemical modification. Additionally, developing composite materials, biomimetic materials, and nanomaterials can make scaffolds acquire better biocompatibility and mechanical adaptability.

S. Hou et al. reported a new alumina membrane with hour-glass shaped nanochannels by using the double-side anodization method and the subsequently in situ pore opening procedure, which is applied to develop the tunable ionic current rectification devices that were modulated by ions gradient. By regulating the pH gradient, tunable ionic current rectification properties which are mainly dependent on the asymmetric surface charge density or polarity distribution on the inner walls of the nanochannels can be obtained. Such specific alumina nanochannels would be considered as

a promising candidate for building bioinspired artificial ion channel systems.

M. I. Hassan et al. reported the bioactivity assessment of poly (ϵ -caprolactone)/hydroxyapatite electrospun fibers for bone tissue engineering application. The fiber diameter is entangled by the concentration of PCL with some adjustment of parameters during electrospinning process. PCL with lower concentration had bead structure while higher concentration had smooth fiber. The fiber diameter of PCL was increased with the addition of nHA. The immersion of PCL/nHA fiber in simulated body fluid (SBF) had bonelike apatite layer on its surface while PCL showed no results. PCL/nHA showed high water uptake and had improved wettability compared to PCL alone, suggesting that PCL/nHA fibers were more hydrophilic than PCL fiber.

T. Zhao et al. presented the preparation of phase-change polymer colloidal photonic crystals (PCs) by assembling hollow latex spheres encapsulated with dodecanol for the first time. The monodispersed hollow latex spheres were obtained by phase reversion of monodispersed core-shell latex spheres in the n-hexane, which dissolves the PS core and retains the PMMA/PAA shell. The as-prepared phase-change colloidal PCs show stable phase-change behavior. This fabrication of phase-change colloidal PCs would be significant for PC's applications in functional coatings and various optic devices.

M. Park et al. reported a method of creating a biomimetic functional biointerface which was introduced to enhance human neural stem cell (hNSC) adhesion. The hNSC-compatible biointerface was prepared by the oxidative polymerization of the neurotransmitter norepinephrine, which generates a nanoscale organic thin layer, termed poly (norepinephrine) (pNE). The pNE-coated biointerfaces provided a highly favorable microenvironment for hNSCs, with no observed cytotoxicity. The adhesive properties of pNE interfaces led to micropatterns of cellular attachment, thereby demonstrating the ability of the interface to organize the stem cells. This highly facile surface-modification method using a biomimetic pNE thin layer can be applied to a number of suitable materials that were previously not compatible with hNSC technology.

N. Wang et al. reported variable responsive wettability films via electrospinning induced by solvents. The three kinds of interesting distinct wettability films are fabricated by a facile electrospinning technique. The films are composites of poly(N-isopropylacrylamide) and polystyrene but different precursor solvents. By taking advantage of the conformational changes of poly(N-isopropylacrylamide) chains and polystyrene chains in different solvents, the films exhibit responsive wettability variation to temperature.

M. Gonzalez et al. reported the effect of silver nanofibers on the deformation properties of blood vessels: towards the development of new nanotechnologies to prevent rupture of aneurysms. They proposed an innovative approach to prevent the rupture of an aneurysm based on the use of nanotechnology to improve the strength of the blood vessel. They presented results on the effect of silver nanofibers on the resistance toward deformation of blood vessels. The silver nanofibers are grown on the surface of the blood vessels. Treatment of blood vessels with silver nanofibers is

a potential translational clinical tool for preventing rupture of aneurysms in a clinical setting.

W. Zhao et al. prepared the preparation of amino-modified PAN fibers with triethylenetetramine as aminating reagents and their application in CO₂ adsorption. The amino-modified polyacrylonitrile (AMPAN) fiber was synthesized by the reaction of polyacrylonitrile (PAN) fiber and triethylenetetramine (TETA) in the presence of water. The effect of water amount, reaction temperature, and time on the weight increase degree and alkali content of the AMPAN fiber was investigated in detail. The characterization results indicated that TETA could be grafted onto the surface of PAN fiber by this method.

Acknowledgments

The editors thank the authors for their efforts and time spent for each manuscript. The lead editor thanks all editors for the time spent in reviewing, assigning reviews, and commenting on submitted manuscripts. The editors hope that this special issue will be useful to investigators in interfacial functional materials.

*Yongmei Zheng
Jingxia Wang
Yongping Hou
Hao Bai
Michael Z. Hu*

Review Article

Scaffolding Biomaterials for Cartilage Regeneration

Zhen Cao,¹ Ce Dou,^{1,2} and Shiwu Dong¹

¹ Department of Biomedical Materials Science, School of Biomedical Engineering, Third Military Medical University, Chongqing 400038, China

² National & Regional United Engineering Laboratory of Tissue Engineering, Department of Orthopedics, Southwest Hospital, Third Military Medical University, Chongqing 400038, China

Correspondence should be addressed to Shiwu Dong; dongshiwu@163.com

Received 22 May 2014; Revised 26 June 2014; Accepted 2 July 2014; Published 15 July 2014

Academic Editor: Hao Bai

Copyright © 2014 Zhen Cao et al. This is an open access article distributed under the Creative Commons Attribution License, which permits unrestricted use, distribution, and reproduction in any medium, provided the original work is properly cited.

Completely repairing of damaged cartilage is a difficult procedure. In recent years, the use of tissue engineering approach in which scaffolds play a vital role to regenerate cartilage has become a new research field. Investigating the advances in biological cartilage scaffolds has been regarded as the main research direction and has great significance for the construction of artificial cartilage. Native biological materials and synthetic polymeric materials have their advantages and disadvantages. The disadvantages can be overcome through either physical modification or biochemical modification. Additionally, developing composite materials, biomimetic materials, and nanomaterials can make scaffolds acquire better biocompatibility and mechanical adaptability.

1. Introduction

Articular cartilage belongs to hyaline cartilage which is avascular and low metabolic. So repairing of cartilage damage resulting from trauma or degeneration has been a thorny clinical issue [1]. Current treatments used in small cartilage defects repairing include multiple drilling, abrasion arthroplasty, mosaicplasty, and autogenous and allogeneic chondrocyte transplantation. Several disadvantages of allograft use include disease transmission, immune reaction, and slower remodeling. Likewise, autograft also has its disadvantages for its requirements of the patient to undergo many surgeries [2]. The rise of tissue engineering in which three basic elements are cells, biodegradable scaffolds, and growth factors provides a new choice for the repair of articular cartilage [3].

In cartilage tissue engineering, scaffolds can provide three-dimensional structure for cartilage cells and be in favor of cell adhesion and proliferation [4]. More importantly, they mediate cell-cell signaling and interaction. However, the physical and biochemical properties are crucial for the scaffolds on the entire cartilage repair process [5].

2. Current Classification and Basic Requirements of Scaffolds

Currently matrix materials suitable for cells can be divided into native biological materials and synthetic polymeric materials [6]. Collagen is a kind of native biological materials with excellent tissue compatibility, little toxicity, and facile biodegradation; meanwhile its degradation products are absorbed facilely without inflammation. Fibrin originates from blood without immunogenicity. So it is widely applied in clinical treatment. Besides its excellent biocompatibility, fibrin can effectively promote the adhesion of chondrocytes. But their common drawbacks, such as weak mechanical properties and unstable degradation rate, limit its application in tissue engineering. Synthetic polymeric material can be molded easily whose microstructure, mechanical properties and degradation can be designed. With its fine biocompatible property, poly (lactic-co-glycolic acid) (PLGA) and polymer of lactic acid (PLA) are widely used in tissue engineering for cartilage. However, as synthetic materials, they are expensive and have weak cell adhesive ability. Polycaprolactone

(PCL) can maintain phenotype and promote chondrocytes proliferation. The most significant advantages of PCL are slow degradation rate and high drug permeability. But it also has drawbacks such as poor hydrophilicity and acidic degradation products which may cause inflammation [7].

Ideal scaffolds for cartilage tissue engineering should be satisfied with the following basic requirements: biocompatible, biodegradable, highly porous, suitable for cell attachment, proliferation and differentiation, osteoconductive, noncytotoxic, flexible and elastic, and nonantigenic [8].

3. Material Modification and Process

The characteristics of native biological materials and synthetic polymeric materials have been described above. Composite materials are currently applied to overcome the disadvantages of single materials [9]. The materials can also be modified by physical and biochemical methods to retain their advantages and overcome their shortcomings [10, 11]. According to recent studies, the scaffold processed into biomimetic materials and nanomaterials is the new trend [12–15] as shown in Figure 1.

3.1. Physical Modification. Physical modification refers to modification of scaffolds by physical methods such as compression, filtration, and ultraviolet light irradiation to improve the porosity and biomechanical property of materials and ultimately contribute to cartilage repair. Cartilage-derived matrix (CDM) scaffold that mimics chondroinductive environment is a type of acellular matrix material [21]. But it is disappointing to find the scaffolds contract during *in vitro* culture, thus affecting the results of tissue engineering cartilage repair. After treated with dehydrothermal (DHT) or ultraviolet light irradiation (UV), CDM scaffold not only can prevent cell-mediated contraction but also can support cell attachment [16]. Collagen gel as matrix scaffold has become a clinically applicable treatment for focal defects of articular cartilage. However, its biomechanical property is still not satisfying [22]. Compression and filtration make it acquire a higher force carrying capacity. Meanwhile, condensed collagen gel is also suitable for three-dimensional autologous chondrocyte implantation [17]. Another study found that different collagen scaffold structures may provide different immunogenicity. And hydrogels that can avoid severe immune rejection were found to be a promising scaffold structure [23]. Due to the excellent biocompatibility and suitability for cell attachment, alginate scaffold has been applied in cartilage tissue engineering. Recently, Wang et al. [18] produced a highly organized alginate scaffold to improve interconnected porous structure and porosity by microfluidic device. They seeded chondrocytes in the scaffold and found that cells can maintain normal phenotypes, highly express aggrecan and type II collagen, and secrete a great deal of extracellular matrix. The structure of a cartilage scaffold is required to mimic native articular cartilage, which has an oriented structure associated with its mechanical function. Oriented extracellular matrix- (ECM-) derived scaffolds enhance the biomechanical property of tissue engineering cartilage and oriented poly PLGA scaffolds efficiently promotes

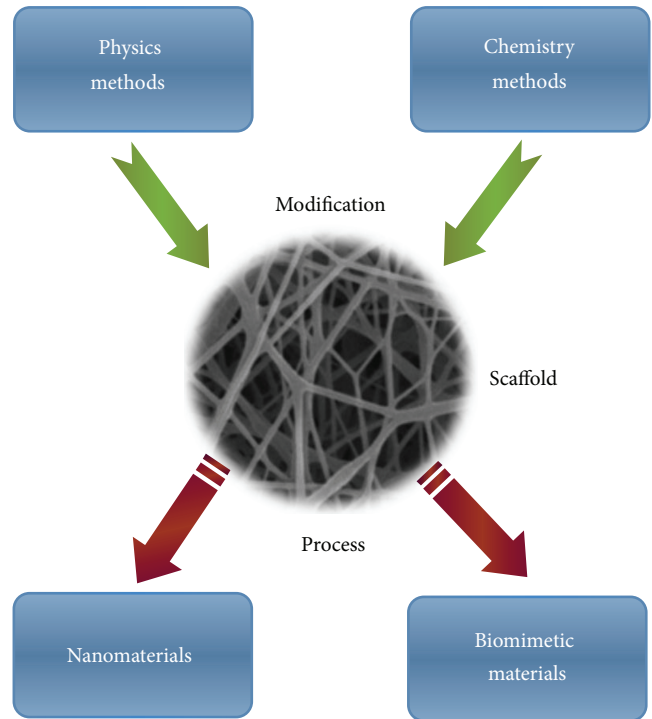


FIGURE 1: The materials can be modified by physical and biochemical methods and processed into biomimetic materials and nanomaterials to retain their advantages and overcome their shortcomings.

cell migration thus probably contributes to improving tissue regeneration [19, 20]. An overview of the physical modification on scaffolds is shown in Table 1.

3.2. Biochemical Modification. The weak mechanical property is the most serious problem of native biological materials. As for synthetic polymeric material, its drawbacks are poor hydrophilicity and weak cell adhesive ability [37]. However, scaffolds can be combined with biological modifier which is called biochemical modification to overcome the problems above. In other words, biochemical modification is introduced in the original material to make scaffolds have better tissue compatibility and provide appropriate microenvironment for cell growth and proliferation as shown in Table 2.

3.2.1. Surface Peptide. Peptide is a promising bioactive molecule to improve chondrogenesis in porous biomaterials. Mesenchymal stem cells- (MSCs-) affinity EPLQLKM peptide (E7) was covalently conjugated onto PCL which is implanted into a cartilage defect site of rat knee joints with endogenous MSCs. After 7 d of implantation, the results suggested that the E7 peptide sequence has a high specific affinity to MSCs and enhances the MSCs recruitment of PCL *in vivo* [24]. Another study investigated the generation of tissue engineering cartilage in TATVHL peptide-grafted polyethylene oxide/chitin/chitosan scaffold in which bovine knee chondrocytes were seeded. The results demonstrated that TATVHL peptide-grafted construct improved the proliferation of chondrocytes in constructs, the secretion of glycosaminoglycans, and the production of collagen [25].

TABLE 1: Physical modification on scaffolds.

Scaffolds	Methods	Effect	References
Cartilage-derived matrix scaffolds	Dehydrothermal treatment ultraviolet light irradiation	Make chondrocytes to produce higher glycosaminoglycan and collagen contents and support cell attachment	Rowland et al., 2013 [16]
Collagen type-I gel	Compression and filtration	Improve the biomechanical and biochemical properties of scaffold	Mueller-Rath et al., 2010 [17]
Alginate scaffold	Microfluidic technology	Enable the scaffold to have a regular interconnected porous structure and high porosity	Wang et al., 2011 [18]
PLGA	Scaffold orientation	Promote cell migration and improve the mechanical property of engineered cartilage	Zhang et al., 2012 [19]
Cartilage extracellular matrix	Scaffold orientation	Enhance the biomechanical property of engineered cartilage	Jia, et al., 2012 [20]

PLGA: poly(lactic-co-glycolic acid).

TABLE 2: Biochemical modification on scaffolds.

Modifier	Scaffolds	Effect	References
Surface peptide	PCL	Enhance the MSCs recruitment and provide a high specific affinity to MSCs	Shao et al., 2012 [24]
	Polyethylene oxide/chitin/chitosan	Enhance the adhesion and proliferation of bovine knee chondrocytes	Kuo and Wang, 2012 [25]
	PEO/chitosan scaffolds	Stimulate chondrogenesis with enhanced quantities of BCCs, glycosaminoglycans (GAGs), and collagen	Kuo and Wang, 2011 [26]
Bioglass	Agarose scaffolds	Improve the biochemical and mechanical properties of a tissue-engineered cartilage layer	Jayabalan et al., 2011 [27]
	PHBV	Improve the hydrophilicity of scaffolds and promote cell migration into the inner part of the constructs	Wu et al., 2013 [28]
Hyaluronic acid	Silk fibroin scaffolds	Protect the chondral phenotype and improve the structural and physical properties of scaffolds	Foss et al., 2013 [29]
	Gelatin-methacrylamide	Enhance the natural functions of scaffolds in cartilage mechanical and geometrical properties	Schuurman et al., 2013 [30]
	PLGA	Provide appropriate mechanical and structural properties of scaffolds for cells	Chang et al., 2013 [31]
	Collagen scaffolds	Improve cellular infiltration and promotes early-stage chondrogenesis	Matsiko et al., 2012 [32]
Chitosan	PLCL	Improve cells compatibility and form better quality cartilage tissue	Yang et al., 2012 [33]
	PLCL	Promote cell adhesion and proliferation and enhance excretion of aggrecan and type-II collagen	Li et al., 2012 [34]
	Silk fibroin scaffolds	Serve as excellent carrier for stem cells to repair cartilage defects	Deng et al., 2013 [35]
	Gelatin scaffolds	Enhance the cartilage regeneration in vitro and in vivo	Whu et al., 2013 [36]

PCL: polycaprolactone; MSCs: mesenchymal stem cells; PEO: polyethylene oxide; PHBV: polyhydroxybutyrate valerate; PLGA: poly(lactic-co-glycolic acid); PLCL: poly l-lactide-co- ϵ -caprolactone.

Surface CDPGYIGSR was grafted via cross-linking onto polyethylene oxide (PEO) and chitosan scaffold. After seeding of bovine knee chondrocytes (BKC) in the scaffolds, the constructs were cultured in a spinner system, indicating that the adhesion of BKC and the maintenance of phenotypic chondrocytes were more efficient [26].

3.2.2. Bioglass. Bioglass is a sort of glass which possesses particular biological and physiological functions. After implanted into osteochondral defects, bioglass directly combines with the host tissue, playing the role of tissue repairing and restoring. When used as a subchondral substrate, bioactive glass (BG) 13-93 did not improve biochemical properties of scaffolds. However, as a culture medium supplement, BG 13-93 improved the biochemical and mechanical properties of a tissue-engineered cartilage layer. BG 13-93 may be suitable as a medium supplement for neocartilage formation [27]. Another research compared the effects of PHBV scaffolds and PHBV/BG composite scaffolds on the properties of engineered cartilage *in vivo*. The results showed that the incorporation of BG into PHBV efficiently improved both the hydrophilicity of the composites and the percentage of adhered cells and promoted cell migration into the inner part of the constructs [28].

3.2.3. Hyaluronic Acid. As a sort of acidic mucopolysaccharides, hyaluronic acid displayed a variety of important physiological functions due to its unique molecular structure and physicochemical properties such as lubricating joints, regulating vascular permeability, and promoting repair in trauma. More importantly, hyaluronic acid called natural moisturizing factor has such special role of water retention that it has important applications in cartilage tissue engineering scaffolds. Among biomaterials proposed for cartilage repair, silk fibroin (SF) has been recently proposed as a material template for porous scaffolds cultured with chondrocytes and investigated under static and dynamic conditions. The combination of hyaluronic acid (HA) with silk fibroin scaffolds can protect the chondral phenotype and improve the structural and physical properties of scaffolds [29]. Gelatin-methacrylamide (gelMA) hydrogels were shown to support chondrocyte viability and differentiation. However, incorporation of HA allows gelMA to match the natural functions of scaffolds in cartilage mechanical and geometrical properties [30]. Another group fabricated gelatin/hyaluronic acid-treated PLGA (PLGA-GH) sponge scaffolds for articular cartilage tissue engineering. The results showed that cells attachment ratio, proliferation, and extracellular matrix secretion on PLGA-GH scaffolds were superior to those of PLGA scaffolds [31]. Collagen-glycosaminoglycan (CG) scaffolds have been extensively applied in a range of tissue engineering successfully. It is well known that there are two types of glycosaminoglycan: chondroitin sulphate (CS) and hyaluronic acid. Compared to collagen-CS scaffolds, collagen-HA scaffolds showed significant acceleration of early-stage gene expression of SOX-9 and collagen type II as well as cartilage matrix production. The results demonstrated that collagen-HA scaffolds own great potential as appropriate matrices for promoting cartilage tissue repair [32].

3.2.4. Chitosan. Because of the excellent biocompatibility, chitosans have been widely utilized in the field of biomedical materials, such as artificial skin [38], absorbable sutures, hemostatic sponge, and antiadhesion agent. Moreover, chitosans not only can provide appropriate microenvironment for cartilage regeneration but can also stimulate cell proliferation and promote tissue repairing through varieties of ways. A porous elastomeric poly l-lactide-co- ϵ -caprolactone (PLCL) was generated and cross-linked at the surface to chitosan to improve its wettability. Bone marrow-derived mesenchymal stem cells (BMSCs) were seeded in the constructs to evaluate attachment, morphological change, and proliferation. The results showed that chitosan modification of the PLCL scaffold improved cell compatibility without significant alteration of the physical elastomeric properties of PLCL and resulted in formation of cartilage tissue with better quality [33]. Coincidentally, another study fabricated chitosan-modified poly PLCL scaffolds to simulate the main biochemical components of cartilage, which revealed that the chitosan-modified PLCL scaffolds not only could promote cell adhesion and proliferation, but also could significantly enhance excretion of aggrecan and type-II collagen [34]. In addition to synthetic scaffolds, chitosans can also improve natural materials such as gelatin and silk fibroin scaffolds. BMSCs were seeded in a three-dimensional scaffold of SF and chitosan to repair cartilage defects in the rabbit knee, which indicated that SF/chitosan scaffold can serve as excellent carriers for stem cells to repair cartilage defects [35]. In addition, chitosan-gelatin (1:1) complex scaffolds cross-linked by water-soluble carbodiimide (WSC) may enhance cartilage regeneration [36].

3.3. Nanomaterials. Nanomaterials have recently attracted considerable attention because of its high surface-to-volume ratio. Nanomaterials provide a new space for seed cells with a wide range of applications in cartilage tissue engineering. The annulus fibrosus comprises concentric lamellae that can be damaged due to intervertebral disc degeneration. Electrospun nanofibrous scaffolds of polycaprolactone are fabricated in random, aligned, and round-ended configurations to support the growth of annulus fibrosus cells. Primary porcine annulus fibrosus cells are grown on the scaffolds and the results demonstrated that the scaffolds are favorable to attachment, proliferation, and production of extracellular matrix of cells. In addition, the scaffold consisting of round-ended nanofibers substantially outperforms the random and aligned scaffolds on cell adhesion while aligned nanofibers strongly effect the orientation of cells [43]. The menisci are crescent-shaped fibrocartilaginous tissues whose structural organization consists of dense collagen bundles that are locally aligned but show a continuous change in macroscopic directionality. A novel electrospinning method to produce scaffolds composed of circumferentially aligned (CircAl) nanofibers was developed. The results showed these novel scaffolds, with spatially varying local orientations and mechanics, enabled the formation of functional anatomic meniscus constructs [44]. Aligned nanofibrous scaffolds can dictate cell and matrix organization. However, their widespread application has been hindered by poor cell infiltration due to the

TABLE 3: Proteins, drugs, or cytokine embedded in biomimetic scaffolds.

Embedding	Scaffolds	Effect	References
Antiangiogenic drug	Fibrin/hyaluronan	Block host vessels ingrowth and enhance constructs survival rate	Centola et al., 2013 [39]
Parathyroid hormone-related protein	Collagen-silk	Inhibit terminal differentiation of chondrocytes and enhance chondrogenesis	Zhang et al., 2013 [40]
Transforming growth factor- β 1	Poly(L-lactide)	Induce an anabolic stimulus on AFCs and mimic the ECM three-dimensional environment of AF tissue	Vadalà et al., 2012 [41]
Cadherin-11	Collagen type II sponges	Promote adhesion of chondrocytes and stimulate chondrogenic differentiation	Dong et al., 2013 [42]

AFCs: annulus fibrosus cells; ECM: extracellular matrix.

tight packing of fibers during fabrication. Containing two distinct fiber fractions: slow-degrading poly (ϵ -caprolactone) and water-soluble, sacrificial poly (ethylene oxide) can be selectively removed to increase pore size; tunable composite nanofibrous scaffolds are produced. It is found that increasing the initial fraction of sacrificial poly (ethylene oxide) fibers enhanced cell infiltration and improved matrix distribution [45].

Biochemical modification of nanomaterials will make scaffolds more biocompatible and bioactive. A new functionalized peptide RLN was designed containing the bioactive motif link N and the amino terminal peptide of link protein. A link N nanofiber scaffold (LN-NS) was self-assembled by mixing peptide solution of RLN. This designer functionalized nanofiber scaffold exhibited little cytotoxicity and promoted nucleus pulposus cells (NPCs) adhesion. Besides, it also stimulated the biosynthesis of ECM by NPCs [46]. Biodegradable nanofibrous membrane was prepared from poly-L-lactic acid by electrospinning and used as a scaffold for cartilage tissue engineering. In order to improve cell attachment and growth, nanofibrous membrane was subject to direct current- (DC-) pulsed oxygen plasma treatment, followed by acrylic acid grafting and collagen coating by covalent binding of collagen to carboxylic moieties of the polyacrylic acid. Primary chondrocytes seeding into the membrane proliferated well and maintained high viability according to previous study [47].

3.4. Biomimetic Materials. Biomimetics refers to the structure and function of tissue-engineered cartilage similar to the cartilage extracellular matrix which provides an ideal microenvironment for chondrocytes. Fibrous scaffolds offer a template for cartilage extracellular matrix production. However, the utilization of homogeneous scaffolds is limited by their inability to mimic the cartilage's zone-specific organization and properties. Trilaminar scaffolds were fabricated by sequential electrospinning and varying fiber size and orientation in a continuous construct, to create scaffolds that can mimic the structural organization and mechanical properties of cartilage's collagen fibrillar network on which bovine chondrocytes proliferated and produced a type II collagen and a sulfated glycosaminoglycan-rich extracellular

matrix. The results demonstrated that trilaminar composite scaffolds mimicked key organizational characteristics of native cartilage, supported cartilage formation *in vitro*, and had superior mechanical properties [48]. Tissue engineering strategies for the intervertebral disc (IVD) have traditionally focused either on the annulus fibrosus (AF) or the nucleus pulposus (NP) in isolation or have simply compared AF cells (AFCs) and NP cells (NPCs) under identical culture conditions. One group developed biomimetic circumferentially orientated polycaprolactone fibres (AF analogue) and seeded them with cells (porcine chondrocytes) and then coagulated a cell-agarose solution in the centre (NP analogue). The results demonstrated that the composite IVD scaffolds had higher modulus and cells were viable and well-distributed around the interface between the NP and AF regions [49]. Besides, a three-layered wedge shaped silk meniscal scaffold system was engineered to mimic native meniscus architecture, which were seeded with human fibroblasts and chondrocytes in a spatial separated mode similar to native tissue in order to generate meniscus-like tissue *in vitro*. This multiporous silk construct is a useful micropatterned template for directed tissue growth with respect to form and function of meniscus-like tissue [50].

Besides mimicking the structure of extracellular matrix, embedding proteins, drugs, or cytokine in scaffolds to mimic the function of ECM is also a biomimetic method as suggested in Table 3. In the process of cartilage repaired with tissue engineering, blood vessel ingrowth and macrophage migration may endanger graft stability of immature constructs. So, control of angiogenesis was proposed as an adjuvant for the treatment of cartilage defects. A clinically compatible fibrin/hyaluronan scaffold with nasal chondrocytes (NC) and functionalized with an FDA-approved antiangiogenic drug (bevacizumab) sequesters vascular endothelial growth factor from the surrounding environment. The proposed pharmacological control of angiogenesis by a therapeutic drug released from a scaffold might enhance constructs survival rate and cartilage regeneration [39]. The repair of cartilage defects can be enhanced with scaffolds but is often accompanied with undesirable terminal differentiation of bone marrow-derived mesenchymal stem cells. Parathyroid hormone-related protein (PTHrP) has been shown to inhibit

aberrant differentiation [51]. Combining PTHrP administration with collagen-silk scaffold is an effective strategy for inhibiting terminal differentiation and enhancing chondrogenesis, thus improving cartilage repair and regeneration [40]. Transforming growth factor- (TGF-) β 1 plays an important role in chondrogenesis [51]. A bioactive microfibrillar poly (L-lactide) scaffold was synthesized by electrospinning, with a direct incorporation of TGF- β 1 into the polymeric solution, on which bovine AFCs were cultured up to 3 weeks. Results demonstrated that AFCs cultured on PLLA/TGF deposited a significantly greater amount of glycosaminoglycans and total collagen with higher neo-ECM thickness [41]. In cartilage tissue engineering, cell adhesion is commonly promoted through the use of polypeptides; however, due to their lack of complementary or modulatory domains, polypeptides must be modified to improve their ability to promote adhesion. According to the principle of matrix-based biomimetic modification, our team utilized a recombinant protein, which spans fragments 7–10 of fibronectin module III (heterophilic motif) and extracellular domains 1–2 of cadherin-11 (rFN/Cad-11) (homophilic motif), to modify the interface of collagen type II (Col II) sponges. The results suggested that the rFN/Cad-11-modified collagen type II biomimetic interface has dual biological functions of promoting adhesion and can stimulate chondrogenic differentiation [42].

4. Challenges and Perspectives

Currently, the main research directions of biomaterials are as follows: the first one is modifying the surface of scaffolds through physical and chemical methods improve the bioactivity of materials for seed cells adhesion and distribution. The second one is making use of new technology to modify the morphology and spatial structure of the materials to compensate the insufficiency in order to build ideal scaffolds. The last one is combining natural materials with synthetic materials to fabricate composite materials with good biocompatibility and mechanical adaptability. With the emergence of new preparation techniques such as 3D fibre deposition and three-dimensional printing, research on cartilage tissue engineering scaffolds has made considerable progress. In addition, as an advanced detecting and monitoring method, biosensors are essential to the development of biotechnology. Electrochemical biosensors can be used for the detection of microRNAs [52]. And electrochemical immunoassays could be used in cancer diagnosis, prognosis, and therapy monitoring [53]. So, the combination of biosensing techniques with biomaterials would vigorously promote the development of tissue engineering. However, with either natural or synthetic materials there exists some problems, such as degradation rate and poor biocompatibility. There is still a great gap to the clinical application of tissue engineering cartilage. Notably, besides scaffolds, other elements of cartilage tissue engineering, cells, and growth factors cannot be ignored. Future research priorities of tissue engineering scaffolds are to improve existing materials and fabrication techniques and to further develop the composite materials, biomimetic materials, nanomaterials, and modified materials. In the near

future, artificial cartilage might show its full potential for the treatment for cartilage injury.

Conflict of Interests

The authors declare that they have no financial or personal relationship with any people or organization that may inappropriately influence their work; there is no professional or commercial interests of any kind in all the commercial identities mentioned in their paper.

Acknowledgments

This work was funded by Grants from Nature Science Foundation of China (81271980), National Basic Research Program (2011CB964701), National Key Technology Research and Development Program of China (2012BAI42G01), and Key project of Logistics Research Plan of PLA (2014).

References

- [1] A. H. Gomoll and T. Minas, "The quality of healing: articular cartilage," *Wound Repair and Regeneration*, vol. 22, supplement 1, pp. 30–38, 2014.
- [2] M. Falah, G. Nierenberg, M. Soudry, M. Hayden, and G. Volpin, "Treatment of articular cartilage lesions of the knee," *International Orthopaedics*, vol. 34, no. 5, pp. 621–630, 2010.
- [3] L. Danisovic, I. Varga, R. Zamborsky et al., "The tissue engineering of articular cartilage: cells, scaffolds and stimulating factors," *Experimental Biology and Medicine*, vol. 237, no. 1, pp. 10–17, 2012.
- [4] Z. Ge, C. Li, B. C. Heng, G. Cao, and Z. Yang, "Functional biomaterials for cartilage regeneration," *Journal of Biomedical Materials Research A*, vol. 100, no. 9, pp. 2526–2536, 2012.
- [5] R. Stoop, "Smart biomaterials for tissue engineering of cartilage," *Injury*, vol. 39, no. 1, pp. 77–87, 2008.
- [6] C. K. Kuo, W. J. Li, R. L. Mauck, and R. S. Tuan, "Cartilage tissue engineering: its potential and uses," *Current Opinion in Rheumatology*, vol. 18, no. 1, pp. 64–73, 2006.
- [7] M. I. Baker, S. P. Walsh, Z. Schwartz, and B. D. Boyan, "A review of polyvinyl alcohol and its uses in cartilage and orthopedic applications," *Journal of Biomedical Materials Research B: Applied Biomaterials*, vol. 100, no. 5, pp. 1451–1457, 2012.
- [8] E. G. Khaled, M. Saleh, S. Hindocha et al., "Tissue engineering for bone production-stem cells, gene therapy and scaffolds," *The Open Orthopaedics Journal*, vol. 5, pp. 289–295, 2011.
- [9] P. Noeaid, V. Salih, J. P. Beier, and A. R. Boccaccini, "Osteochondral tissue engineering: scaffolds, stem cells and applications," *Journal of Cellular and Molecular Medicine*, vol. 16, no. 10, pp. 2247–2270, 2012.
- [10] F. Mirahmadi, M. Tafazzoli-Shadpour, M. A. Shokrgozar, and S. Bonakdar, "Enhanced mechanical properties of thermosensitive chitosan hydrogel by silk fibers for cartilage tissue engineering," *Materials Science and Engineering C*, vol. 33, no. 8, pp. 4786–4794, 2013.
- [11] Y. C. Kuo and C. Y. Chung, "Chondrogenesis in scaffolds with surface modification of elastin and poly-L-lysine," *Colloids and Surfaces B: Biointerfaces*, vol. 93, pp. 85–91, 2012.
- [12] G. Filardo, E. Kon, A. di Martino, M. Busacca, G. Altadonna, and M. Marcacci, "Treatment of knee osteochondritis dissecans with a cell-free biomimetic osteochondral scaffold: clinical and

- imaging evaluation at 2-year follow-up,” *The American Journal of Sports Medicine*, vol. 41, no. 8, pp. 1786–1793, 2013.
- [13] R. J. Egli and R. Luginbuehl, “Tissue engineering—nanomaterials in the musculoskeletal system,” *Swiss Medical Weekly*, vol. 142, Article ID w13647, 2012.
- [14] M. Peran, M. A. Garcia, E. Lopez-Ruiz et al., “Functionalized nanostructures with application in regenerative medicine,” *International Journal of Molecular Sciences*, vol. 13, no. 3, pp. 3847–3886, 2012.
- [15] E. Kon, M. Delcogliano, G. Filardo, G. Altadonna, and M. Marcacci, “Novel nano-composite multi-layered biomaterial for the treatment of multifocal degenerative cartilage lesions,” *Knee Surgery, Sports Traumatology, Arthroscopy*, vol. 17, no. 11, pp. 1312–1315, 2009.
- [16] C. R. Rowland, D. P. Lennon, A. I. Caplan, and F. Guilak, “The effects of crosslinking of scaffolds engineered from cartilage ECM on the chondrogenic differentiation of MSCs,” *Biomaterials*, vol. 34, no. 23, pp. 5802–5812, 2013.
- [17] R. Mueller-Rath, K. Gavénis, S. Andereya et al., “Condensed cellular seeded collagen gel as an improved biomaterial for tissue engineering of articular cartilage,” *Bio-Medical Materials and Engineering*, vol. 20, no. 6, pp. 317–328, 2010.
- [18] C. C. Wang, K. C. Yang, K. Lin, H. Liu, and F. Lin, “A highly organized three-dimensional alginate scaffold for cartilage tissue engineering prepared by microfluidic technology,” *Biomaterials*, vol. 32, no. 29, pp. 7118–7126, 2011.
- [19] Y. Zhang, F. Yang, K. Liu et al., “The impact of PLGA scaffold orientation on invitro cartilage regeneration,” *Biomaterials*, vol. 33, no. 10, pp. 2926–2935, 2012.
- [20] S. Jia, L. Liu, W. Pan et al., “Oriented cartilage extracellular matrix-derived scaffold for cartilage tissue engineering,” *Journal of Bioscience and Bioengineering*, vol. 113, no. 5, pp. 647–653, 2012.
- [21] W. Yang, S. Lee, Y. H. Jo et al., “Effects of natural cartilaginous extracellular matrix on chondrogenic potential for cartilage cell transplantation,” *Transplantation Proceedings*, vol. 46, no. 4, pp. 1247–1250, 2014.
- [22] A. Funayama, Y. Niki, H. Matsumoto et al., “Repair of full-thickness articular cartilage defects using injectable type II collagen gel embedded with cultured chondrocytes in a rabbit model,” *Journal of Orthopaedic Science*, vol. 13, no. 3, pp. 225–232, 2008.
- [23] T. Yuan, K. Li, L. Guo, H. Fan, and X. Zhang, “Modulation of immunological properties of allogeneic mesenchymal stem cells by collagen scaffolds in cartilage tissue engineering,” *Journal of Biomedical Materials Research A*, vol. 98, no. 3, pp. 332–341, 2011.
- [24] Z. Shao, X. Zhang, Y. Pi et al., “Polycaprolactone electrospun mesh conjugated with an MSC affinity peptide for MSC homing in vivo,” *Biomaterials*, vol. 33, no. 12, pp. 3375–3387, 2012.
- [25] Y.-C. Kuo and C.-C. Wang, “Cartilage regeneration by culturing chondrocytes in scaffolds grafted with TATVHL peptide,” *Colloids and Surfaces B: Biointerfaces*, vol. 93, pp. 235–240, 2012.
- [26] Y. C. Kuo and C. C. Wang, “Surface modification with peptide for enhancing chondrocyte adhesion and cartilage regeneration in porous scaffolds,” *Colloids and Surfaces B: Biointerfaces*, vol. 84, no. 1, pp. 63–70, 2011.
- [27] P. Jayabalan, A. R. Tan, M. N. Rahaman, B. S. Bal, C. T. Hung, and J. L. Cook, “Bioactive glass 13–93 as a subchondral substrate for tissue-engineered osteochondral constructs: a pilot study,” *Clinical Orthopaedics and Related Research*, vol. 469, no. 10, pp. 2754–2763, 2011.
- [28] J. Wu, K. Xue, H. Li, J. Sun, and K. Liu, “Improvement of PHBV scaffolds with bioglass for cartilage tissue engineering,” *PLoS ONE*, vol. 8, no. 8, Article ID e71563, 2013.
- [29] C. Foss, E. Merzari, C. Migliaresi, and A. Motta, “Silk fibroin/hyaluronic acid 3D matrices for cartilage tissue engineering,” *Biomacromolecules*, vol. 14, no. 1, pp. 38–47, 2013.
- [30] W. Schuurman, P. A. Levett, M. W. Pot et al., “Gelatin-methacrylamide hydrogels as potential biomaterials for fabrication of tissue-engineered cartilage constructs,” *Macromolecular Bioscience*, vol. 13, no. 5, pp. 551–561, 2013.
- [31] N. Chang, Y. Jhung, C. Yao, and M. Yeh, “Hydrophilic gelatin and hyaluronic acid-treated PLGA scaffolds for cartilage tissue engineering,” *Journal of Applied Biomaterials and Fundamental Materials*, vol. 11, no. 1, pp. 45–52, 2013.
- [32] A. Matsiko, T. J. Levingstone, F. J. O’Brien, and J. P. Gleeson, “Addition of hyaluronic acid improves cellular infiltration and promotes early-stage chondrogenesis in a collagen-based scaffold for cartilage tissue engineering,” *Journal of the Mechanical Behavior of Biomedical Materials*, vol. 11, pp. 41–52, 2012.
- [33] Z. Yang, Y. Wu, C. Li et al., “Improved mesenchymal stem cells attachment and in vitro cartilage tissue formation on chitosan-modified poly(l-lactide-co-epsilon-caprolactone) scaffold,” *Tissue Engineering A*, vol. 18, no. 3–4, pp. 242–251, 2012.
- [34] C. Li, L. Wang, Z. Yang, G. Kim, H. Chen, and Z. Ge, “A viscoelastic chitosan-modified three-dimensional porous poly(L-lactide-co-epsilon-Caprolactone) scaffold for cartilage tissue engineering,” *Journal of Biomaterials Science, Polymer Edition*, vol. 23, no. 1–4, pp. 405–424, 2012.
- [35] J. Deng, R. She, W. Huang, Z. Dong, G. Mo, and B. Liu, “A silk fibroin/chitosan scaffold in combination with bone marrow-derived mesenchymal stem cells to repair cartilage defects in the rabbit knee,” *Journal of Materials Science: Materials in Medicine*, vol. 24, no. 8, pp. 2037–2046, 2013.
- [36] S. W. Whu, K. Hung, K. Hsieh, C. Chen, C. Tsai, and S. Hsu, “In vitro and in vivo evaluation of chitosan-gelatin scaffolds for cartilage tissue engineering,” *Materials Science and Engineering C*, vol. 33, no. 5, pp. 2855–2863, 2013.
- [37] C. Li, J. Zhang, Y. Li, S. Moran, G. Khang, and Z. Ge, “Poly (l-lactide-co-caprolactone) scaffolds enhanced with poly (β -hydroxybutyrate-co- β -hydroxyvalerate) microspheres for cartilage regeneration,” *Biomedical Materials*, vol. 8, no. 2, Article ID 025005, 2013.
- [38] H. F. Liu, J. S. Mao, K. D. Yao, G. Yang, L. Cui, and Y. Cao, “A study on a chitosan-gelatin-hyaluronic acid scaffold as artificial skin in vitro and its tissue engineering applications,” *Journal of Biomaterials Science, Polymer Edition*, vol. 15, no. 1, pp. 25–40, 2004.
- [39] M. Centola, F. Abbruzzese, C. Scotti et al., “Scaffold-based delivery of a clinically relevant anti-angiogenic drug promotes the formation of in vivo stable cartilage,” *Tissue Engineering A*, vol. 19, no. 17–18, pp. 1960–1971, 2013.
- [40] W. Zhang, J. Chen, J. Tao et al., “The promotion of osteochondral repair by combined intra-articular injection of parathyroid hormone-related protein and implantation of a bi-layer collagen-silk scaffold,” *Biomaterials*, vol. 34, no. 25, pp. 6046–6057, 2013.
- [41] G. Vadalà, P. Mozetic, A. Rainer et al., “Bioactive electrospun scaffold for annulus fibrosus repair and regeneration,” *European Spine Journal*, vol. 21, no. 1, pp. S20–S26, 2012.
- [42] S. Dong, H. Guo, Y. Zhang et al., “rFN/Cad-11-modified collagen type II biomimetic interface promotes the adhesion and chondrogenic differentiation of mesenchymal stem cells,” *Tissue Engineering A*, vol. 19, no. 21–22, pp. 2464–2477, 2013.
- [43] L. Koepsell, L. Zhang, D. Neufeld, H. Fong, and Y. Deng, “Electrospun nanofibrous polycaprolactone scaffolds for tissue

- engineering of annulus fibrosus,” *Macromolecular Bioscience*, vol. 11, no. 3, pp. 391–399, 2011.
- [44] M. B. Fisher, E. A. Henning, N. Söegaard, J. L. Esterhai, and R. L. Mauck, “Organized nanofibrous scaffolds that mimic the macroscopic and microscopic architecture of the knee meniscus,” *Acta Biomaterialia*, vol. 9, no. 1, pp. 4496–4504, 2013.
- [45] B. M. Baker, R. P. Shah, A. M. Silverstein, J. L. Esterhai, J. A. Burdick, and R. L. Mauck, “Sacrificial nanofibrous composites provide instruction without impediment and enable functional tissue formation,” *Proceedings of the National Academy of Sciences of the United States of America*, vol. 109, no. 35, pp. 14176–14181, 2012.
- [46] B. Wang, Y. Wu, Z. Shao et al., “Functionalized self-assembling peptide nanofiber hydrogel as a scaffold for rabbit nucleus pulposus cells,” *Journal of Biomedical Materials Research A*, vol. 100, no. 3, pp. 646–653, 2012.
- [47] J. P. Chen, S. F. Li, and Y. P. Chiang, “Bioactive collagen-grafted poly-L-lactic acid nanofibrous membrane for cartilage tissue engineering,” *Journal of Nanoscience and Nanotechnology*, vol. 10, no. 8, pp. 5393–5398, 2010.
- [48] S. D. McCullen, H. Autefage, A. Callanan, E. Gentleman, and M. M. Stevens, “Anisotropic fibrous scaffolds for articular cartilage regeneration,” *Tissue Engineering A*, vol. 18, no. 19-20, pp. 2073–2083, 2012.
- [49] M. Lazebnik, M. Singh, P. Glatt, L. A. Friis, C. J. Berkland, and M. S. Detamore, “Biomimetic method for combining the nucleus pulposus and annulus fibrosus for intervertebral disc tissue engineering,” *Journal of Tissue Engineering and Regenerative Medicine*, vol. 5, no. 8, pp. e179–e187, 2011.
- [50] B. B. Mandal, S. H. Park, E. S. Gil, and D. L. Kaplan, “Multilayered silk scaffolds for meniscus tissue engineering,” *Biomaterials*, vol. 32, no. 2, pp. 639–651, 2011.
- [51] F. Long and D. M. Ornitz, “Development of the endochondral skeleton,” *Cold Spring Harbor Perspectives in Biology*, vol. 5, no. 1, 2013.
- [52] E. Hamidi-Asl, I. Palchetti, E. Hasheminejad, and M. Mascini, “A review on the electrochemical biosensors for determination of microRNAs,” *Talanta*, vol. 115, pp. 74–83, 2013.
- [53] I. Diaconu, C. Cristea, V. Harceaga et al., “Electrochemical immunosensors in breast and ovarian cancer,” *Clinica Chimica Acta*, vol. 425, pp. 128–138, 2013.

Research Article

Bioactivity Assessment of Poly(ϵ -caprolactone)/Hydroxyapatite Electrospun Fibers for Bone Tissue Engineering Application

Mohd Izzat Hassan, Naznin Sultana, and Salehuddin Hamdan

Faculty of Biosciences and Medical Engineering, Universiti Teknologi Malaysia (UTM), Skudai, 81310 Johor Bahru, Johor, Malaysia

Correspondence should be addressed to Naznin Sultana; naznin@biomedical.utm.my

Received 9 May 2014; Accepted 26 June 2014; Published 9 July 2014

Academic Editor: Hao Bai

Copyright © 2014 Mohd Izzat Hassan et al. This is an open access article distributed under the Creative Commons Attribution License, which permits unrestricted use, distribution, and reproduction in any medium, provided the original work is properly cited.

Electrospinning is useful for fabricating nanofibrous structure with different composition and morphologies. It offers great advantages through its geometrical structure and biomimetic property, which can provide a suitable environmental site for cell growth. The fiber diameter is entangled by the concentration of PCL with some adjustment of parameters during electrospinning process. PCL with lower concentration had bead structure while higher concentration had smooth fiber. The incorporation of nanoparticle hydroxyapatite (nHA) into poly(ϵ -caprolactone) fiber was studied. The fiber diameter of PCL was increased with the addition of nHA. Composition of fiber at lower concentrations of PCL and nHA into the polymer produced fiber with a homogenous distribution of nHA in PCL fiber with less agglomeration. The immersion of PCL/nHA fiber in simulated body fluid (SBF) had bone-like apatite layer on its surface while PCL showed no results. PCL/nHA showed high water uptake and had improved wettability compared to PCL alone, suggesting that PCL/nHA fibers were more hydrophilic than PCL fiber.

1. Introduction

Bone is a nanostructured biomaterial with unique biological and mechanical properties. It consists of inorganic hydroxyapatite crystal, organic type I collagen fibers, and other proteins [1]. However, at some time bone may damage and lose its function because of disease or accident. Thus, there is a clinical need for the replacement of the damaged bone. Current trend in clinical practice to overcome the problem is tissue engineering. The purpose of tissue engineering is to regenerate and restore damaged tissue with the combinations of biomaterials, cells, and bioactive agents [2]. In tissue engineering, commonly biodegradable and biocompatible scaffold is used to replace the defect providing a platform for cell function, adhesion, and transplantation.

Nanofibrous scaffold offers great advantages such as the large surface area to volume ratio, with pore structure characteristic, and it can mimic the natural extracellular matrix which is beneficial for cell growth. Among the various techniques of scaffold fabrication, electrospinning can be described as simple and most reliable for producing long and continuous fibers [3–5]. A wide range of polymers can be fabricated using this technique. In addition, the diameters

of the fibers can be controlled from a few micrometers to a few nanometers, depending on the optimization during the electrospinning process and parameter such as solvent used [6].

The scaffold may come from natural and synthetic materials. Synthetic polymer poly(ϵ -caprolactone) (PCL) has been widely used as biomedical materials such as suture material and drug delivery device. It is semicrystalline and bioresorbable aliphatic polyester. It has been intensively explored as tissue engineering scaffold because of its slow biodegradable property (2–4 years) [7, 8]. Due to the low melting temperature at 55–60°C, the PCL can be easily molded into the desired scaffold design from different fabrication techniques. However, PCL is hydrophobic in nature which results in lack of wettability and poor cell attachment compared to hydrophilic material [9]. One way to modify the surface properties of hydrophobic PCL is by blending with bioresorbable ceramics, such as calcium phosphates, hydroxyapatite (HA), and tricalcium phosphate (TCP). HA exists as a major composition of materials in human bone. The presence of HA in the polymer/composite is advantageous for osteoblast proliferation [10–12].

In this study, nanoparticle hydroxyapatite (nHA) incorporation into PCL fiber was investigated through the dispersibility of nHA within the fiber. The surface of the fiber was modified by immersion in a simulated body fluid (SBF) to mimic the mineral of native bone. PCL is a synthetic polymer. So, it may be extremely difficult to induce mineralization because PCL had very few ionic molecular groups compared to natural polymers such as chitosan and collagen. The existence of HA within PCL polymer fibers could improve the surface mineralization process.

2. Materials and Methods

2.1. Materials. PCL with molecular weight 70,000 to 90,000 and acetone (99.8%) were purchased from Sigma-Aldrich. Nanoparticle HA was synthesized by nanoemulsion technique produced in-house from the previous study [13, 14].

2.2. Methods

2.2.1. Preparation of the Solution. PCL was dissolved in acetone solvent at a concentration of 7.5% (w/v) and 12.5% (w/v) at 40°C. HA powder was suspended into the solution at a concentration of 10% (w/w) and 20% (w/w), respectively. The mixed solution was stirred at room temperature for 24 h and homogenized using homogenizer (IKA T25, IKA works, Germany).

2.2.2. Electrospinning Fibrous Scaffold. The prepared solution was transferred into a 5 mL syringe, with 18 and 22 G blunt-end needle. The electrospinning was conducted using electrospinning unit (NaBond, China). The distance between the needle tip and aluminium collector was adjusted at 10 cm. High voltage of 15–22 kV was applied to the needle. The solution was ejected at a feeding rate of 3 mL/h using infusion pump (Veryark TCV-IV, China). The resulting fiber was dried overnight to remove any solvent left on its surface.

2.2.3. Bioactivity Test. The bioactivity test was done by immersing the fibers in SBF. The SBF was prepared in accordance with Kokubo et al. [15] with ion concentration (in mM: Na⁺ 142.0, K⁺ 5.0, Mg²⁺ 1.5, Ca²⁺ 2.5, Cl⁻ 147.8, HCO₃⁻ 4.2, HPO₄²⁻ 1.0, SO₄²⁻ 0.5) almost similar to human blood plasma with initial pH 7.4 at 37°C in a water bath (Memmert, Schwabach, Germany). The fiber was cut into (1 × 1) cm², left in SBF, and was extracted at 3, 7, and 14 days.

2.2.4. Microstructure Characterization. The morphology of the fibers was observed under SEM (Hitachi TM 3000, Japan) at an accelerating voltage of 15 kV and FESEM (Hitachi SU 8020, Japan). The fibers immersed in SBF analyzed by FESEM were gold-coated prior to analysis. The diameter of single fiber was measured at random location using image analysis software (Image J, NIH, USA). Energy dispersive X-ray (EDX) was used to confirm the presence of HA in the PCL polymer.

2.2.5. Contact Angle. Water contact angle was measured by dropping deionized water (3 μL) onto the surface using 28 gauge blunt tip needle on different areas on the surfaces to determine the wettability of the fibers using a contact angle instrument (VCA-Optima, AST Inc., USA). Water was dropped on 5/6 places on each sample surface and the average and standard deviation was calculated.

2.2.6. Water Uptake. Water uptake of the fiber was measured to see how much water can be absorbed, which mainly depends on the hydrophilicity of the fiber. The fiber before immersion in SBF was cut into (2 × 1) cm² and immersed in deionized water. The fiber was removed at the interval of 1 min, wiped gently with clean tissue paper, and weighed. The process was repeated for 10 min. The water uptake of the fiber after immersion in SBF was measured similarly at different intervals of 3, 7, and 14 days. The water uptake was calculated using the following equation [16]:

$$\% \text{ Water uptake} = 100 \times \frac{W_{\text{wet}} - W_o}{W_o}, \quad (1)$$

where W_{wet} is the weight of the wet fiber and W_o is the starting dry weight of the fiber.

3. Results and Discussion

3.1. Morphology of Electrospun Fibrous Scaffold. Figure 1 shows the morphologies of fibrous scaffolds produced from 7.5% (w/v) PCL, 12.5% (w/v) PCL, 10% nHA incorporated 7.5% (w/v) and 12.5% (w/v) PCL, and 20% nHA incorporated 7.5% (w/v) and 12.5% (w/v) PCL (Figures 1(a)–1(f)). Electrospun nanofibrous PCL at lower concentration had the disadvantage. There were many unwanted beads with spindle-like structure which was observed (Figure 1(a)). Meanwhile, smooth fiber was obtained at higher concentration (Figure 1(b)). However, there was an increased size of fiber from nanometer into micrometer in range. Incorporation of nHA into PCL fibers was also examined. The addition of 10% (w/w) nHA into 7.5% (w/v) PCL and 12.5% (w/v) PCL was found to have smooth fiber structure (Figures 1(c) and 1(e)). Increased fiber diameter was also observed. The nHA was well-dispersed into the fiber and only small agglomeration was found. In a recent study, it was described that the agglomeration of nanoparticles resulted in large size and low mechanical properties of fiber [17]. This was related to the increased content of loading nanoparticles. In our study, no apparent change in the size of the fiber was observed. It proves the successful incorporation of nHA nanoparticles homogeneously in the fibers. On the other hand, the addition of 20% (w/w) nHA into 12.5% (w/v) PCL resulted in increasing the size of the fiber. This was in agreement with another study where the addition of nanoparticle increased the diameter of fiber [18]. However, many agglomerations were found within the random fiber (Figures 1(d) and 1(f)). Another study showed higher agglomeration at 20% HA into different polymer of poly(D,L-lactide-co-glycolide) (PLGA) had broken fiber, but in this study no broken fiber was identified [19].

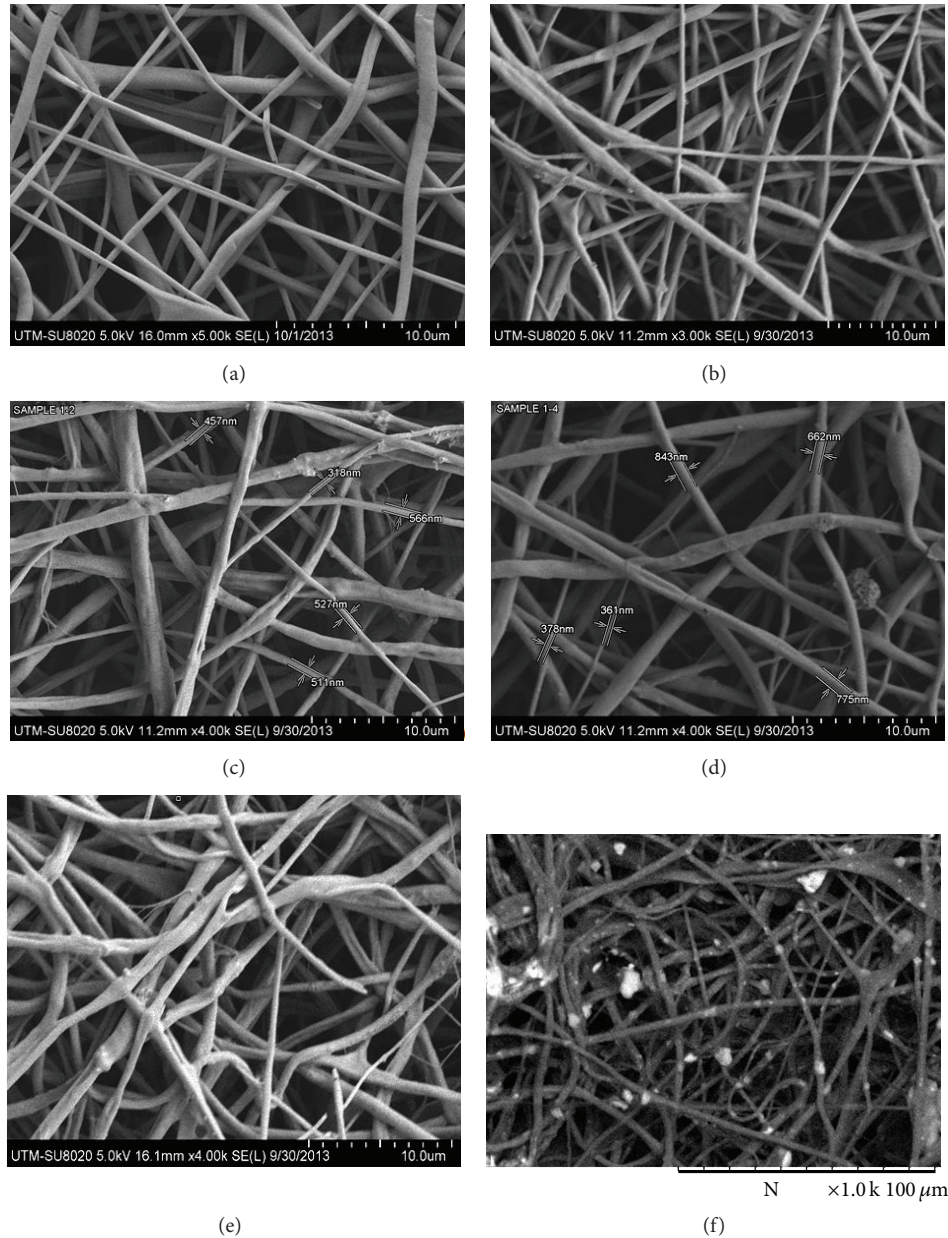


FIGURE 1: SEM micrographs of fibers at different compositions: (a) 7.5% (w/v) PCL; (b) 12.5% (w/v) PCL; (c) 7.5% (w/v) PCL with 10% (w/w) nHA; (d) 7.5% (w/v) PCL with 20% nHA; (e) 12.5% (w/v) PCL with 10% (w/w) nHA; (f) 12.5% (w/v) PCL with 10% (w/w).

3.2. Bioactivity Evaluation of Fibers in SBF. The ability of forming apatite onto the fiber was evaluated through soaking them in SBF for 3, 7, and 14 days using a sample of 7.5% (w/v) PCL and 7.5% (w/v) PCL with 10% (w/w) nHA. When the sample was immersed into SBF, PCL fiber was floated suggesting that high hydrophobic surface prevents water absorption. Meanwhile, composite fiber settled down to the bottom dish suggesting the fiber was high in density. It also showed faster absorption of water into the fiber. From Figure 2, it was observed that the composite fiber started to nucleate hydroxyapatite at day 3 and showed full mineralization after 7 days. After 14 days, some parts of fibers were completely covered by the apatite layer and the interfaces of fibers were blocked by apatite layer. Meanwhile,

no noticeable bone-apatite layer was observed on PCL fibers even after seven days. A scaffold material should possess porous structure with high percentage of porosity and good interconnectivity. The fiber should maintain the pore shape to provide better connectivity as a scaffold. Thus, the fibers after immersing for 7 days in SBF had good property as a scaffold as it showed better interconnectivity of the pores while preserving its microstructure. EDX analyses at different locations of composite electrospun fibers also confirmed the presence of nHA particles that were well mixed with polymer fiber surfaces (Figure 3(a)). The distribution of Ca in 10% nHA in PCL nanofiber matrices after immersing in SBF was further confirmed by the elemental mapping of Ca (Figure 3(b)).

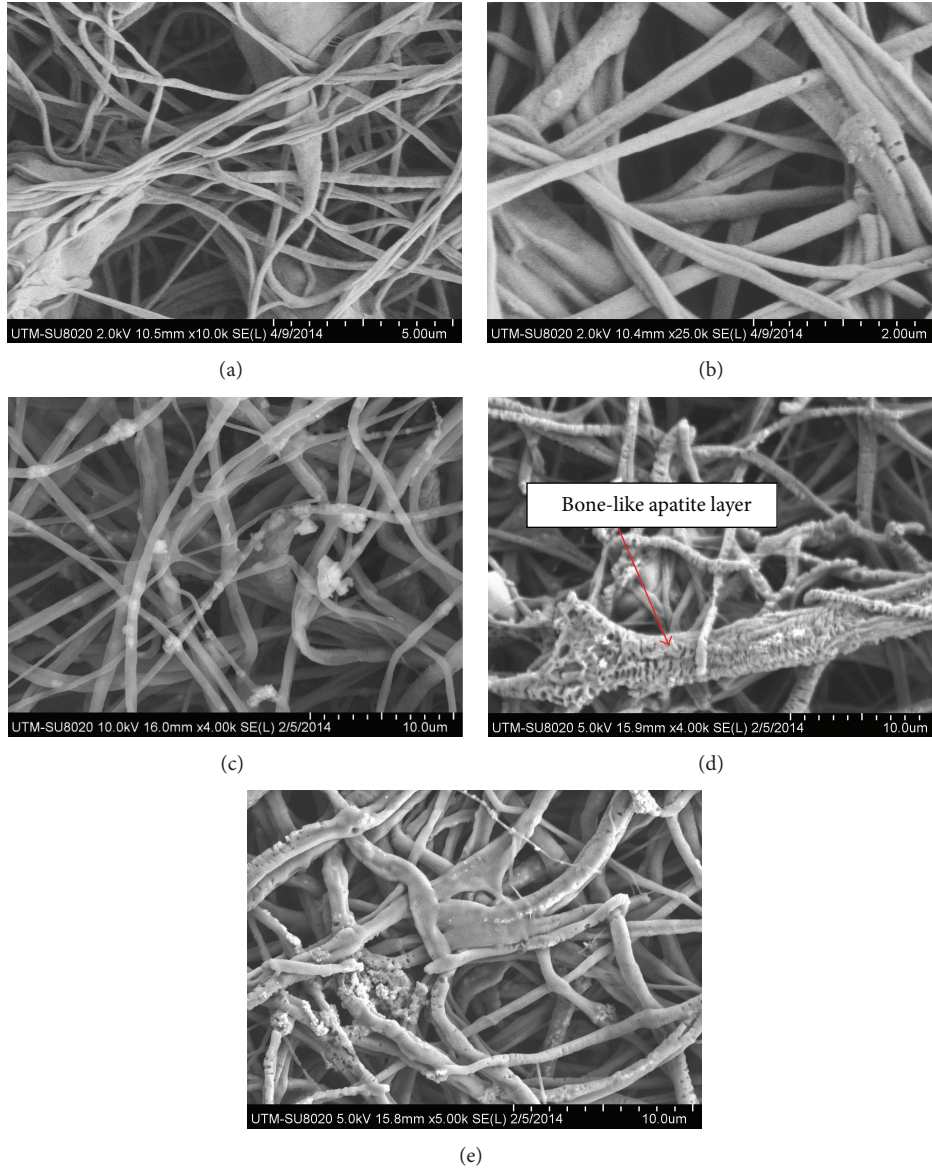


FIGURE 2: FESEM micrographs of 7.5% (w/v) PCL fiber immersed in SBF after (a) 3 days, (b) 7 days; (c) 7.5% (w/v) PCL with 10% (w/w) nHA immersed in SBF after 3 days, (d) 7 days, and (e) 14 days.

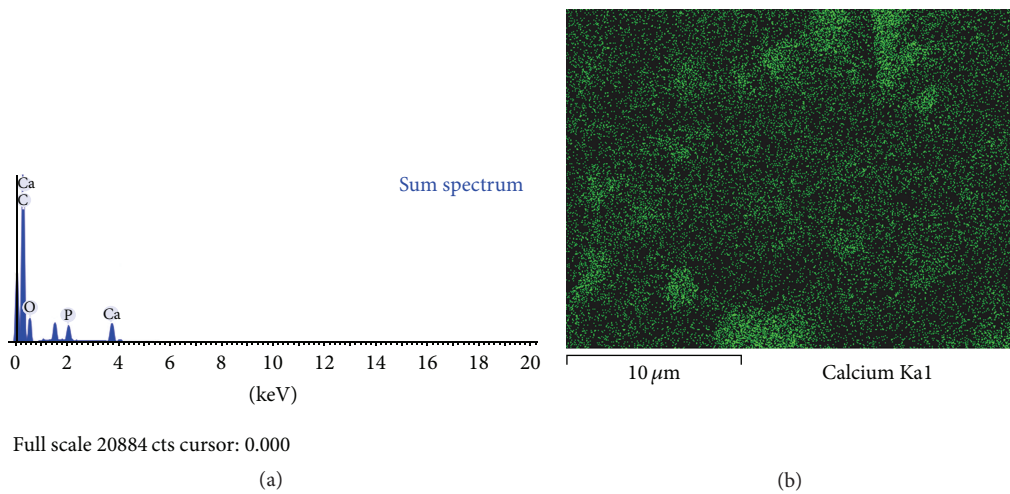


FIGURE 3: (a) An EDX spectrum and (b) Ca distribution on PCL with 10% (w/w) nHA immersed in SBF after 7 days.

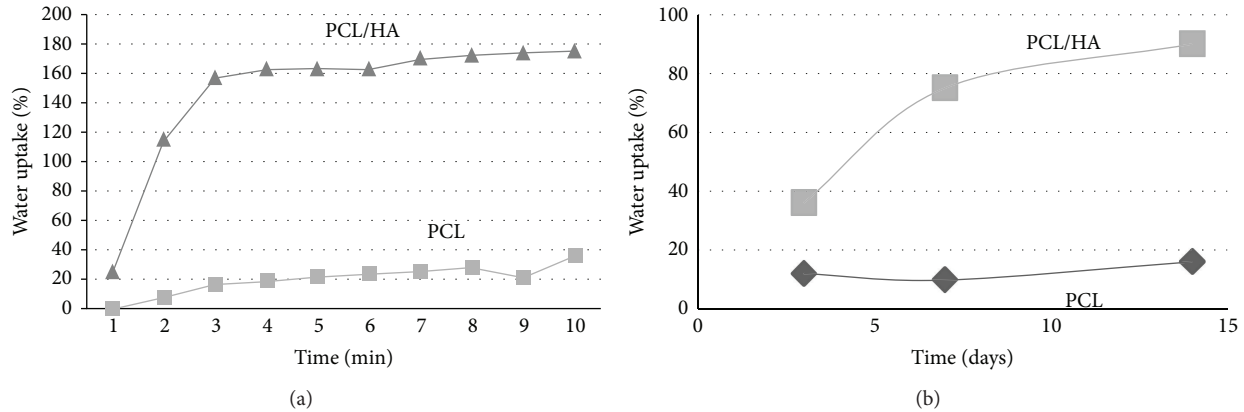


FIGURE 4: Water uptake of PCL fiber and PCL/HA fibers in (a) deionized water over time (minutes) and (b) in simulated body fluid (SBF) over time (days).

TABLE 1: Contact angle measurement of fibers at different PCL and HA concentration.

Composition	0% HA/7.5% PCL	10% HA/7.5% PCL	20% HA/7.5% PCL	0% HA/12.5% PCL	10% HA/12.5% PCL	20% HA/12.5% PCL
Contact angle	127.3 ± 2.4	112.7 ± 3.1	106.3 ± 4.5	120.5 ± 2.2	115.1 ± 4.1	93.7 ± 3.6

3.3. Contact Angle Measurement. The wettability of the fiber was determined using contact angle. The desired scaffold property for cell interaction is hydrophilic surface. Table 1 shows the contact angle of different composition of HA/PCL fibers. The change in contact angle was observed. With an increasing amount of 10% (w/w) and 20% (w/w) nHA, some decreases of contact angles were observed. This is due to the incorporation of hydrophilic nHA. This shows that the incorporation of nHA as a second-phase material with hydrophilic property reduced the contact angle of pure PCL fiber. Also surface roughness had influence on this property [19, 20]. These results indicated that PCL/nHA fibers had better hydrophilicity. A change in contact angle of the fiber can give early prediction of successful blending and surface modification. However, it also depends on the surface roughness of the fiber. This is because when the surface roughness is high, only a small quantity of water may come in contact with the surface of the fiber. So, the interaction between fiber and water becomes low and the interaction of water and air becomes high. This will cause increase in contact angle for rougher surface. It was also reported that the surface roughness increased with increasing of fiber diameter and increasing with the incorporation of nHA [21, 22]. Since PCL is hydrophobic polymer, adding nHA into the polymer can alter the properties into more hydrophilic and rougher surface. Rougher surface may cause slightly higher contact angle of fiber. However since HA is hydrophilic, there was only a slight change of lower contact angle with the increasing amount of nHA. The contact angle of PCL/nHA fiber after

7 days in SBF was 84.4 ± 3.5 . The deposition of apatite on fiber surface rendered them into more hydrophilic one.

3.4. Water Uptake. Figure 4(a) shows water uptake of 7.5% (w/v) PCL and 7.5% (w/v) PCL with 10% (w/w) nHA fiber at different time interval after soaking in deionized water. It showed that PCL/nHA fiber had higher water uptake while PCL had lower water uptake properties. Initial water uptake of PCL fiber was 0.4% and had the highest water uptake at 35.5%. Meanwhile, PCL/nHA fiber had initial water uptake of 25% and the highest water uptake of 175%.

The water uptake of the fiber immersed in SBF was measured as in Figure 4(b). PCL fiber showed a lower percentage of water absorbed (11.94%) at day 3 due to hydrophobic property. From day 3 to day 7, it was slightly decreased by 9.72%. Up to day 14, it was gradually increased to 15.95%. PCL/nHA fiber showed faster water absorption at day 3 with 36% water uptake. From day 3 to day 7, it showed an abrupt increase by 75%. The water uptake gradually increased until reaching a final value of 90% at day 14. The results showed PCL/nHA exhibits better hydrophilicity than PCL fiber. After 20 days, no significant increase in water uptake was observed, indicating the saturation state. The water uptake properties are very important for porous materials to study the mechanism. After an initial period of time, all the materials exhibit an equilibrium state [4]. After longer time, when the polymers start to degrade or the HA starts to dissolve, weight loss can be observed for composite scaffolds or fibers.

4. Conclusion

Using the electrospinning technique, beadless HA/PCL nanofiber was obtained. Immersion in SBF showed 7.5% (w/v) PCL with 10% (w/w) nHA fiber had good bioactivity up to seven days compared to PCL fiber. Contact angle and water uptake showed that the composite PCL/nHA fibers were more hydrophilic than PCL fiber. The water uptake property was also greater in the composite fibers than pure PCL fiber. The composite electrospun fiber of PCL with osteoconductive nHA is expected to be conducive for osteoblast growth for bone tissue regeneration.

Conflict of Interests

The authors declare that there is no conflict of interests.

Acknowledgments

The authors would like to acknowledge the Faculty of Biosciences and Medical Engineering, Universiti Teknologi Malaysia (UTM), for the lab facilities. This work was supported by research Grants GUP Tier 1 (05H07). The authors are also thankful for the support given by MOHE, RMC, and UTM.

References

- [1] T. J. Webster and E. S. Ahn, "Nanostructured biomaterials for tissue engineering bone," *Advances in Biochemical Engineering/Biotechnology*, vol. 103, pp. 275–308, 2007.
- [2] V. Leung and F. Ko, "Biomedical applications of nanofibers," *Polymers for Advanced Technologies*, vol. 22, no. 3, pp. 350–365, 2011.
- [3] L. T. H. Nguyen, S. Chen, N. K. Elumalai et al., "Biological, chemical, and electronic applications of nanofibers," *Macromolecular Materials and Engineering*, vol. 298, no. 8, pp. 822–867, 2013.
- [4] N. Sultana and T. H. Khan, "Water absorption and diffusion characteristics of nanohydroxyapatite (nHA) and poly(hydroxybutyrate-co-hydroxyvalerate-) based composite tissue engineering scaffolds and nonporous thin films," *Journal of Nanomaterials*, vol. 2013, Article ID 479109, 8 pages, 2013.
- [5] T. Sun, T. H. Khan, and N. Sultana, "Fabrication and *in vitro* evaluation of nanosized hydroxyapatite/Chitosan-based tissue engineering scaffolds," *Journal of Nanomaterials*, vol. 2014, Article ID 194680, 8 pages, 2014.
- [6] L. A. Bosworth and S. Downes, "Acetone, a sustainable solvent for electrospinning poly(ϵ -caprolactone) fibres: effect of varying parameters and solution concentrations on fibre diameter," *Journal of Polymers and the Environment*, vol. 20, no. 3, pp. 879–886, 2012.
- [7] A. Cipitria, A. Skelton, T. R. Dargaville, P. D. Dalton, and D. W. Hutmacher, "Design, fabrication and characterization of PCL electrospun scaffolds—a review," *Journal of Materials Chemistry*, vol. 21, no. 26, pp. 9419–9453, 2011.
- [8] L. S. Nair and C. T. Laurencin, "Biodegradable polymers as biomaterials," *Progress in Polymer Science*, vol. 32, no. 8–9, pp. 762–798, 2007.
- [9] C. H. Kim, M. S. Khil, H. Y. Kim, H. U. Lee, and K. Y. Jahng, "An improved hydrophilicity via electrospinning for enhanced cell attachment and proliferation," *Journal of Biomedical Materials Research B: Applied Biomaterials*, vol. 78, no. 2, pp. 283–290, 2005.
- [10] W. Song, D. C. Markel, S. Wang, T. Shi, G. Mao, and W. Ren, "Electrospun polyvinyl alcohol-collagen-hydroxyapatite nanofibers: a biomimetic extracellular matrix for osteoblastic cells," *Nanotechnology*, vol. 23, no. 11, Article ID 115101, 2012.
- [11] Y. Zhang, J. R. Venugopal, A. El-Turki, S. Ramakrishna, B. Su, and C. T. Lim, "Electrospun biomimetic nanocomposite nanofibers of hydroxyapatite/chitosan for bone tissue engineering," *Biomaterials*, vol. 29, no. 32, pp. 4314–4322, 2008.
- [12] H. Kim, H. Lee, and J. C. Knowles, "Electrospinning biomedical nanocomposite fibers of hydroxyapatite/poly(lactic acid) for bone regeneration," *Journal of Biomedical Materials Research A*, vol. 79, no. 3, pp. 643–649, 2006.
- [13] M. I. Hassan, M. Mokhtar, N. Sultana, and T. H. Khan, "Production of hydroxyapatite(HA) nanoparticle and HA/PCL tissue engineering scaffolds for bone tissue engineering," in *Proceedings of the 2nd IEEE-EMBS Conference on Biomedical Engineering and Sciences (IECBES '12)*, pp. 239–242, December 2012.
- [14] W. Y. Zhou, M. Wang, W. L. Cheung, B. C. Guo, and D. M. Jia, "Synthesis of carbonated hydroxyapatite nanospheres through nanoemulsion," *Journal of Materials Science: Materials in Medicine*, vol. 19, no. 1, pp. 103–110, 2008.
- [15] T. Kokubo, H. Kim, and M. Kawashita, "Novel bioactive materials with different mechanical properties," *Biomaterials*, vol. 24, no. 13, pp. 2161–2175, 2003.
- [16] B. Rai, S. H. Teoh, and K. H. Ho, "An *in vitro* evaluation of PCL-TCP composites as delivery systems for platelet-rich plasma," *Journal of Controlled Release*, vol. 107, no. 2, pp. 330–342, 2005.
- [17] M. Kharazih, M. H. Fathi, and H. Edris, "Development of novel aligned nanofibrous composite membranes for guided bone regeneration," *Journal of the Mechanical Behavior of Biomedical Materials*, vol. 24, pp. 9–20, 2013.
- [18] P. Wutticharoenmongkol, N. Sanchavanakit, P. Pavasant, and P. Supaphol, "Preparation and characterization of novel bone scaffolds based on electrospun polycaprolactone fibers filled with nanoparticles," *Macromolecular Bioscience*, vol. 6, no. 1, pp. 70–77, 2006.
- [19] M. V. Jose, V. Thomas, K. T. Johnson, D. R. Dean, and E. Nyairo, "Aligned PLGA/HA nanofibrous nanocomposite scaffolds for bone tissue engineering," *Acta Biomaterialia*, vol. 5, no. 1, pp. 305–315, 2009.
- [20] F. Yang, J. G. C. Wolke, and J. A. Jansen, "Biomimetic calcium phosphate coating on electrospun poly(ϵ -caprolactone) scaffolds for bone tissue engineering," *Chemical Engineering Journal*, vol. 137, no. 1, pp. 154–161, 2008.
- [21] C. Xu, F. Yang, S. Wang, and S. Ramakrishna, "In vitro study of human vascular endothelial cell function on materials with various surface roughness," *Journal of Biomedical Materials Research A*, vol. 71, no. 1, pp. 154–161, 2004.
- [22] V. Thomas, D. R. Dean, M. V. Jose, B. Mathew, S. Chowdhury, and Y. K. Vohra, "Nanostructured biocomposite scaffolds based on collagen coelectrospun with nanohydroxyapatite," *Biomacromolecules*, vol. 8, no. 2, pp. 631–637, 2007.

Research Article

Structure and Identification of Solenin: A Novel Fibrous Protein from Bivalve *Solen grandis* Ligament

Jun Meng,¹ Gang-Sheng Zhang,² and Zeng-Qiong Huang¹

¹ College of Pharmacy, Guangxi Medical University, 22 Shuangyong Road, Nanning, Guangxi 530021, China

² College of Materials Science and Engineering, Guangxi University, 100 Daxue Road, Nanning, Guangxi 530004, China

Correspondence should be addressed to Zeng-Qiong Huang; huangzengqiong@163.com

Received 19 May 2014; Accepted 17 June 2014; Published 8 July 2014

Academic Editor: Jingxia Wang

Copyright © 2014 Jun Meng et al. This is an open access article distributed under the Creative Commons Attribution License, which permits unrestricted use, distribution, and reproduction in any medium, provided the original work is properly cited.

Fibrous proteins, which derived from natural sources, have been acting as templates for the production of new materials for decades, and most of them have been modified to improve mechanical performance. Insight into the structures of fibrous proteins is a key step for fabricating of bioinspired materials. Here, we revealed the microstructure of a novel fibrous protein: solenin from *Solen grandis* ligament and identified the protein by MALDI-TOF-TOF-MS and LC-MS-MS analyses. We found that the protein fiber has no hierarchical structure and is homologous to keratin type II cytoskeletal 1 and type I cytoskeletal 9-like, containing “SGGG,” “SYGSGGG,” “GS,” and “GSS” repeat sequences. Secondary structure analysis by FTIR shows that solenin is composed of 41.8% β -sheet, 16.2% β -turn, 26.5% α -helix, and 9.8% disordered structure. We believe that the β -sheet structure and those repeat sequences which form “glycine loops” may give solenin excellence elastic and flexible properties to withstand tensile stress caused by repeating opening and closing of the shell valves in vivo. This paper contributes a novel fibrous protein for the protein materials world.

1. Introduction

Fibrous proteins have attracted much attention for a long time because of their excellent tensile strength, elastic properties, biocompatibility, and implication for fabricating biomaterials. The most common fibrous proteins include collagen, elastin, silk fibroin, and keratin, whose microstructures, composition, primary structures, and mechanical properties have been studied in detail [1–3]. Mussel byssal thread, a fibrous biomaterial from bivalve mollusc, has also been investigated for decades. This hair-like fiber can be divided into three regions: an elastic proximal thread, stiff distal thread, and adhesive plaque regions, and it was found to contain collagenous and elastin-like domains that play a key role in the extraordinary mechanical properties [4–6]. Although these proteins have been studied in detail; however, the knowledge about fibrous proteins in bivalve ligaments is still limited.

Bivalve ligament is an elastic calcified structure which connects two shell valves dorsally and functions like a coil spring to open the valves when adductor muscles relax.

Most of bivalve ligaments are divided structurally into an outer uncalcified protein layer and an inner calcified layer made up of aragonite and matrix proteins [7]. They have attracted the interest of materials scientists as elastic biocomposite materials with particular structure presenting excellent mechanical properties [8]. Generally, an intact ligament is composed of about 40% protein and 60% calcium carbonate [9]. These proteins have been studied for decades. Earlier studies were carried out mainly on amino acid composition analysis. For instance, Kelly and Rice [10] and Kahler et al. [9] reported that ligament proteins contain high contents of glycine and methionine but are devoid of hydroxyproline and hydroxylysine. Later, Kikuchi et al. [11] confirmed the results and identified two components desmosine and isodesmosine acting as cross-link in ligament protein. More recent studies have revealed insights into gene cloning and secondary structure analysis of the rubber-like protein: abduction of scallop and the synthetic peptides inspired by abduction [12, 13]. Besides, few studies have been given to proteins, especially fibrous proteins in other bivalve ligaments. Recently, we found two novel fibrous proteins from *Siliqua radiata*

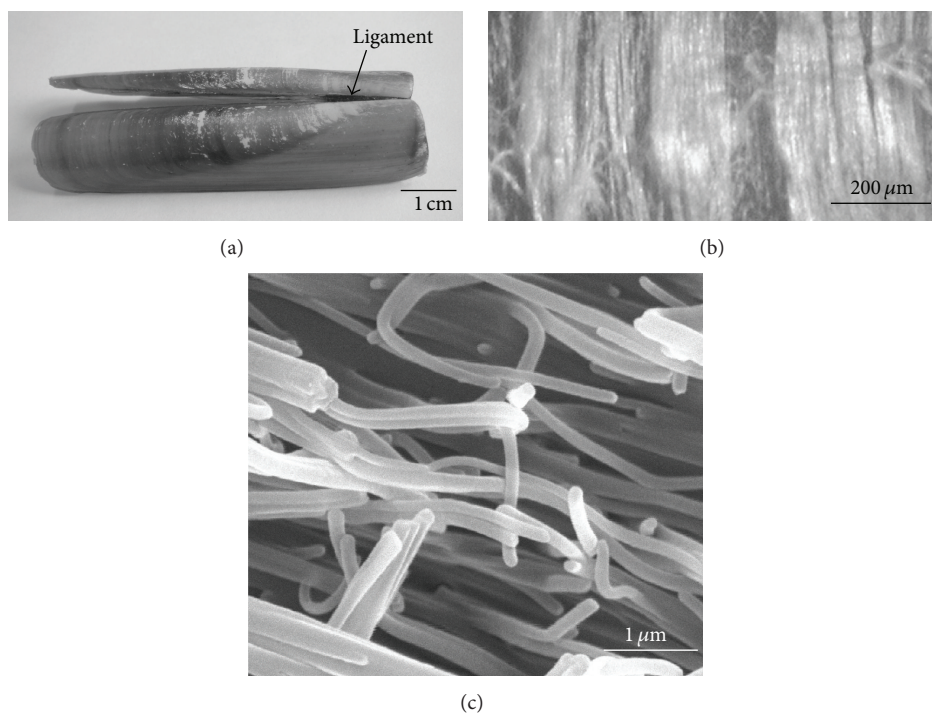


FIGURE 1: Optical photos and SEM image of the experiment sample. (a), (b) Optical photos of *S. grandis* and ligament fibrous protein, respectively, and (c) SEM image of the fibrous protein.

and *Solen grandis* ligaments. The former, named as K58, was found homologous to keratin type II cytoskeletal I [14, 15]; the latter, which has never been studied, is composed of protein fibers with diameter of about 120 nm (Figure 1) [16].

This paper aims to observe the microstructure of the fibrous protein (FP), identify it by MALDI-TOF-TOF-MS and LC-MS-MS analyses, and reveal its secondary structure by FTIR analysis.

2. Materials and Methods

2.1. Sample Preparation and Observations. *S. grandis* (Figure 1(a)) was freshly collected from Beihai city of Guangxi in southern China. After removing the soft body, ligaments were separated from shells mechanically, washed with deionized water, and air-dried. Then, we stripped away the outer layer and took an optical photo of the protein (Figure 1(b)) using a microscope equipped with a CCD camera. To obtain the SEM image (Figure 1(c)), FP was coated with gold and observed by a SEM (S-3400N, Hitachi) operated at accelerating voltage of 30 kV.

2.2. TEM Observations. To observe the detailed structure of FP, we carried out TEM observations. First, we soaked FP in 3% glutaraldehyde for 3 days and then fixed it with 1% osmic acid for 2 h. After being dehydrated gradually with ethanol-acetone solution, FP was permeated by using acetone-epoxy resin for 24 h. Then, the embedded FP was sliced into 70 nm thickness in longitudinal and transverse section with Leica UC7 ultramicrotome. Finally, the slices were stained with

uranyl acetate-lead citrate solution and observed by Hitachi H-7650 TEM with acceleration voltage of 100 kV.

2.3. Sodium Dodecyl Sulphate-Polyacrylamide Gel Electrophoresis (SDS-PAGE). For biochemical analysis, FP was ground into powder in liquid nitrogen. Then, 20 mg powder was treated with 7 M urea, 3% 2-mercaptoethanol, and 0.5 M NaOH solution at 65°C for 1 h. After being centrifuged at 12000 rpm and 4°C for 20 min, we discarded the solution and treated the residue with the same conditions except NaOH solution that was diluted into 0.25 M. Then, the sample solution was obtained by centrifugation and dialyzed with a dialysis bag of 14 kDa molecular weight cutoff for three days. Dialysate was concentrated under vacuum, treated with 2D-Clean-Up Kit (GE Healthcare), and redissolved in lysis buffer.

After being quantified by Bradford assay, 26.1 μg protein sample and molecular weight standards (MW 14.4–94.0 kDa, TianGen Biotech) were applied to SDS-PAGE on a 12% separating gel using a JY 600 electrophoresis system (JunYi Technology). Electrophoresis was followed by silver staining and the gel band 1-1 (~78 kDa) in lane 1 (Figure 2) was excised for trypsin digestion.

2.4. In-Gel Trypsin Digestion and MALDI-TOF-TOF-MS Analysis. Gel band 1-1 was destained, dehydrated, and dried under vacuum. Then, gel pieces were rehydrated with 10 ng μL⁻¹ trypsin in 40 mM NH₄HCO₃ and 10% acetonitrile solution for 45 min in ice bath. After being incubated at 37°C for 16 h, peptides were extracted from the gel twice with 50% acetonitrile and 0.1% trifluoroacetic acid. The extraction was

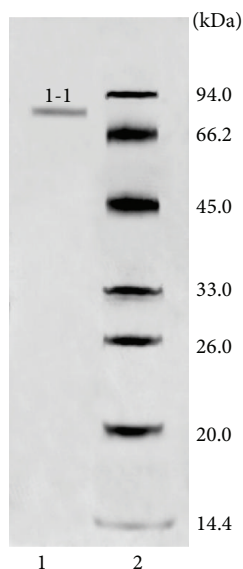


FIGURE 2: SDS-PAGE pattern of FP (lane 1) and molecular weight standards (lane 2).

vacuum-dried, redissolved in 0.1% trifluoroacetic acid, and mixed with α -cyano-4-hydroxycinnamic acid (CHCA). The mixture was applied to a 4800 mass spectrometer (Applied Biosystems, Framingham) running in positive ion reflection mode in the mass range of 800–4000 Da. The ten most intense ions were selected for MS-MS analysis with acceleration voltage of 20 kV.

The acquired MS and MS-MS data were combined and searched against protein databases at NCBI and Swiss-Prot using the Mascot search engine with GPS Explorer Software (Applied Biosystems). Mass tolerance of 200 ppm and ± 0.3 Da for MS and MS-MS were set, and variable modifications, such as oxidation, methylation, and phosphorylation, were under consideration. Protein score calculated by the software was used for correct identification.

2.5. LC-MS-MS Analysis. FP sample solution was separated by SDS-PAGE again, and the similar gel band was excised and digested by trypsin. Digested sample was dissolved in 0.1% formic acid and desalted with 0.2% formic acid on a Zorbax 300 SB C18 peptide trap. Then, peptides were separated by a reversed phase C18 column (0.15 mm \times 150 mm, Column Technology Inc.) with a linear gradient of 0–50% mobile phase A (0.1% formic acid and 84% acetonitrile) in mobile phase B (0.1% formic acid) over 60 min. Separated peptides were eluted into an LTQ linear ion trap mass spectrometer (Thermo Finnigan) equipped with a microspray source running in data-dependent mode with spray voltage of 3.4 kV at 200°C and full scan mass range of 300–1800 Da. Dynamic exclusion was enabled with a repeat count of 2 and exclusion duration of 1.5 min. The ten most intense ions in every full scan were selected automatically for MS-MS analysis.

The MS-MS spectra were searched against protein databases using SEQUEST algorithm. All SEQUEST searches were performed on Bioworks 3.2 software (Thermo Finnigan)

with following parameters: fully tryptic peptide, parent mass tolerance 1.4; peptide mass tolerance 1.5. Delta CN (≥ 0.1) and Xcorr (one charge ≥ 1.9 , two charges ≥ 2.2 , and three charges ≥ 3.75) were used as criteria for identification.

2.6. FTIR and Secondary Structure Analysis. FP powder was mounted in KBr and scanned using an FTIR (Nicolet 4700, Thermo Electron) with 64 scans and resolution of 2 cm^{-1} in the range of 4000–400 cm^{-1} . The amide I region (1700–1600 cm^{-1}) of the spectrum was curve fitted into Gaussian curve for secondary structure analysis. Curve-fitting was carried out using origin 7.5 software (OriginLab) equipped with peak fitting module (PFM) with following parameters: data preconditioning: methods 11; filters: savitzky-golay, polynomial 2; find peaks with threshold height of 0.002. We used the peak position of individual component of Gaussian curve to assign α -helix (1650–1657 cm^{-1}), β -sheet (1612–1640 cm^{-1}), β -turn (1655–1675 cm^{-1}), and disordered (1640–1651 and 1670–1697 cm^{-1}) structure [17, 18]. Peak area of each component was calculated to obtain secondary structure data.

3. Results and Discussion

3.1. TEM Observations. The morphology of FP has been observed by SEM in Figure 1(c) and previous study [16]. However, owing to the limited resolution of SEM, it is hard to observe the fine structure of FP, especially the detailed structure of transverse sections of the protein fibers. By using TEM, we found that transverse sections of these protein fibers are roundish with diameters ranging from 130 to 200 nm, and they arrange orderly connecting one by one like many strings of pearls (Figure 3(a)). It is worth noting that diameters of protein fibers in TEM image are larger than those in SEM (about 120 nm). This inconsistency is very likely due to the pretreatment of FP for TEM observation. At higher magnification (Figure 3(b)) and from longitudinal view (Figures 3(c) and 3(d)), we did not find any microfibrils within these protein fibers, which means that these fibers have no hierarchical structure and they are not constructed by microfibrils. This structure feature is different from keratin and collagen fibers, both of which have complex hierarchical structures and are assembled by microfibrils as elementary building blocks [1, 3]. These results imply that FP may be a new kind of fibrous protein.

3.2. MALDI-TOF-TOF-MS Results and Data Analysis. In previous study [14], we have found that FP has strikingly high Gly, Asp, Met, and Phe contents but contains trace amount of Hyp. That means that FP is not collagen. To identify this unique fibrous protein, mass spectrometry was performed and the results are shown in the following.

As expected, no proteins of bivalve mollusc were matched when searched against protein databases. However, unexpectedly, FP was identified as *Pan troglodytes* keratin type II cytoskeletal 1 (K1) and *Pongo abelii* keratin type I cytoskeletal 9-like (K9) with protein score of 625 and 491, respectively,

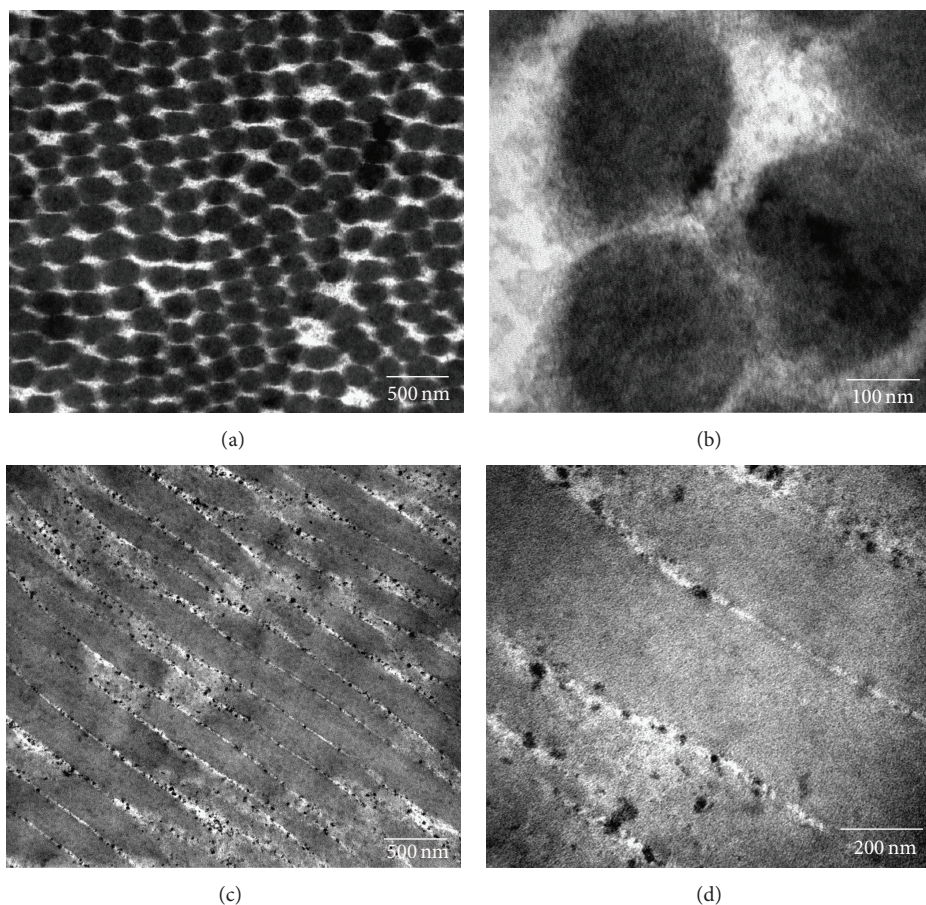


FIGURE 3: TEM observation of FP. (a) Transverse section of FP, (b) enlarged view of transverse section of FP that shows no microfibrils within the protein fibers, (c) longitudinal section of FP, and (d) enlarged view of longitudinal section of FP that shows no microfibrils within the protein fibers.

representing 100% confidence. Furthermore, some interesting repeat sequences of “SGGG,” “SYGSGG,” “GS,” and “GSS” were highly matched (Tables 1 and 2).

Although FP was highly matched with K1 and K9, it does not mean that FP is K1 or K9, because the molecular weight of FP (~78 kDa) (Figure 2) is higher than K1 (~64 kDa) and K9 (~63 kDa) [19, 20]. As known, K1 and K9 are fibrous proteins belonging to keratin family. In terms of structure, both of them can be divided into three domains: a highly conserved central rod domain acting as basic structural framework, an N-terminal head, and a C-terminal tail domain that are diverse in different proteins [21]. Of the matching peptides in Tables 1 and 2, 70% and 55% belong to conserved central rod domains of K1 and K9, respectively. These high matching rates imply that FP contains conserved domains similar to K1 and K9, and it should be the differences of head and tail domains that distinguish FP from K1 and K9. Therefore, we consider that FP is a novel fibrous protein homologous to K1 and K9. Since it was found from bivalve *S. grandis* ligament and identified for the first time, we named it solenin.

3.3. LC-MS-MS Results and Data Analysis. LC-MS-MS analysis shows the same results as MALDI. Similarly, no proteins were matched when searched against mollusc protein

database, but K1 and K9 were matched with 56.7% and 64.2% sequence coverage, respectively. These results again indicate that solenin is homologous to K1 and K9. Interestingly, we also found that a matrix protein from inner layer of *S. grandis* ligament has a high homology with K1, which gives us an important implication; that is, solenin is likely to assemble from matrix proteins (consider for publication elsewhere). It is known that matrix proteins from bivalve shells can control the formation of biominerals [22]. Excitingly, we have found that solenin can control pure aragonite formation at ambient condition in vitro, which suggests that solenin may serve as template for fabricating of biocomposite materials.

LC-MS-MS results also matched with repeat sequences mentioned (Tables 1 and 2). These sequences, with many repetitive “G,” are different from those of other fibrous or elastic proteins, such as “GGFGGMGGGX” of abductin [12], “GAGAGS,” “APGVGV,” and “GPGGG” of silk fibroin, elastin, and mussel byssal thread, respectively [23, 24]. However, repeat sequences of “GS” and “GSS” of solenin are identical to those of Lustrin A, an extracellular matrix protein from mollusc *Haliotis rufescens* shell [25]. These glycine- and serine-rich repeats previously had been found to form rubber-like “glycine loops” in Lustrin A and keratins to give them elastic and flexible properties [25, 26]. Such

TABLE 1: Search result of FP identified by MALDI-TOF-TOF-MS, matching keratin, type II cytoskeletal 1 [*Pan troglodytes*], NCBI database ID: gi|160961491.

Calculated mass	Observed mass	\pm ppm	Position	Peptide sequence ^{a,b}
973.5312	973.572	42	396–403	IEISELNR
1033.516	1033.5568	39	479–487	TLLEGEESR
1065.5211	1065.5497	27	351–359	AQYEDIAQK
1092.5028	1092.5533	46	596–609	GSGGGSSGGSIGGR
1179.6005	1179.6487	41	372–381	YEELQITAGR
1277.71	1277.7668	44	468–478	LALDLEIATYR
1302.7151	1302.7572	32	339–350	SLDLSIAAEVK
1340.6692	1340.719	37	360–371	SKAEAESLYQSK
1393.7322	1393.7858	38	273–284	TNAENEFVTIKK
1475.7489	1475.8197	48	207–218	WELLQQVDTSTR
1475.7853	1475.8197	23	195–206	FLEQQNQVLQTK
1539.7836	1539.8457	40	456–467	LLRDYQELM*NTK
1638.8599	1638.9277	41	181–194	SLNNQFASFIDKVR
1657.7928	1657.8588	40	13–29	SGGGFSSGSAGIINYQR
1708.7131	1708.7843	42	46–65	FSSCGGGGSGFAGGGF GSR
1716.8511	1716.9194	40	413–427	QISNLQSSISDAEQR
1993.9825	1994.0464	32	618–637	SSGSSSVKVFSTTYSGVTR
2150.0776	2150.1382	28	219–235	THNLEPYFESFINNLR
2383.9517	2384.0327	34	514–544	GGGGGGY GSGSSYSGGGSYSGGGGGGGR
3312.3079	3312.3784	21	545–583	GSYSGGGSSYSGGGSYSGGGGGGHGSYSGSSSGGYR

^aM*: oxidized methionine.

^bBold peptides are the repeat sequences.

TABLE 2: Search result of FP identified by MALDI-TOF-TOF-MS, matching keratin, type I cytoskeletal 9-like [*Pongo abelii*], NCBI database ID: gi|297716097.

Calculated mass	Observed mass	\pm ppm	Position	Peptide sequence ^{a,b}
913.4084	913.4358	30	238–244	MTLDDFR
982.4337	982.4608	28	35–46	FSS SGGGGGGGR
1060.5634	1060.5917	27	229–237	TLLDIDNTR
1074.5215	1074.5509	27	5–13	QFSSSYLSR
1157.5909	1157.6195	25	255–265	QGVDAINGLR
1232.5978	1232.6311	27	14–29	SGGGGGGLGSGGSIR
1235.5287	1235.556	22	47–59	FSSSSGYGG GSSR
1323.6725	1323.6975	19	245–254	IKFEM*EQNLR
1867.9219	1867.9476	14	326–340	TLNDM*RQEYEQLIK
1966.0604	1966.0665	3	379–395	HGVQELEIELQSLK
2705.1609	2705.1836	8	64–95	GGGGSFGYSYGGG SGGGFSASSLGGGFGGGRGGGGSGFY SYGGG SGGGFSASSLGGGFGGGR

^aM*: oxidized methionine.

^bBold peptides are the repeat sequences.

loops should also be present in solenin as it is homologous to keratin and contains “GS” and “GSS” repeats. Besides, phenylalanine (F) and tyrosine (Y) residues are involved in these repeat domains (Tables 1 and 2); their aromatic side chains interaction will contribute to the formation of “glycine loops” (Figure 4). These loops may give solenin excellence elastic and flexible properties to withstand tensile stress caused by repeating opening and closing of the shell valves in vivo.

3.4. FTIR Spectrum and Secondary Structure Analysis. FTIR spectrum (Figure 5(a)) of solenin has been discussed in our previous study [16]. Here, secondary structure of solenin was analyzed by curve-fitting of amide I band of the spectrum, since the band is frequently used for secondary structure analysis [27, 28]. Based on previous studies [17, 18] and the curve-fitting results (Figure 5(b)), peaks of Gaussian curve were ascribed to β -sheet, β -turn, α -helix, and disordered structure, respectively. Quantitative analysis results indicate

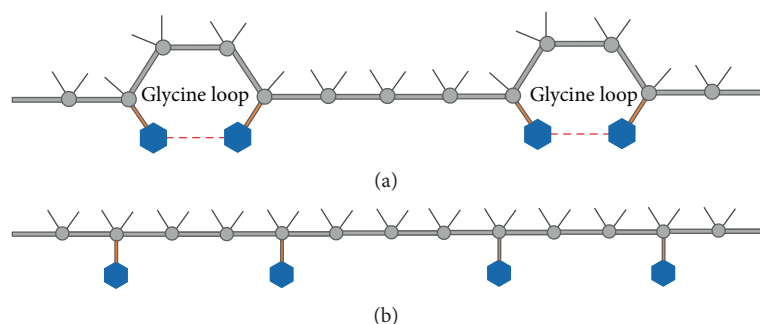


FIGURE 4: Schematic diagram of formed (a) and unfolded glycine loops (b). Blue hexagons represent benzene rings and red dot lines represent the interaction of benzene rings side chains of phenylalanine and tyrosine.

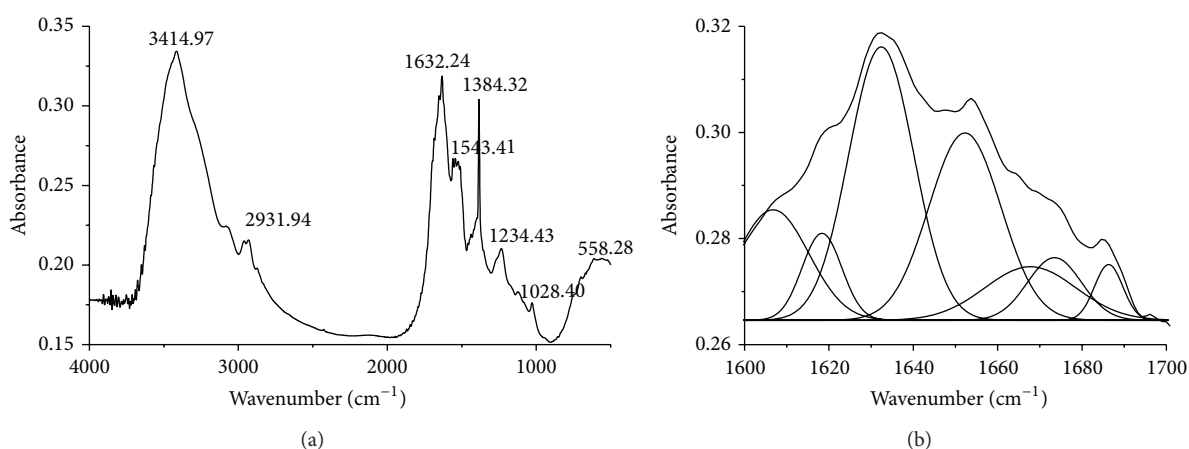


FIGURE 5: FTIR spectra of solenin. (a) Original spectrum and (b) Gaussian line shapes of amide I region, 1700–1600 cm^{-1} ((a) adapted from Figure 7(b), [16], with permission).

that solenin is mainly composed of β -sheet structure (41.8%), with 16.2% β -turn, 26.5% α -helix, and a small amount of disordered structure (9.8%). This high β -sheet content contradicts K1 and K9 (mainly with α -helix structure), which confirms that solenin is not K1 or K9. It also implies that the head or tail domain of solenin is mainly composed of β -sheet structure since its central rod domain is similar to K1 and K9. This secondary structural feature is similar to silk [29, 30] and K58 [14]. It may endow solenin with high performance of tensile strength, just like silk; the strong fibrous protein having high tensile strength of 0.6 GPa [31] is mainly made up of β -sheet structures.

Although the tensile strength of solenin has not been determined yet for the lack of instrument, there is no doubt that solenin is subjected to repeating tensile stress with frequent closing of shell valves in vivo [16]. This implies that solenin must have superior tensile strength to withstand long-term successive rapid movement of shell valves to accommodate the rapid burrowing life habit of this species [16, 32]. In addition, solenin presents excellent solvent resistance property similar to K58 [14], which implies that the protein may serve as a good template for fabricating of biomaterials.

4. Conclusions

Solenin is a novel fibrous protein homologous to K1 and K9. It is not constructed by microfibrils and is different from collagen. Its high content of β -sheet structure (41.8%) may endow solenin with excellent tensile strength and solvent resistance property. Insight into the structure of this intriguing natural fibrous protein will provide a new template for fabricating of bioinspired materials.

Conflict of Interests

The authors declare that there is no conflict of interests regarding the publication of this paper.

Acknowledgments

The authors thank Qiang Fu, Ming Zhu Li, and Dr. Jin Zi Wang for useful discussions. The authors also acknowledge Guangxi Key Lab of Subtropical Agricultural Bio-resource Conservation and Utilization for MALDI-TOF-TOF determination. Thanks also are given to the Research Centre

for Proteome Analysis, Key Lab of Proteomics, Institute of Biochemistry and Cell Biology, Shanghai Institutes for Biological Sciences, and Chinese Academy of Sciences, for LC-MS-MS contributions. This work was supported by the Natural Science Foundation of Guangxi China (Grant no. 2013 GXNSFAA019052).

References

- [1] P. Fratzl, *Collagen Structure and Mechanics*, Springer Science Business Media, LLC, New York, NY, USA, 2008.
- [2] P. R. Shewry, A. S. Tatham, and A. Bailey, *Elastomeric Proteins: Structures, Biomechanical Properties, and Biological Roles*, Cambridge University Press, New York, NY, USA, 2003.
- [3] T. Scheibel, *Fibrous Proteins: Molecular Biology Intelligence Unit*, Landes Bioscience, Austin, Tex, USA, 2008.
- [4] J. H. Waite, X. X. Qin, and K. J. Coyne, "The peculiar collagens of mussel byssus," *Matrix Biology*, vol. 17, no. 2, pp. 93–106, 1998.
- [5] K. J. Coyne, X. Qin, and J. H. Waite, "Extensible collagen in mussel byssus: a natural block copolymer," *Science*, vol. 277, no. 5333, pp. 1830–1832, 1997.
- [6] M. J. Harrington and J. H. Waite, "Short-order tendons: liquid crystal mesophases, metal-complexation and protein gradients in the externalized collagens of mussel byssal threads," in *Fibrous Proteins, Molecular Biology Intelligence Unit*, T. Scheibel, Ed., Landes Bioscience, Austin, Tex, USA, 1st edition, 2008.
- [7] A. F. Sartori and A. D. Ball, "Morphology and postlarval development of the ligament of *Thracia phaseolina* (bivalvia: Thraciidae), with a discussion of model choice in allometric studies," *Journal of Molluscan Studies*, vol. 75, no. 3, pp. 295–304, 2009.
- [8] H. Ehrlich, *Biological Materials of Marine Origin: Invertebrates*, vol. 1 of *Biologically-Inspired Systems*, Springer, Dordrecht, The Netherlands, 1st edition, 2010.
- [9] G. A. Kahler, R. L. Sass, and F. M. Fisher Jr., "The fine structure and crystallography of the hinge ligament of *Spisula solidissima* (Mollusca: Bivalvia: Mactridae)," *Journal of Comparative Physiology*, vol. 109, no. 2, pp. 209–220, 1976.
- [10] R. E. Kelly and R. V. Rice, "Abductin: a rubber-like protein from the internal triangular hinge ligament of Pecten," *Science*, vol. 155, no. 3759, pp. 208–210, 1967.
- [11] Y. Kikuchi, O. Tsuchikura, M. Hiram, and N. Tamiya, "Desmosine and isodesmosine as cross-links in the hinge-ligament protein of bivalves. 3,3'-Methylenebistirosine as an artefact," *European Journal of Biochemistry*, vol. 164, no. 2, pp. 397–402, 1987.
- [12] Q. Cao, Y. Wang, and H. Bayley, "Sequence of abductin, the molluscan "rubber" protein," *Current biology*, vol. 7, no. 11, pp. 677–678, 1997.
- [13] B. Bochicchio, A. Pepe, and A. M. Tamburro, "Circular dichroism studies on repeating polypeptide sequences of abductin," *Chirality*, vol. 17, no. 7, pp. 364–372, 2005.
- [14] Z. Huang and G. Zhang, "Identification and secondary structure analysis of a keratin-like fibrous protein discovered in ligament of the bivalve *Siliqua radiata*," *Biochemistry*, vol. 76, no. 11, pp. 1227–1232, 2011.
- [15] Z. Huang and G. Zhang, "Biomimetic synthesis of aragonite nanorod aggregates with unusual morphologies using a novel template of natural fibrous proteins at ambient condition," *Crystal Growth & Design*, vol. 12, no. 4, pp. 1816–1822, 2012.
- [16] H. Zengqiong and Z. Gangsheng, "A new structural model of bivalve ligament from *Solen grandis*," *Micron*, vol. 42, no. 7, pp. 706–711, 2011.
- [17] J. M. Cardamone, "Investigating the microstructure of keratin extracted from wool: peptide sequence (MALDI-TOF/TOF) and protein conformation (FTIR)," *Journal of Molecular Structure*, vol. 969, no. 1–3, pp. 97–105, 2010.
- [18] J. T. Pelton and L. R. McLean, "Spectroscopic methods for analysis of protein secondary structure," *Analytical Biochemistry*, vol. 277, no. 2, pp. 167–176, 2000.
- [19] <http://www.ncbi.nlm.nih.gov/protein/160961491>.
- [20] <http://www.ncbi.nlm.nih.gov/protein/297716097>.
- [21] I. Szeverenyi, A. J. Cassidy, W. C. Cheuk et al., "The human intermediate filament database: comprehensive information on a gene family involved in many human diseases," *Human Mutation*, vol. 29, no. 3, pp. 351–360, 2008.
- [22] T. Takeuchi, I. Sarashina, M. Iijima, and K. Endo, "In vitro regulation of CaCO₃ crystal polymorphism by the highly acidic molluscan shell protein Aspein," *FEBS Letters*, vol. 582, no. 5, pp. 591–596, 2008.
- [23] Y. Ner, J. A. Stuart, G. Whited, and G. A. Sotzing, "Electrospinning nanoribbons of a bioengineered silk-elastin-like protein (SELP) from water," *Polymer*, vol. 50, no. 24, pp. 5828–5836, 2009.
- [24] A. S. Tatham and P. R. Shewry, *Elastomeric Proteins: Structures, Biomechanical Properties, and Biological Roles*, Edited by P. R. Shewry, A. S. Tatham, A. Bailey, Cambridge University Press, New York, NY, USA, 1st edition, 2003.
- [25] X. Shen, A. M. Belcher, P. K. Hansma, G. D. Stucky, and D. E. Morse, "Molecular cloning and characterization of Lustrin A, a matrix protein from shell and pearl nacre of *Haliotis rufescens*," *Journal of Biological Chemistry*, vol. 272, no. 51, pp. 32472–32481, 1997.
- [26] M. Suzuki and H. Nagasawa, "The structure-function relationship analysis of Prismaticin-14 from the prismatic layer of the Japanese pearl oyster, *Pinctada fucata*," *The FEBS Journal*, vol. 274, no. 19, pp. 5158–5166, 2007.
- [27] A. Barth, "Infrared spectroscopy of proteins," *Biochimica et Biophysica Acta—Bioenergetics*, vol. 1767, no. 9, pp. 1073–1101, 2007.
- [28] J. Kong and S. Yu, "Fourier transform infrared spectroscopic analysis of protein secondary structures," *Acta Biochimica et Biophysica Sinica*, vol. 39, no. 8, pp. 549–559, 2007.
- [29] L. Römer and T. Scheibel, *Fibrous proteins: Molecular Biology Intelligence Unit*, edited by T. Scheibel, Landes Bioscience, Austin, Tex, USA, 1st edition, 2008.
- [30] G. A. Petsko and D. Ringe, *Protein Structure and Function: From Sequence to Consequence*, Science Press, London, UK, 2007.
- [31] M. A. Meyers, P. Y. Chen, A. Y. M. Lin, and Y. Seki, "Biological materials: structure and mechanical properties," *Progress in Materials Science*, vol. 53, article 112, 2008.
- [32] E. R. Trueman, "The dynamics of burrowing in *Ensis*," *Proceedings of the Royal Society B*, vol. 1166, pp. 459–476, 1967.

Research Article

Alumina Membrane with Hour-Glass Shaped Nanochannels: Tunable Ionic Current Rectification Device Modulated by Ions Gradient

Shengnan Hou, Qinjin Wang, Xia Fan, Zhaoyue Liu, and Jin Zhai

Key Laboratory of Bio-Inspired Smart Interfacial Science and Technology of Ministry of Education, School of Chemistry and Environment, Beihang University, Xueyuan Road, No. 37, Haidian District, Beijing 100191, China

Correspondence should be addressed to Xia Fan; fanxia@buaa.edu.cn and Jin Zhai; zhajin@buaa.edu.cn

Received 7 May 2014; Accepted 27 May 2014; Published 19 June 2014

Academic Editor: Hao Bai

Copyright © 2014 Shengnan Hou et al. This is an open access article distributed under the Creative Commons Attribution License, which permits unrestricted use, distribution, and reproduction in any medium, provided the original work is properly cited.

A new alumina membrane with hour-glass shaped nanochannels is reported using the double-side anodization method and the subsequently in situ pore opening procedure, which is applied to develop the tunable ionic current rectification devices that were modulated by ions gradient. By regulating the pH gradient, tunable ionic current rectification properties which are mainly dependent on the asymmetric surface charge density or polarity distribution on the inner walls of the nanochannels can be obtained. The enhanced ionic current rectification properties were presented due to the synergistic effect of the voltage driven ion flow and diffusion driven ion flow with the application of pH and electrolyte concentration gradients. Therefore, such specific alumina nanochannels would be considered as a promising candidate for building bioinspired artificial ion channel systems.

1. Introduction

In living systems, with proton migration from inward to outward of biological membranes, the transmembrane proton gradient is generated and applies essential driving force for oxidative phosphorylation to promote the formation of adenosine triphosphate (ATP), which guarantees the energy requirement of life activities [1, 2]. This phenomenon demonstrates that ions gradient plays an important role in the transmembrane ion transport behaviors [3, 4]. It inspires that, for artificial nanopores and nanochannels, ions gradient can be considered as an external parameter to regulate ionic transport behaviors [5–10], build nanofluidic devices [11–13], or construct photoelectric conversion systems [14–16]. For example, Jiang's group reported a photoelectric conversion system based on smart gating proton driven nanochannels whose inspiration came from photoelectric conversion of retina [17]. García-Giménez et al. discovered that the applied pH gradient originated strong asymmetries in the distribution of fixed charges along the bacterial porin OmpF, a biological nanopore, resulting in rectified ion transport behavior [18]. This behavior shows the preferential direction for ion flow in synthetic nanochannels, which is observed

as a nonlinear current-voltage signal [19]. Nanofluidic diode system was fabricated using single conically shaped nanopore by manipulating pH gradient and an enhanced current rectification was obtained comparing with the condition that there exists homogeneous electrolyte [20]. The concentration gradient dependent ionic current rectifications were reported in charged nanopores [21, 22] and homogeneous silica nanochannels [23, 24] as well. Recently, systematic studies on rectified ion transport in artificial nanochannels with both pH gradient and concentration gradient driven ion flow are of significant interests [25].

Alumina nanochannels possess many particular advantages such as repeatability, chemical stability, high pore densities, and flexibility in controlling the geometry, which makes this inorganic nanochannel as a desired candidate for artificial ion channels [26–28]. Recently, extensive efforts have been expended on controlling the asymmetric geometric structures [29, 30] and surface properties [31] to obtain the novel nanofluidic devices based on artificial alumina nanochannels. Our group has experimentally demonstrated the diode performance of the branched alumina nanochannels, which are mainly dependent on the natural asymmetric

effect of the branched structures and the surface-charge distribution on inner walls [32]. By breaking the symmetry of the cylindrical alumina nanochannels and introducing amine functional groups, a modulated rectification behavior that is responsive to pH stimuli has been constructed [33]. However, these alumina nanochannels were nearly prepared by one-side anodization process and Al substrate as well as barrier oxide layers should be removed after anodization. To develop advanced functional nanochannels, making innovation on internal configurations of alumina nanochannels is still a huge challenge.

The anodization technique allows control over the shape of the nanochannels, and in this work a double-side anodization process was applied together with an in situ pore opening procedure. A new alumina membrane with hour-glass shaped nanochannels is fabricated. Similar to previously reported single double-conical shaped nanochannel based on organic materials [34, 35], these unique nanochannels are composed of two segments of asymmetric nanochannels, whose surface properties can be simultaneously or separately modulated by external stimuli, such as pH and concentration. Herein, we utilize the specific symmetric hour-glass shaped alumina nanochannels with asymmetric ion gradients to adjust diverse surface charge properties in order to develop the asymmetric nanochannel systems that provide variety control over both the pH- and concentration-tunable ionic rectification properties.

2. Experimental

2.1. Alumina Nanochannel Fabrication Process. The hour-glass shaped alumina nanochannels were prepared by a double-side anodization method with an in situ pore opening process. Al foil (99.999% pure, 0.1 mm thick) was firstly cleaned by acetone, ethanol, and MilliQ water (18.2 M Ω) in sequence and then was electropolished in a mixture solution of HClO₄ and ethanol (1:4 in volume ratio) at 4°C under the voltage of 17 V. The first anodization step was carried out in a 0.3 M oxalic acid solution at 5°C. Each side of the Al foil was separately anodized for 1 h and then the resulting porous oxide layer was etched from Al substrate in a solution containing 6 wt% phosphoric acid and 3.5 wt% chromic acid at 90°C for 4 h. In the second step, the corresponding Al substrate with highly ordered hemispherical concaves was anodized under the same electrolyte conditions as the first anodization. The duration of the second anodization was varied from 7 to 9.2 h in order to investigate the effect of anodization time on the growth behavior of the Al₂O₃ nanotube arrays. Here, two layers of Al₂O₃ nanotube arrays synchronously grew on both sides of the Al substrate that contact the electrolyte during anodization process. When the anodized current decreased nearly to zero at 9.2 h, Al substrate was totally anodized, and two highly ordered Al₂O₃ nanotube layers were fabricated with a barrier oxide layer at each bottom of the nanotubes. These insulating layers would block direct electrical and chemical contact between the two nanotube layers. After anodization, as-fabricated Al₂O₃ nanotubes membrane was still immersed in electrolyte oxalic

acid in order to penetrate the two barrier oxide layers. This in situ pore opening time should be controlled within 30 min for forming the hour-glass shaped alumina nanochannels, which would be used as an optional candidate for artificial ion channels. The detailed microstructure of the as-prepared alumina nanotubes and nanochannels was characterized with scanning electron microscopy (SEM, Hitachi, S4300).

2.2. Current-Voltage (*I-V*) Measurement. The ionic transport behaviors of hour-glass shaped alumina nanochannels under the pH or ionic concentration gradient conditions were investigated in an electrochemical cell. As shown in Figure S1 (supporting information in Supplementary Material available online at <http://dx.doi.org/10.1155/2014/564694>), alumina nanochannels membrane was mounted between two half-cells. Potassium chloride (KCl) aqueous solutions with different pH or ion concentrations were chosen as the electrolyte. The pH of the electrolyte varied from 3.0 to 11.0, which was adjusted with 0.1 M hydrochloric acid or 0.1 M potassium hydroxide solution. The concentrations of KCl electrolyte varied from 0.1 mM to 100 mM. Ag/AgCl electrodes were settled in each half-cell to apply the desired transmembrane potential. The anode faced the left side of the nanochannels and the cathode faced the right side in all measurements. *I-V* curves were measured using a Keithley 6487 picoammeter/voltage source. The voltage was stepped between -2 V and +2 V with 200 mV steps, lasting for 5 s.

3. Results and Discussions

3.1. Alumina Nanochannel Characterization. As described in experimental process, the fabrication process of the hour-glass shaped alumina nanochannel is schematically illustrated in Figure 1, which consists of five steps. Using the double-side anodizing process (from step (a) to step (d)), the double-layer alumina nanotubes were firstly fabricated with the opposite growth direction. However, there are two insulating barrier oxide layers between the bottoms of the two nanotube layers. The in situ pore opening procedure (step (e)) was carried out immediately after the anodization process. The hour-glass shaped alumina nanochannels were finally obtained. The two opening sides have the relatively large diameters depending on the anodization voltage, while the center of the nanochannels that etched from the barrier layers have the small diameters determined by the in situ pore opening time.

3.2. Microstructure and Morphology of Alumina Nanochannels. In our work, the effect of anodization time on the growth behavior of the Al₂O₃ nanotube arrays was investigated. As shown in Figures 2(a)–2(e), two layers of Al₂O₃ nanotubes synchronously grew on both sides of the Al substrate with the growth time about 7 h, 8 h, 8.5 h, 9 h, and 9.2 h, respectively. The thickness of the membrane for all samples is controlled about 95 μ m. With the increase in anodization time, the thickness of the alumina nanotube layers increased gradually from 78.2 μ m to 95 μ m, while the thickness of Al substrate decreased correspondingly. When

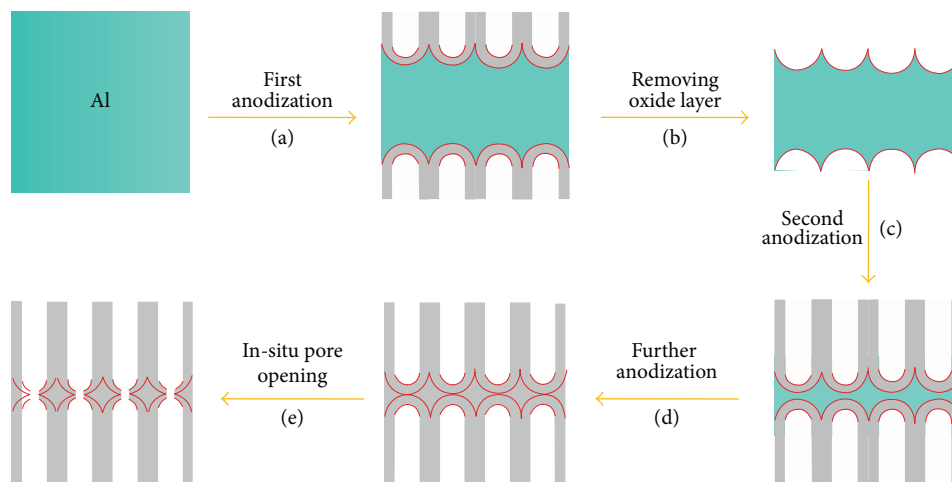


FIGURE 1: Schematic illustration of the experimental method for fabricating hour-glass shaped alumina nanochannels membrane.

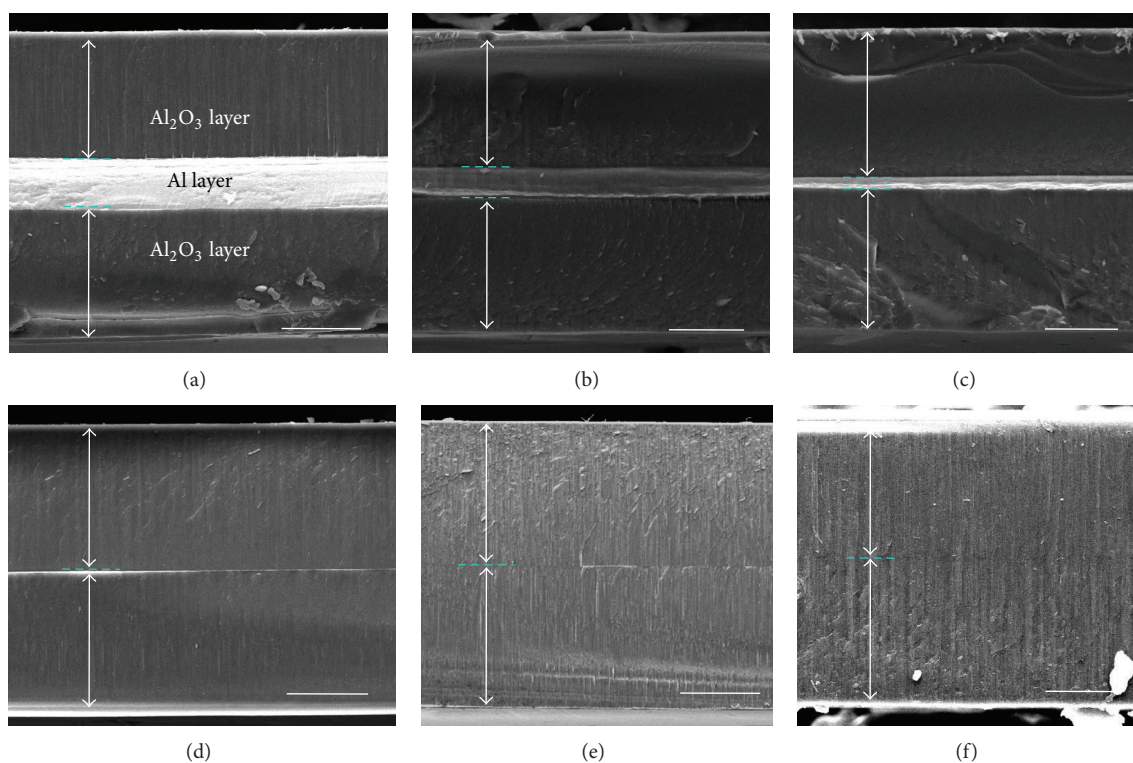


FIGURE 2: The cross-sectional SEM images of (a–e) the Al_2O_3 nanotube layers with different second-step anodized time, which would be regulated from 7 h, 8 h, 8.5 h, and 9 h to 9.2 h, respectively. The thickness of Al_2O_3 nanotube layers increased when the anodized time increased, while the thickness of Al substrate decreased. When the anodization time was 9.2 h, the Al substrate was completely anodized. The double-layer alumina nanotubes were fabricated and the boundary between the two nanotube layers became vague after 30 min in situ pore opening process (f). Scale bar is $25\ \mu\text{m}$.

the anodization time was 9 h (Figure 2(d)), Al substrate decreased to be a slice, with the thickness of about 600 nm. And finally the Al substrate was completely anodized at 9.2 h (Figure 2(e)). Then after 30 min in situ pore opening process, the boundary between two layers of alumina nanotubes became vague (Figure 2(f)). At this time, the as-fabricated alumina membrane exhibited a good transparency (Figure

S2). Therefore, based on this unique phenomenon, we further investigated the detailed microstructure of the double-layer Al_2O_3 nanotubes before and after the in situ pore opening procedure.

As shown in Figures 3(a) and 3(b), pore diameters of as-prepared double-layer alumina nanotubes are about 45 nm at both top and bottom opening sides. Two barrier layers

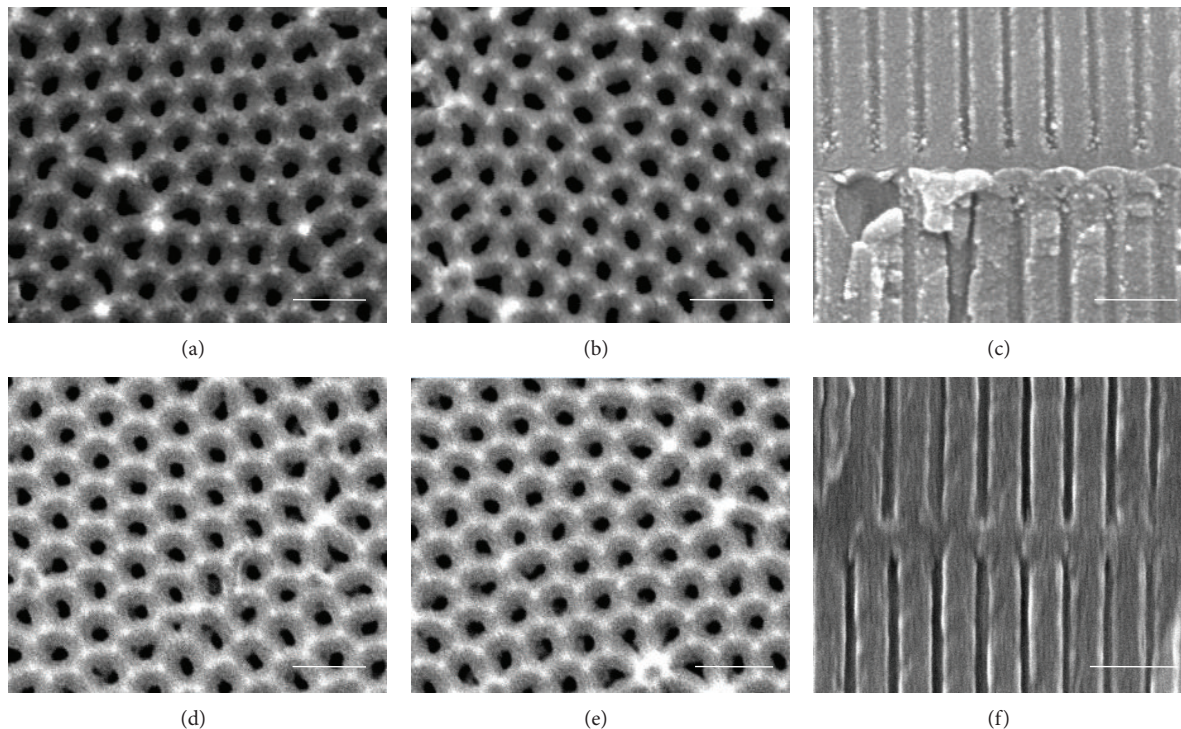


FIGURE 3: SEM images from the top opening side, bottom opening side, and the cross-sectional viewing of (a–c) the double-layer Al_2O_3 nanotubes and (d–f) hour-glass shaped alumina nanochannels, respectively. Both the nanotube and the nanochannel have the pore diameters at top and bottom opening sides about 45 nm. At the center of the nanotube membrane, two barrier layers closely contact and the ion transportation would be blocked. With the in situ barrier layer etching for about 30 min, hour-glass shaped nanochannel was fabricated, which has a small pore at the central region of channel with the diameter of about 15 nm. Scale bar is 200 nm.

closely contact at the center of the nanotubes membrane (Figure 3(c)). In our controlled in situ pore opening process, the inner walls of the channels would not be etched (Figures 3(d) and 3(e)), while the barrier layers were preferentially penetrated. It is clear from Figure 3(f) that an ionic confined-transportation region is observed within the nanochannels with the pore diameter about 15 nm. This in situ pore opening process is different from the wet-chemical etching methods that were usually used [36–38]. In anodization process, nanotubes growth occurred at the barrier oxide layers with the dissolving and anodizing process of Al substrate [39]. The barrier layers have the relatively higher reaction activity than the inner walls. When the anodization reaction just stopped, the alumina nanotubes membrane is nearly impassable and only a very low ion transport current was detected by I - V measurement (Figure S3). And then, the barrier layers would be preferably dissolved in the residual electrolyte solution because the pH value is about 0.99. Thus, the partly dissolved barrier layers resulted in the forming of hour-glass shaped nanochannels. It is noted that the inner walls can also be etched with the increase in etching time, which results in the disappearance of the confined spaces. Here, on the basis of our experimental results, the optimal in situ barrier layer etching time was determined to be 30 min for fabricating the hour-glass shaped alumina nanochannels (Figure 3(f)), which provided a desired transmembrane ionic current as the previously reported alumina nanochannels.

3.3. Influence of pH and Concentration Gradient on the Tunable Ionic Current Rectification Performances. As we know, alumina is an amphoteric material with the isoelectric point (pI) about 8.5 and the surface charges could be modulated by pH stimuli [40]. Here we present the pH-gradient dependent ionic current rectification in as-prepared hour-glass shaped alumina nanochannels. With the adjusting of pH values, the nanochannels surface carried positive (Al-OH_2^+) or negative charges (Al-O^-) due to the protonation or deprotonation of the terminated Al-OH surface. Thus, Figures 4(a) and 4(b) show the I - V curves of hour-glass shaped alumina nanochannels with 1 mM KCl solution under different pH gradient stimuli. The corresponding surface charge density or polarity distributions of the inner walls of alumina nanochannels are schematically represented in Figures 4(c) and 4(d) with the assumption that solutions at two half-cells meet at the central confined space of the hour-glass nanochannels. When the value of solution pH_L was 4.5 in the left half-cell, the values of pH_R in the right half-cell varied from 4.5 to 11.0 (Figures 4(a) and 4(c)). The pH gradients could be considered as four different conditions owing to the different surface charge properties on the inner walls of hour-glass shaped nanochannels. (i) Symmetric acid-acid: two asymmetric channel segments carry the same positive charges when pH 4.5 is below the pI. Undoubtedly, the linear I - V curve can be obtained in such symmetric hour-glass shaped alumina nanochannels, which means it does not rectify. (ii) Asymmetric acid-acid: with the

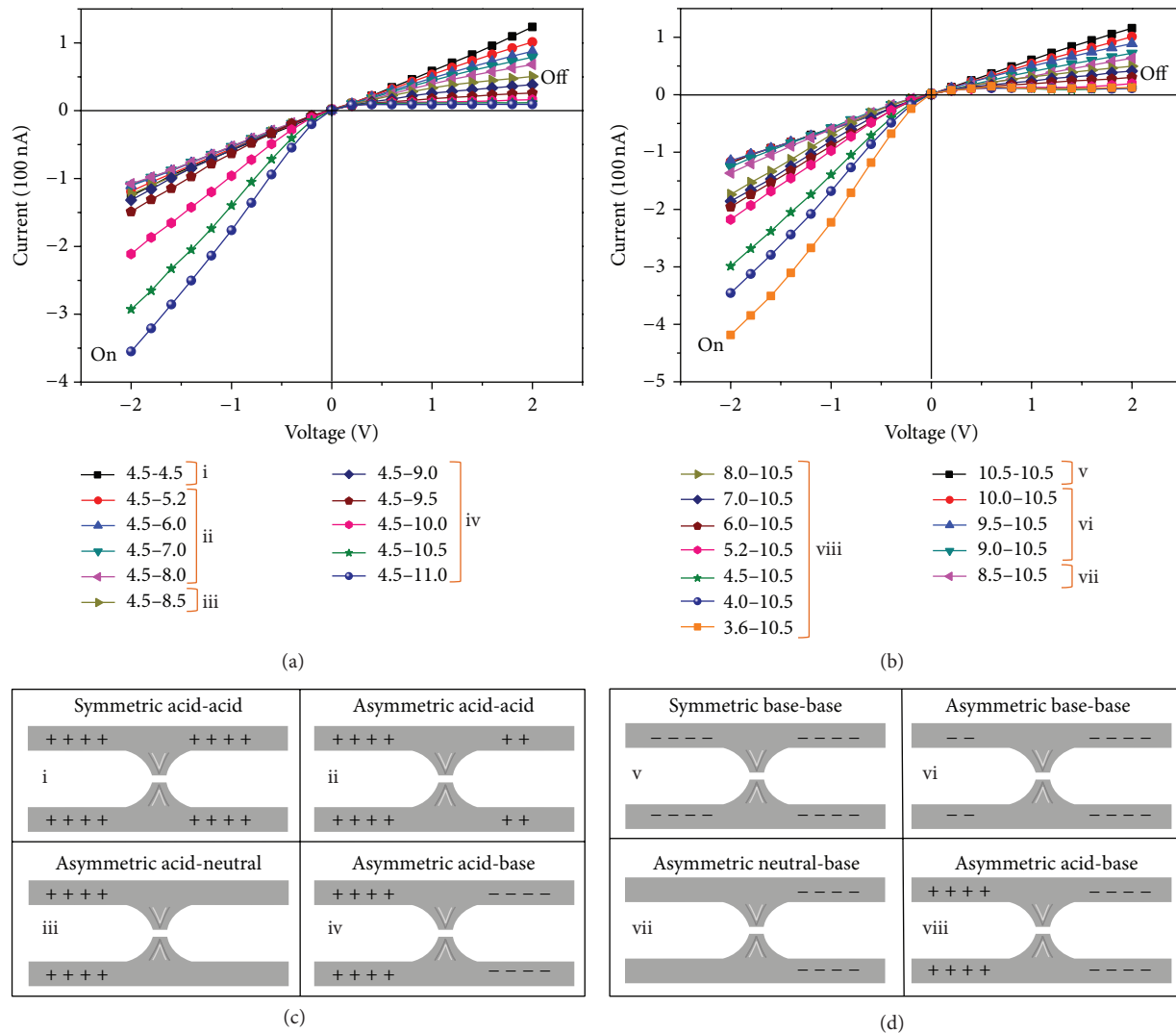


FIGURE 4: Ionic transport properties of the hour-glass shaped alumina nanochannels measured in 1 mM KCl solution with pH gradient stimuli. (a) I - V curves with pH_L 4.5 and pH_R varying from 4.5 to 11.0. (b) I - V curves with pH_R 10.5 and pH_L varying from 3.6 to 10.5. (c) and (d) schematic representation of the surface charge distribution under symmetric/asymmetric pH stimuli.

increase in pH_R values, homogeneous discontinuous positive charge density between two nanochannel segments is created. The nanochannels show the rectification characteristics as follows: a high conducting state (“on”) at negative voltage and a low conducting state (“off”) at positive voltage. Meanwhile, with the escalated pH gradient, the asymmetry of surface charge density distribution is enhanced, which contributes to the increase in ionic current at “on” state and the decrease in ionic current at “off” state. (iii) Asymmetric acid-neutral: only one asymmetric channel segment has the positive charges, which resulted in the nonuniform chemical composition on the symmetric nanochannels. The ionic transport condition in our experiment is relatively similar to the diode made with proteins in silicon nanochannels [41]. As a result, the rectifying occurred. (iv) Asymmetric acid-base: hour-glass shaped nanochannels have the heterogeneous surface charges, which resulted in a positive-negative charge junction

like a bipolar diode [42, 43]. At negative voltage, both K^+ and Cl^- are driven toward the junction. Ions accumulated inside the electric double layer of the nanochannels dependent on the strong interaction between charged walls and ions in solution; thus, the nanochannels are the “on” state. While at positive voltage, the depletion of ions induces a low ionic current and the nanochannels are the “off” state. As a consequence, from the state (i) to state (iv), current at negative voltages dramatically increased, while it decreased at positive voltages in sequence. The best ionic rectification property was exhibited in state (iv).

Further, we investigated the rectification behaviors of hour-glass shaped alumina nanochannels with another kind of pH gradient stimuli that the pH_L values changed from 10.5 to 3.6, while the pH_R was fixed at 10.5 (Figures 4(b) and 4(d)). The pH gradients were also divided into four parts as described above including (v) symmetric base-base,

(vi) asymmetric base-base, (vii) asymmetric neutral-base, and (viii) asymmetric acid-base. The right segment nanochannels have the same negative surface charges, while the left segment nanochannels have the adjusted surface charges that vary from high negative, low negative, and neutral to positive following the pH values decreasing in sequence. It should be noted that the similar I - V curves were observed among states (i) and (v), states (ii) and (vi), states (iii) and (vii), and states (iv) and (viii), respectively. At states (vi) and (vii), the nanochannels especially exhibited the ion rectification with the same direction as states (ii) and (iii) because the surface charge polarity and the direction of the charge distribution were simultaneously reversed.

Rectification performance can be quantitatively represented by the value r , which is defined as the ratio between the currents measured at a voltage of the same amplitude but opposite polarity. In our case, the corresponding r is calculated by the absolute value of I (on state)/ I (off state), measured at ± 2 V applied potential. The tunable ionic rectification behavior has been represented in hour-glass shaped alumina nanochannels. Figure 5(a) shows the rectification performance of states (i), (ii), (iii), and (iv). In this case, r is 1.0 at state (i) for the symmetric pH solutions (4.5/4.5) and increases to reach the maximum value of 37.4 under the largest pH gradient (4.5/11.0) of state (iv). In Figure 5(b), when pH_R is fixed at 10.5, r is equal to 34.3 at state (viii) with asymmetric pH 3.6/10.5 stimuli and decreases to 1.0 at state (v) under the symmetric pH 10.5/10.5. So, with the increase in pH gradient, the ionic rectification behavior can be enhanced. Significant increase in rectification ratios especially is observed at states (iv) and (viii), which mainly depends on the opposite charge polarity on the asymmetric nanochannel segments. To inspect and verify the pH response of the two asymmetric alumina nanochannel segments, I - V properties of the hour-glass shaped nanochannels have been examined with asymmetric pH values changed simultaneously (Figure S4(a)). The rectification behavior can be modulated and the better rectification performance was obtained under the highest pH gradient of 3.0/11.0. The rectification ratio reaches the maximum value of 48.9 (Figure S4(b)).

Ionic concentration gradient has been identified as an important factor to influence rectification properties. We investigated the current rectification properties of hour-glass shaped alumina nanochannels under the modulating of both pH and ionic concentration gradient. Figure 6 shows the asymmetric I - V curves measured in KCl electrolyte with or without a different concentration gradient in an asymmetric acid-base solution with pH_L 5.2 and pH_R 10.0. We fixed an ionic concentration of 0.1 mM at one side and manipulated the different concentration (0.1, 1, 10, and 100 mM) at the other side. Here, ionic concentration is defined as C_L in acid solution, as well as C_R in basic solution. With the same ion concentration on both sides ($C_L = C_R = 0.1$ mM), the hour-glass shaped alumina nanochannels display an evidently asymmetric rectification behavior in the pH gradient solution. With the concentration gradient stimuli, the zero-volt current is nonzero because of the selective diffusion of the anions or cations. In addition, with the increase in the ionic concentration gradient, the negative ionic current

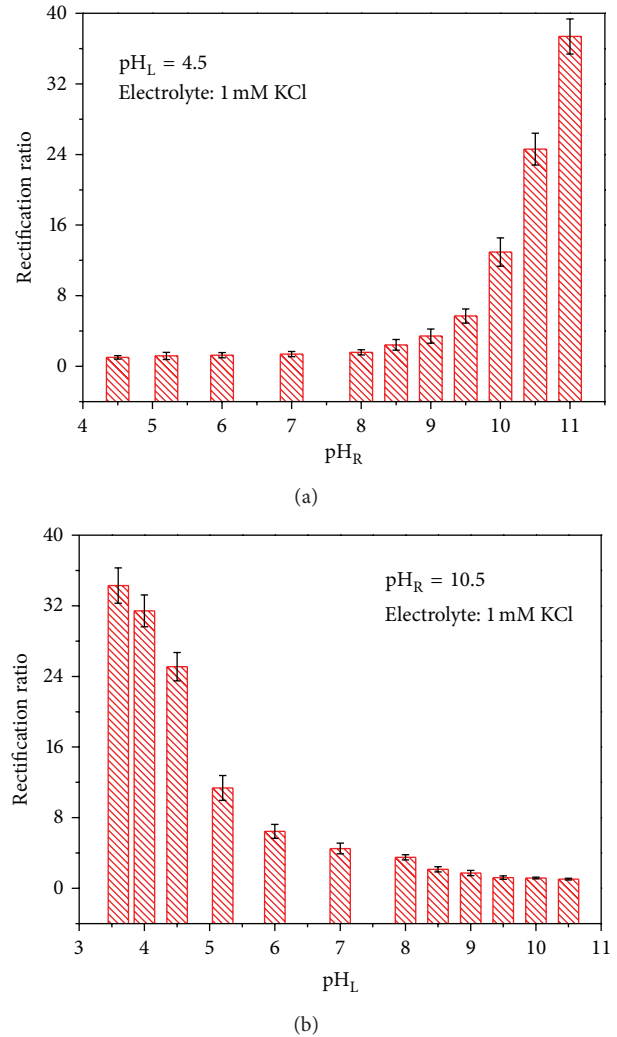


FIGURE 5: Ionic rectification ratio of the hour-glass shaped alumina nanochannels measured in 1 mM KCl with a series of pH gradients. (a) pH_L 4.5 and pH_R varied from 4.5 to 11.0. (b) pH_R 10.5 and pH_L varied from 3.6 to 10.5. With the increasing of pH gradient, the rectification ratios correspondingly increased.

monotonously remarkably increased (“on” state), while the positive ionic current slightly increased (“off” state).

Figure 7 illustrated how the hour-glass shaped alumina nanochannels operate under both pH and concentration gradients stimuli. Upon applying pH gradient, the ionic diode was formed, which consists of a junction between positively and negatively charged zones within the hour-glass shaped nanochannels. At the “on” state, the external voltage drives both cations (e.g., K^+) and anions (e.g., Cl^-) from the bulk solution through the nanochannel. The nanochannel has no ion selectivity and the current is carried by both cations and anions. When low ionic concentration is fixed at the acid side ($C_L < C_R$), the direction of diffusive K^+ ion flow is consistent with the voltage driven K^+ ion flow at “on” state (up-left in Figure 7), while the direction of diffusive Cl^- ion flow is opposite to the voltage driven Cl^- ion flow. As a result, the diffusion rate of K^+ along its concentration gradient

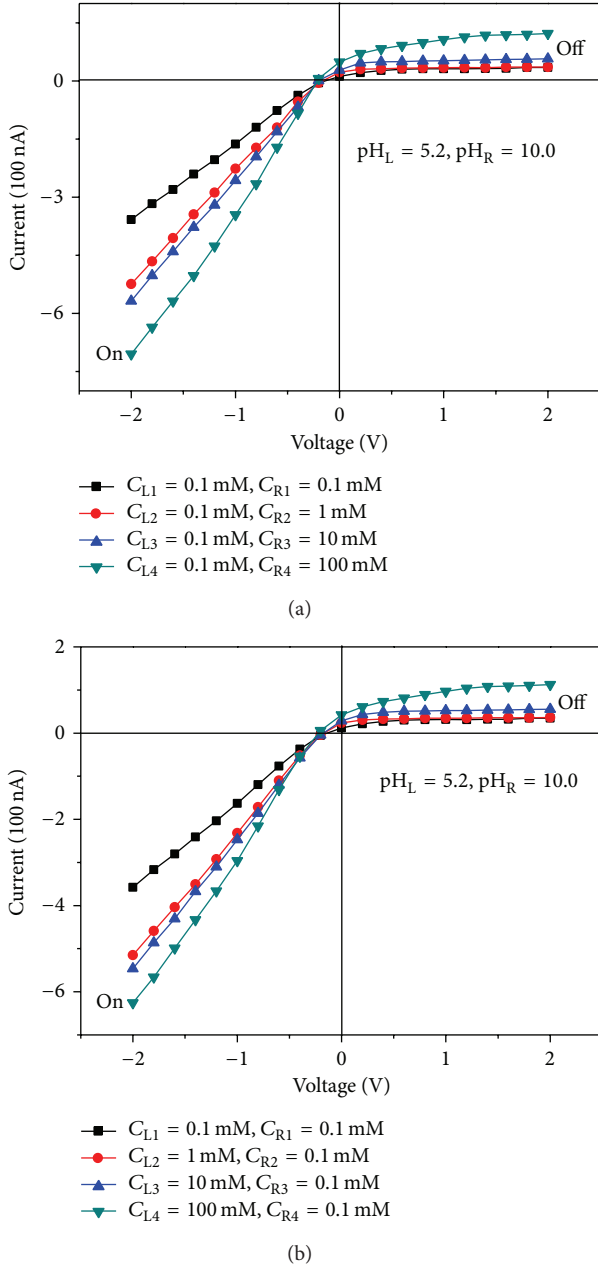


FIGURE 6: Concentration-gradient dependent ionic current rectification of hour-glass shaped alumina nanochannel in an asymmetric acid-base solution of $\text{pH}_L = 5.2$ and $\text{pH}_R = 10.0$. I - V curves measured in KCl electrolyte with or without a different concentration gradient. The experimental configurations are (a) $C_L = 0.1 \text{ mM}$ and C_R varied from 0.1 to 100 mM. (b) $C_R = 0.1 \text{ mM}$ and C_L changed from 0.1 to 100 mM.

(from the base side to the acid side) across the membrane is higher than the diffusion rate of Cl^- , which causes the nonzero zero-volt current. More K^+ ions are supplied from the bulk at base side than that in symmetric concentration solution and then get transported through the channel by the driven force including external bias and concentration gradient. Therefore, this forward concentration gradient

contributes to a high ionic current at “on” state. At the “off” state, the voltage polarity is reversed and external bias drives ions out of the nanochannel. Under the concentration gradient stimuli, few ions can be replenished into the ion-depleted zone at base side (bottom-left in Figure 7). The diffusion of Cl^- ions from base side to the acid side would possibly occur, which results in a slightly increase in ionic current.

When low ionic concentration is fixed at base side (up-right in Figure 7), the reversed concentration gradient ($C_L > C_R$) excited a higher diffusion rate of Cl^- across the membrane from the acid side to the base side than the diffusion rate of K^+ at “on” state, which remarkably promotes the ionic currents in the same direction with the voltage driven ion flow. At the “off” state, the ion-depleted zone will be filled with the excess K^+ ions that originate from the high concentration gradient at the acid solution (bottom-right in Figure 7). Similarly, the diffusive K^+ ions may enhance the ionic transmembrane current. Therefore, regardless of the direction of the ionic concentration gradient on the forward or on the reverse, diffusive ion flow has the same ability for promoting ionic transportation properties. Ionic selective transport of the hour-glass shaped alumina nanochannels also has been constructed, which is opposite to some reported artificial nanochannels [13, 32] that asymmetric geometry is needed. Based on the regulation of both pH and concentration gradients, we implement the heterogeneous surface charges distribution and execute the asymmetric external stimuli in one integrating device successfully.

The concentration-gradient dependent ionic rectification ratios are summarized in Figure 8. Without concentration gradient, the rectification ratio of hour-glass shaped alumina nanochannels recorded at $\pm 2 \text{ V}$ is 10.2 under the asymmetric acid-base solution with the concentration of about 0.1 mM. When the forward concentration gradient is applied ($C_L < C_R$), the enhanced rectification ratio with a factor of 14.6 is obtained in an ionic concentration gradient of 0.1 mM/1 mM (red histogram). In this way, the diffusive ion flow remarkably promotes the ionic transport at “on” state as the synergistic effect of diffusive ion flow and voltage driven ion flow. Then, with the concentration gradient increasing to 100-fold and 1000-fold, the rectification ratios decreased to 9.9 and 5.7 due to the decrease in electrical double layer thickness in high concentrated solutions, which is not beneficial for ionic accumulated on the inner walls by the electrostatic interaction. When the reversed concentration gradient is applied ($C_L > C_R$), the optimal rectification characteristic is also obtained at 10-fold concentration gradient (grey histogram). It is affirmative that ionic rectification behavior could be enhanced under regulating of both pH and concentration gradients for such symmetric artificial nanochannels.

4. Conclusion

In summary, we fabricated a new alumina membrane with symmetric hour-glass shaped nanochannels for the first time via the double-side anodization method and an in situ pore opening procedure, which displays both pH- and concentration-modulated asymmetric ionic transport

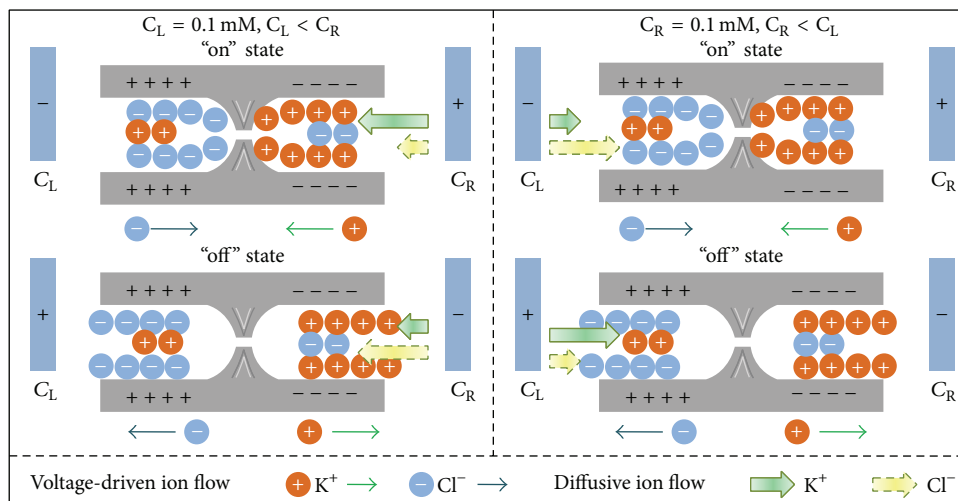


FIGURE 7: Schematic representation of how the alumina nanochannel operates under both pH and concentration gradient at "on" state and "off" state. When $C_L < C_R$, the direction of diffusive K^+ ion flow and voltage-induced K^+ ion flow is accordant to make large current at "on" state (up-left). While at "off" state, few Cl^- ions are replenished into the ion-depleted zone at base side and get across the membrane under the concentration gradient stimuli (bottom-left). When $C_L > C_R$, the diffusive ion flow at the acid side exhibited the same ability for promoting ionic transportation properties (right) as that at the base side. Ionic selective transport also has been constructed dependent on the cooperative effect of pH and concentration gradient. The value of pH_L is 5.2 and that of pH_R is 10.0.

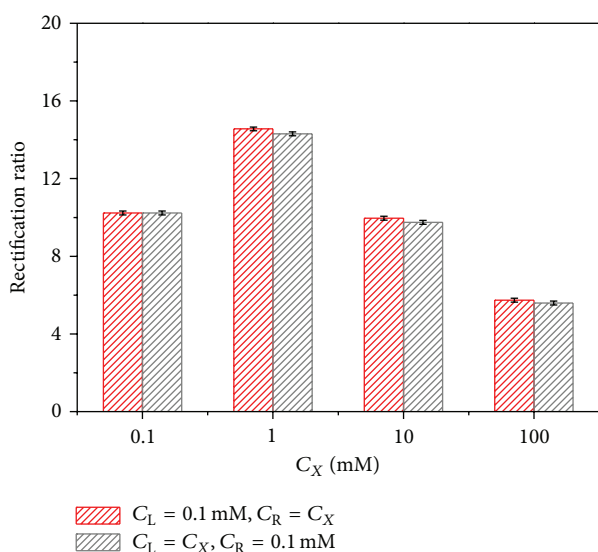


FIGURE 8: Ionic current rectification ratios of the hour-glass shaped alumina nanochannel with or without ionic concentration gradient. When C_L is 0.1 mM, the enhanced rectification ratio with a maximum factor of 14.6 was obtained in a 10-fold concentration gradient solution (red histogram). With this forward concentration gradient increasing to 100-fold and 1000-fold, the rectification ratios decreased. When using the reversed concentration gradient stimuli (grey histogram), we got the similar rectification ratio results. The value of pH_L is 5.2 and that of pH_R is 10.0.

properties. Under different pH gradient stimuli, the as-prepared alumina nanochannels presented regular changes in rectified ionic current on account of different surface charge density and polarity distributions on the inner walls of the

nanochannels. When the pH gradient was defined, enhanced ionic current rectification properties were revealed due to the synergistic effect of the voltage driven ion flow and diffusion driven ion flow under low electrolyte concentration gradient. We believe that the hour-glass shaped alumina nanochannels may inspire innovation in the application of the complex ionic current rectification devices in contrast to previously reported nanochannels to provide molecular analysis, controlled mass transport, and photoelectric conversion systems.

Conflict of Interests

The authors declare that there is no conflict of interests regarding the publication of this paper.

Authors' Contribution

Shengnan Hou and Qinqin Wang contributed equally to this work.

Acknowledgments

The authors thank the National Natural Science Foundation of China (Grant no. 21101009) and the National Basic Research Program of China (973 Program, Grant no. 2010CB934700). The work was also supported by the Fundamental Research Funds for the Central Universities (Grant no. YWF-14-HHXY-12).

References

- [1] C. Spetea and B. Schoefs, "Solute transporters in plant thylakoid membranes key players during photosynthesis and light stress,"

- Communicative & Integrative Biology*, vol. 3, no. 2, pp. 122–129, 2010.
- [2] D. Gust, T. Moore, and A. L. Moore, “Mimicking photosynthetic solar energy transduction,” *Accounts of Chemical Research*, vol. 34, no. 1, pp. 40–48, 2001.
- [3] E. Gouaux and R. MacKinnon, “Principles of selective ion transport in channels and pumps,” *Science*, vol. 310, no. 5753, pp. 1461–1465, 2005.
- [4] H. Dong, R. Nie, X. Hou, P. Wang, J. Yue, and L. Jiang, “Assembly of FOF1-ATPase into solid state nanoporous membrane,” *Chemical Communications*, vol. 47, no. 11, pp. 3102–3104, 2011.
- [5] H. Zhang, X. Hou, L. Zeng et al., “Bioinspired artificial single ion pump,” *Journal of the American Chemical Society*, vol. 135, no. 43, pp. 16102–16110, 2013.
- [6] A. Alcaraz, P. Ramírez, E. García-Giménez, M. L. López, A. Andrio, and V. M. Aguilera, “A pH-tunable nanofluidic diode: electrochemical rectification in a reconstituted single ion channel,” *The Journal of Physical Chemistry B*, vol. 110, no. 42, pp. 21205–21209, 2006.
- [7] Z. S. Siwy, I. Kosińska, A. Fuliński, and C. Martin, “Asymmetric diffusion through synthetic nanopores,” *Physical Review Letters*, vol. 94, no. 4, Article ID 048102, 2005.
- [8] M. Ali, P. Ramirez, Q. H. Nguyen et al., “Single cigar-shaped nanopores functionalized with amphoteric amino acid chains: experimental and theoretical characterization,” *ACS Nano*, vol. 6, no. 4, pp. 3631–3640, 2012.
- [9] Y. He, D. Gillespie, D. Boda, I. Vlassiuk, R. S. Eisenberg, and Z. S. Siwy, “Tuning transport properties of nanofluidic devices with local charge inversion,” *Journal of the American Chemical Society*, vol. 131, no. 14, pp. 5194–5202, 2009.
- [10] L. H. Yeh, M. Zhang, and S. Qian, “Ion transport in a pH-regulated nanopore,” *Analytical Chemistry*, vol. 85, no. 15, pp. 7527–7534, 2013.
- [11] P. Ramirez, M. Ali, W. Ensinger, and S. Mafe, “Information processing with a single multifunctional nanofluidic diode,” *Applied Physics Letters*, vol. 101, no. 13, Article ID 133108, 2012.
- [12] J. Kim, S. J. Kim, and D. K. Kim, “Energy harvesting from salinity gradient by reverse electrodialysis with anodic alumina nanopores,” *Energy*, vol. 51, pp. 413–421, 2013.
- [13] I. Vlassiuk and Z. S. Siwy, “Nanofluidic diode,” *Nano Letters*, vol. 7, no. 3, pp. 552–556, 2007.
- [14] Z. Y. Meng, H. Bao, J. T. Wang et al., “Artificial ion channels regulating light-induced ionic currents in photoelectrical conversion systems,” *Advanced Materials*, vol. 26, no. 15, pp. 2329–2334, 2014.
- [15] L. P. Wen, X. Hou, Y. Tian, J. Zhai, and L. Jiang, “Bio-inspired photoelectric conversion based on smart-gating nanochannels,” *Advanced Functional Materials*, vol. 20, no. 16, pp. 2636–2642, 2010.
- [16] L. P. Wen, Y. Tian, Y. Guo, J. Ma, W. Liu, and L. Jiang, “Conversion of light to electricity by photoinduced reversible pH changes and biomimetic nanofluidic channels,” *Advanced Functional Materials*, vol. 23, no. 22, pp. 2887–2893, 2013.
- [17] W. Guo, L. C. Cao, J. Xia et al., “Energy harvesting with single-ion-selective nanopores: a concentration-gradient-driven nanofluidic power source,” *Advanced Functional Materials*, vol. 20, no. 8, pp. 1339–1344, 2010.
- [18] E. García-Giménez, A. Alcaraz, V. M. Aguilera, and P. Ramírez, “Directional ion selectivity in a biological nanopore with bipolar structure,” *Journal of Membrane Science*, vol. 331, no. 1–2, pp. 137–142, 2009.
- [19] Z. S. Siwy, “Ion-current rectification in nanopores and nanotubes with broken symmetry,” *Advanced Functional Materials*, vol. 16, no. 6, pp. 735–746, 2006.
- [20] L. Wang, W. Guo, Y. B. Xie, X. W. Wang, J. M. Xue, and Y. G. Wang, “Nanofluidic diode generated by pH gradient inside track-etched conical nanopore,” *Radiation Measurements*, vol. 44, no. 9–10, pp. 1119–1122, 2009.
- [21] L. Cao, W. Guo, Y. Wang, and L. Jiang, “Concentration-gradient-dependent ion current rectification in charged conical nanopores,” *Langmuir*, vol. 28, no. 4, pp. 2194–2199, 2012.
- [22] L. H. Yeh, C. Hughes, Z. Zeng, and S. Qian, “Tuning ion transport and selectivity by a salt gradient in a charged nanopore,” *Analytical Chemistry*, vol. 86, no. 5, pp. 2681–2686, 2014.
- [23] L. J. Cheng and L. J. Guo, “Rectified ion transport through concentration gradient in homogeneous silica nanochannels,” *Nano Letters*, vol. 7, no. 10, pp. 3165–3171, 2007.
- [24] W. L. Hsu, D. W. Inglis, H. Jeong et al., “Stationary chemical gradients for concentration gradient-based separation and focusing in nanofluidic channels,” *Langmuir*, vol. 30, no. 18, pp. 5337–5348, 2014.
- [25] I. Vlassiuk, T. R. Kozel, and Z. S. Siwy, “Biosensing with nanofluidic diodes,” *Journal of the American Chemical Society*, vol. 131, no. 23, pp. 8211–8220, 2009.
- [26] A. M. Md Jani, D. Losic, and N. H. Voelcker, “Nanoporous anodic aluminium oxide: advances in surface engineering and emerging applications,” *Progress in Materials Science*, vol. 58, no. 5, pp. 636–704, 2013.
- [27] Y. Zhou, W. Guo, J. Cheng, Y. Liu, J. Li, and L. Jiang, “High-temperature gating of solid-state nanopores with thermoresponsive macromolecular nanoactuators in ionic liquids,” *Advanced Materials*, vol. 24, no. 7, pp. 962–967, 2012.
- [28] Y. N. Jiang, N. Liu, W. Guo, F. Xia, and L. Jiang, “Highly-efficient gating of solid-state nanochannels by DNA sandwich structure containing ATP aptamers: a nanofluidic IMPLICATION logic device,” *Journal of the American Chemical Society*, vol. 134, no. 37, pp. 15395–15401, 2012.
- [29] R. X. Yan, W. J. Liang, R. Fan, and P. D. Yang, “Nanofluidic diodes based on nanotube heterojunctions,” *Nano Letters*, vol. 9, no. 11, pp. 3820–3825, 2009.
- [30] S. M. Wu, F. Wildhaber, O. Vazquez-Mena, A. Bertsch, J. Brugger, and P. Renaud, “Facile fabrication of nanofluidic diode membranes using anodic aluminium oxide,” *Nanoscale*, vol. 4, no. 18, pp. 5718–5723, 2012.
- [31] L. J. Cheng and L. J. Guo, “Ionic current rectification, breakdown, and switching in heterogeneous oxide nanofluidic devices,” *ACS Nano*, vol. 3, no. 3, pp. 575–584, 2009.
- [32] Y. Kong, X. Fan, M. H. Zhang et al., “Nanofluidic diode based on branched alumina nanochannels with tunable ionic rectification,” *ACS Applied Materials & Interfaces*, vol. 5, no. 16, pp. 7931–7936, 2013.
- [33] C. Y. Li, F. X. Ma, Z. Q. Wu et al., “Solution-pH-modulated rectification of ionic current in highly ordered nanochannel arrays patterned with chemical functional groups at designed positions,” *Advanced Functional Materials*, vol. 23, no. 31, pp. 3836–3844, 2013.
- [34] E. B. Kalman, I. Vlassiuk, and Z. S. Siwy, “Nanofluidic bipolar transistors,” *Advanced Materials*, vol. 20, no. 2, pp. 293–297, 2008.
- [35] X. Hou, F. Yang, L. Li, Y. Song, L. Jiang, and D. Zhu, “A biomimetic asymmetric responsive single nanochannel,” *Journal of the American Chemical Society*, vol. 132, no. 33, pp. 11736–11742, 2010.

- [36] H. Han, S. J. Park, J. S. Jang et al., "In situ determination of the pore opening point during wet-chemical etching of the barrier layer of porous anodic aluminum oxide: nonuniform impurity distribution in anodic oxide," *ACS Applied Materials and Interfaces*, vol. 5, no. 8, pp. 3441–3448, 2013.
- [37] J. Cui, Y. Wu, Y. Wang, H. Zheng, G. Xu, and X. Zhang, "A facile and efficient approach for pore-opening detection of anodic aluminum oxide membranes," *Applied Surface Science*, vol. 258, no. 14, pp. 5305–5311, 2012.
- [38] C. Y. Han, G. A. Willing, Z. L. Xiao, and H. H. Wang, "Control of the anodic aluminum oxide barrier layer opening process by wet chemical etching," *Langmuir*, vol. 23, no. 3, pp. 1564–1568, 2007.
- [39] C. Cheng and A. H. W. Ngan, "Growth sustainability of nanopore channels in anodic aluminum oxide guided with prepatterns," *The Journal of Physical Chemistry C*, vol. 117, no. 23, pp. 12183–12190, 2013.
- [40] M. Kosmulski, "pH-dependent surface charging and points of zero charge II. Update," *Journal of Colloid and Interface Science*, vol. 275, no. 1, pp. 214–224, 2004.
- [41] R. Karnik, C. H. Duan, K. Castelino, H. Daiguji, and A. Majumdar, "Rectification of ionic current in a nanofluidic diode," *Nano Letters*, vol. 7, no. 3, pp. 547–551, 2007.
- [42] H. Daiguji, Y. Oka, and K. Shirono, "Nanofluidic diode and bipolar transistor," *Nano Letters*, vol. 5, no. 11, pp. 2274–2280, 2005.
- [43] Z. S. Siwy and S. Howorka, "Engineered voltage-responsive nanopores," *Chemical Society Reviews*, vol. 39, no. 3, pp. 1115–1132, 2010.

Research Article

Fabrication of Phase-Change Polymer Colloidal Photonic Crystals

Tianyi Zhao,¹ Youzhuan Zhang,² Jingxia Wang,³ Yanlin Song,² and Lei Jiang²

¹ Key Laboratory of Bio-Inspired Smart Interfacial Science and Technology of Ministry of Education, School of Chemistry and Environment, Beihang University, Beijing 100191, China

² Beijing National Laboratory for Molecular Sciences (BNLMS), Laboratory of New Materials, Key Laboratory of Organic Solids, Institute of Chemistry, Chinese Academy of Sciences, Beijing 100190, China

³ Technical Institute of Physics and Chemistry, Chinese Academy of Sciences, Beijing 100190, China

Correspondence should be addressed to Jingxia Wang; wangzhang@iccas.ac.cn

Received 16 April 2014; Accepted 13 May 2014; Published 12 June 2014

Academic Editor: Yongping Hou

Copyright © 2014 Tianyi Zhao et al. This is an open access article distributed under the Creative Commons Attribution License, which permits unrestricted use, distribution, and reproduction in any medium, provided the original work is properly cited.

This paper presents the preparation of phase-change polymer colloidal photonic crystals (PCs) by assembling hollow latex spheres encapsulated with dodecanol for the first time. The monodispersed hollow latex spheres were obtained by phase reversion of monodispersed core-shell latex spheres in the n-hexane, which dissolves the PS core and retains the PMMA/PAA shell. The as-prepared phase-change colloidal PCs show stable phase-change behavior. This fabrication of phase-change colloidal PCs would be significant for PC's applications in functional coatings and various optic devices.

1. Introduction

Photonic crystals (PCs) have attracted enormous interest due to their unusual optical properties originating from the photonic stopband [1, 2] and show potential applications in smart windows, chemical sensors, and optical devices [3–5]. Recently, increasing interest has been focused on the fabrication of multifunctional PCs; besides their photonic stopband, they can exhibit extra properties and greatly extend their applications [6–12]. For example, tough [13–15] PCs can endure various harsh environments; PCs with special wettability [16–21] favor swift diffusion of the detected materials into the PCs for the highly sensitive sensors, [20] while the responsive PCs [22–25] can respond to various exterior stimuli. Typically, Dorvee et al. [20] reported an amphiphilic, magnetic bifunctional PCs which could manipulate liquid droplets without microfluidic container and its structure color provides an optical signal to distinguish different liquids. It is expected to fabricate novel functional PCs to meet application requirements. Herein, a phase-change polymer colloidal PCs is firstly fabricated by assembly of latex particles encapsulated with phase-change materials (PCMs)

of dodecanol, which will greatly extend the applications of PCs in functional coatings.

PCMs [26–29] have attracted wide attention since PCMs can store and release latent heat during their phase transition at defined temperature range, which can be used in thermal energy conservation [29–31]. In the past several decades, research attentions have been mainly paid on the fabrications of phase-change microcapsules [32, 33] or phase-change fibers [34], which could retain energy and is used in thermal regulated fabrics, coatings, building, and so forth. It is expected that a novel colloidal PCs could be fabricated if introducing PCMs into the interior of the colloidal PCs. Here, we demonstrate the fabrication of phase-change polymer colloidal PCs by assembly of the hollow latex spheres encapsulated of PCM with n-dodecanol for the first time. The hollow latex spheres are prepared by phase reversion of monodispersed latex spheres with PS core and PMMA/PAA shell in the solvent of n-hexane, which is the good solvent of PS core but poor solvent of the PMMA/PAA shell. The as-prepared phase-change colloidal crystals contain 35% dodecanol, showing a stable phase-change behavior. This fabrication of phase-change PCs with

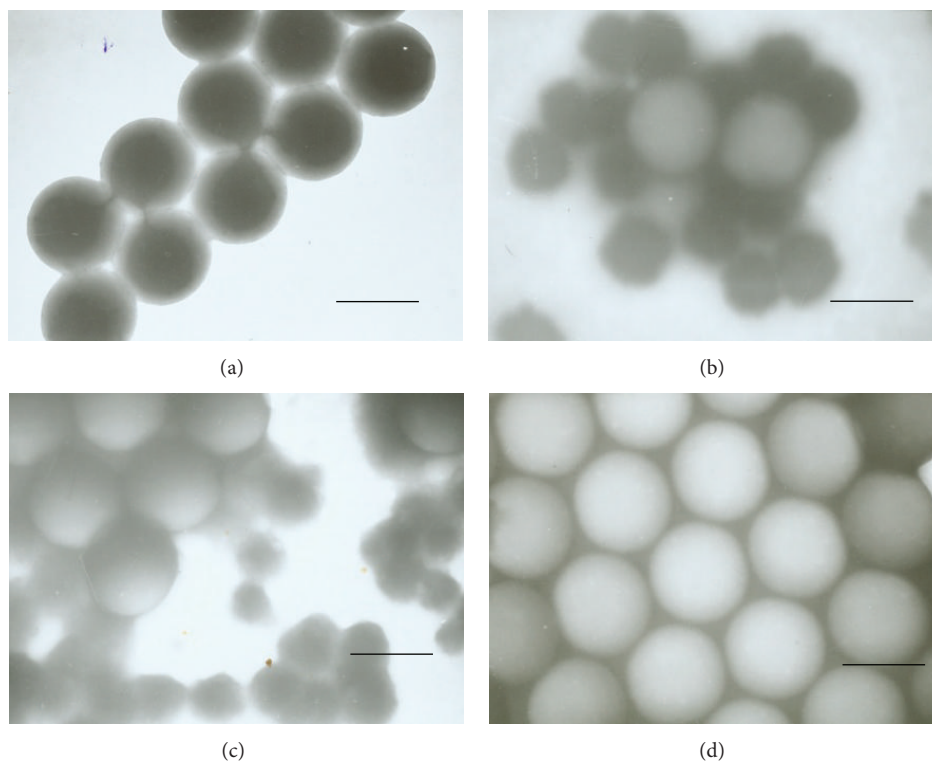


FIGURE 1: Typical TEM images of the latex spheres after dispersing in the n-hexane with different times (a) 0, (b) 5, (c) 10, and (d) 30 min. Scale bar: 200 nm.

energy storage properties greatly enlarges the application of polymer colloidal crystals in functional coatings.

2. Experimental Part

2.1. Preparation of Monodispersed Latex Spheres. Monodispersed core-shell latex spheres of poly(styrene-methyl methacrylate-acrylic acid) (Poly(St-MMA-AA)) with diameter of 230 nm were prepared via soap-free emulsion polymerization as reported modified procedure [15, 35]. The polydispersity of the latex spheres was about 0.005, which was detected by ZetaPALS BI-90plus (Brookhaven instrument). Glass transition temperature (T_g) of the as-prepared sample was 107.6°C; the value was analyzed with a Perkin-Elmer DSC 7 (USA).

2.2. Fabrication of Hollow Monodispersed Latex Spheres. The hollow monodispersed latex spheres were prepared as follows [36–38]: firstly, the as-prepared latex suspension was dispersed into the n-hexane (1 : 10, V/V) by ultrasonic at 30°C for 30 min. Secondly, the aforementioned n-hexane phase was removed and the remaining samples were continuously washed via n-hexane for several times. Thus, the hollow latex spheres samples were obtained.

2.3. Filling the Hollow Latex Spheres via n-Dodecanol. The hollow latex spheres were filled with n-dodecanol by dispersing the hollow latex spheres in the solvent of n-dodecanol

for 30 min at 30°C. Subsequently, the filled latex spheres were redispersed into the aqueous system prepared for the use of the self-assembly.

2.4. Fabrication of Phase-Change Colloidal PCs. The phase-change colloidal PCs were fabricated on glass substrates by vertical deposition method [15, 35]. Glass slides were treated firstly with a chromic-sulfuric acid solution to ensure clean surfaces and then fixed vertically in a vial containing the monodisperse hollow PMMA-PAA aqueous suspension of 0.2 wt% at constant temperature (25°C) and humidity (60 R.H.%) for 24 h. Then, the dried phase-change PCs were obtained.

2.5. Characterization. Transmission electron microscopy (TEM) images of latex spheres were obtained with a H800 transmission microscope (JEM2010, Japan); high resolution TEM (HRTEM) (Tecnai F30) was used to investigate the latex morphology. Scanning electron microscopy (SEM) images were obtained with a field-emission scanning electron microscope (JEOL JSM-6700, Japan). UV-Vis spectra were performed on a U-4100 UV-Vis Spectrometer (Hitachi, Japan). A Nicolet Magna 750 FTIR spectrometer was used to investigate the chemical component of the colloidal crystal films by attenuated total reflectance infrared spectroscopy (ATR-FTIR) mode. The phase-change property of the samples was determined by DSC (Shimadzu DSC-60) in Al pans with a scanning rate of 4°C/min.

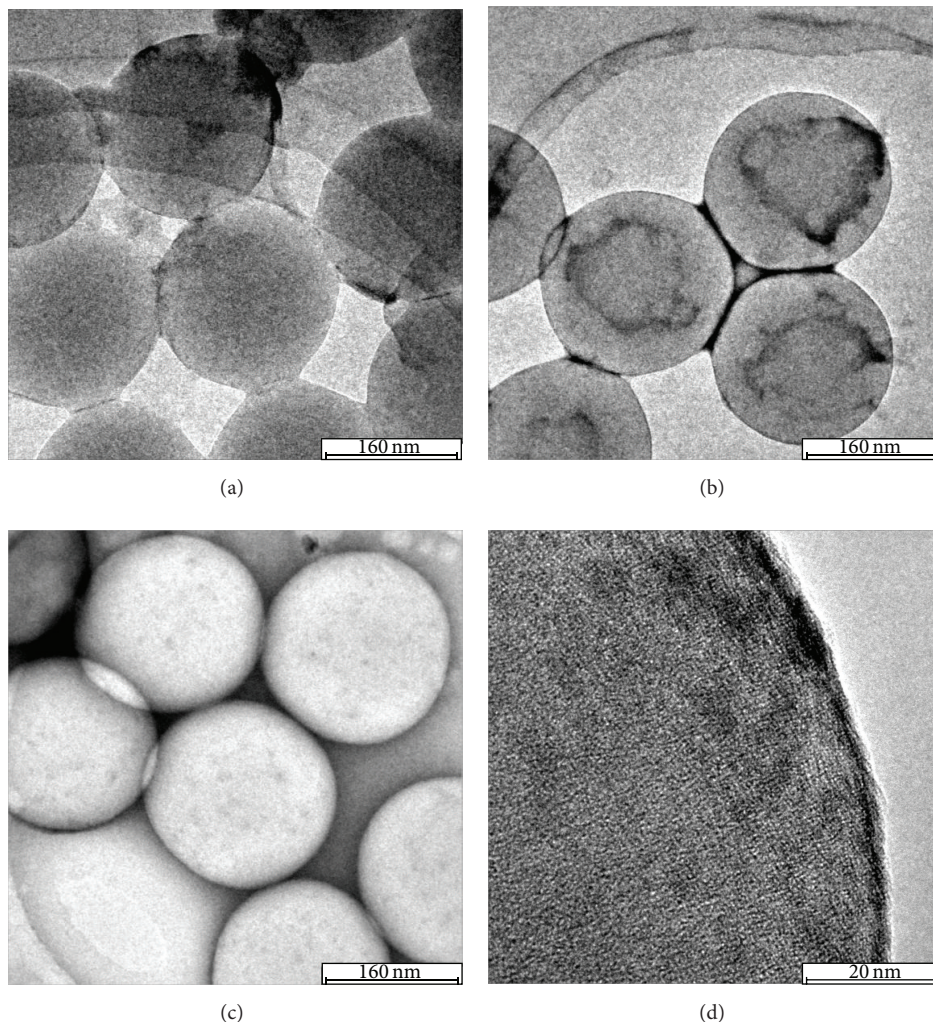


FIGURE 2: HRTEM images of the films. (a) Solid spheres, (b) latex spheres dispersing in n-hexane for 5 min, (c) hollow latex spheres, and (d) high-magnification image of the hollow sphere. Scale bar from (a) to (c) is 160 nm and scale bar of (d) is 20 nm.

3. Results and Discussion

The monodispersed latex spheres with hydrophobic PS core and hydrophilic PMMA/PAA shell were prepared via one-step soap-free emulsion polymerization, [15, 35, 39] where hydrophilic AA and hydrophobic St were dispersed in the aqueous phase and the spontaneous formation of hydrophilic shell and hydrophobic core was mainly attributed to the minimization of the total interfacial energy in the aqueous phase [39]. Thus, hydrophobic polymer segment (PS-rich) would try to depart from water phase, while the hydrophilic polymer segment (PMMA/PAA-rich) would prefer to extend toward the water phase. As a consequence, the latex spheres with PS-rich core and PMMA/PAA-rich shell were formed. The core-shell morphology can be clearly confirmed from TEM images of Figure 1(a), where, the darkly PS-rich regions are surrounded by the grey PAA/PMMA-rich domains.

The hollow latex spheres are prepared by dispersing the as-prepared latex suspension with PS core-PMMA/PAA shell into the solvent of n-hexane, which is a good solvent of PS

core but poor solvent of PMMA/PAA shell. Figures 1(a)–1(d) present TEM images of the latex suspension with PS core-PMMA/PAA shell after being dispersed in n-hexane for different times. Clearly, the core part of latex spheres gradually decreases and disappears when dispersing the latex spheres in the n-hexane for 5, 10, and 30 min, which indicates that the hollow latex sphere can be obtained via the above-mentioned process. In details, the black hydrophobic PS core will effuse and melt into the n-hexane phase once the latex spheres are dispersed into the n-hexane in Figure 1(b), which is very different from that before the sample is dispersed into the n-hexane; latex particles keep distinct black hydrophobic core and grey hydrophilic shell in Figure 1(a). The irregular black particle in Figures 1(b) and 1(c) is the melted PS core since the black hydrophobic PS-rich core tends to extend toward the hydrophobic n-hexane solvent phase due to their similar solubility and phase separation [36–38]. With the increased ultrasonic time, most of PS-rich segment in the core dissolves into the n-hexane. As a result, the insoluble PMMA/PAA-rich segment is retained and the latex sphere

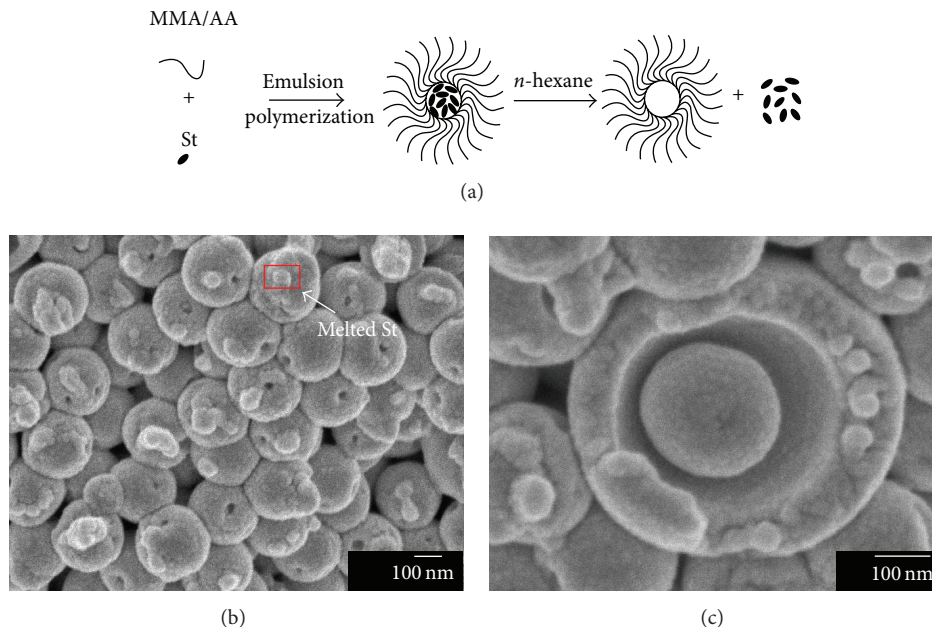


FIGURE 3: (a) Schematic illustration of the formation process from solid sphere to hollow sphere. (b) and (c) SEM images of the films assembled from latex spheres dispersing in n-hexane for 5 min.

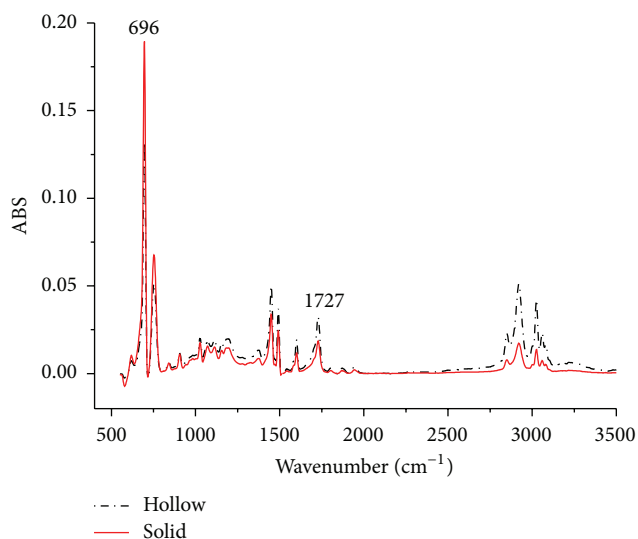


FIGURE 4: ATR FTIR spectra of solid sphere (red solid line) and hollow sphere (black dot line).

keeps the spherical shape, which results in the formation of hollow latex spheres made of PMMA/PAA in Figures 1(c) and 1(d). But the broken latex spheres would be observed if ultrasonic time is over 30 min. High magnification HRTEM images in Figure 2 confirm the elimination of the PS core and the achievement of the hollow P(MMA-AA) latex spheres. However, no clear cavity could be observed in the shell of hollow latex sphere, as given in the magnified HRTEM image in Figure 2(d). But an obvious cavity could be found in the latex particle from the SEM pictures, which confirms the obtainment of the latex particle with hollow structure

when further putting the hollow latex particles in the liquid N₂ for 5 min (see Figure S1, see supplementary material available online at <http://dx.doi.org/10.1155/2014/702089>).

Furthermore, the influence of the mixing ratio of n-hexane and polymer on the resultant morphology of latex spheres has been optimized (see Table S1). When the volume ratio of the latex and n-hexane is smaller than 1:1, the dissolution effect is insufficient for the removal of PS core. But the PS residue is found when the ratio of n-hexane is smaller than 10 and the broken latex spheres will be observed when the solvent ratio is larger than 10. It is found that the optimized volume ratio of the latex and n-hexane is 1:10. The possible formation procedure of the hollow latex spheres was also presented in the upper part of Figure 3 (Figure 3(a)). The initial core-shell latex spheres with PS-rich core and PMMA/PAA-rich shell are firstly synthesized by one-step emulsion polymerization. When the as-prepared latex spheres are dispersed into the solvent of n-hexane, phase reversion occurs to the polymer segments with different polarity. As a result, the PS-rich polymer segment in the latex core would be dissolved out while the PMMA/PAA-rich polymer shell would keep intact. The procedure can be further elaborated by the SEM images of the film assembled from latex spheres which were just undergone the process of dispersing into the solvent. From Figure 3(b), it can be clearly observed that PS residue formed irregular particles onto the PMMA/PAA polymer shells when dispersing into the n-hexane solvent. From the magnified image in Figure 3(c), it can also be observed that core part of the latex sphere was reduced because of the dispersing process.

To confirm clearly the dissolution or part dissolution of PS-rich core in n-hexane solvent, ATR [19, 40] spectra is used to check the change of the chemical composition of the films

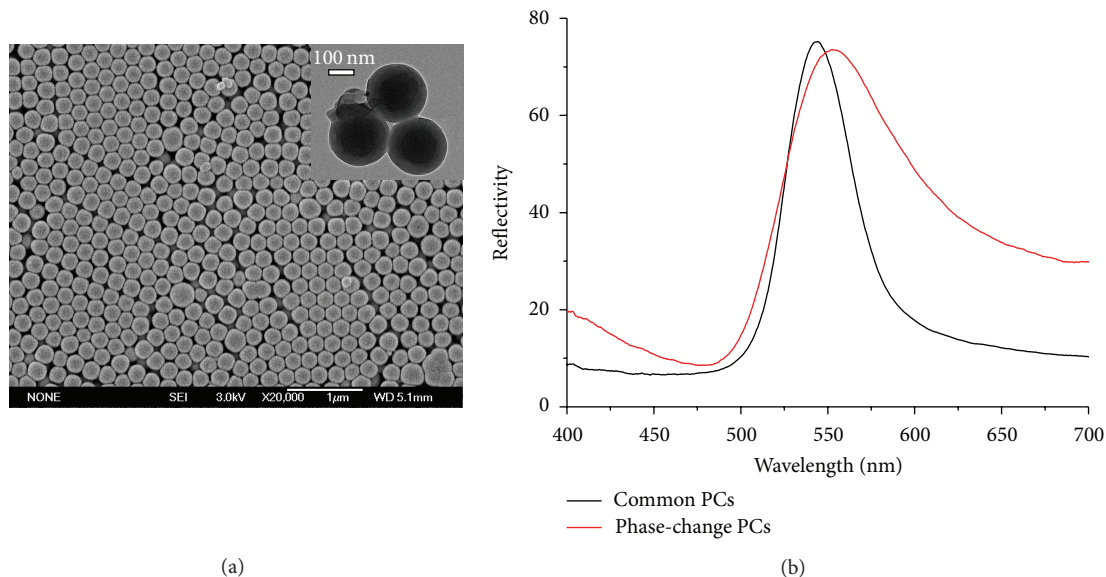


FIGURE 5: (a) SEM images and (b) UV-Vis spectra of the as-prepared phase-change and common PCs; the insert is the TEM image of the latex particle encapsulated with n-dodecanol.

assembled from latex spheres before and after being dispersed in the solvent. The result is demonstrated in Figure 4. In this experiment, the change of chemical component of the colloidal crystal films is estimated from the different absorbance of specific infrared bands, in particular, the change of absorbance ratios between PS and PMMA/PAA. In this case, the characteristic absorbance bands of 1727 cm^{-1} from carboxyl group, and 696 cm^{-1} from benzene group, represent the chemical composition of core (PS) and shell (PMMA/PAA) part [19]. As an example, Figure 4 presents the ATR spectra of the colloidal crystal films assembled from hollow or solid latex spheres, respectively. And the absorbance ratio between the absorbance bands 696 and 1727 cm^{-1} is 9.88 before the latex spheres are dispersed into the solvent and the value lowers and reaches 3.93 after dispersing into the solution. The result indicates the decrease of the ratio of PS segment after dispersing the latex spheres in the solution; the characterization result is well agreed with the phase reversion or disappearance of the PS-rich core part in Figure 1.

The phase-change colloidal PCs were obtained by assembly of hollow latex spheres filled with n-dodecanol. The insert picture of Figure 5(a) is TEM image of the latex particle infiltrated in n-dodecanol, the clear flow of the dodecanol could be found in magnified image in Figure S2. Figure 5 shows the SEM image and the UV-vis spectra of the as-prepared phase-change colloidal PCs. Clearly, there is well-ordered arrangement for the latex spheres in the films in Figure 5(a), which contributes to the good optic properties in Figure 5(b). But the reflection spectra of phase-change colloidal PCs is broader than that of PCs from common latex particles, which indicates that the dissolution process of core may result in some deformation of latex spheres. This affects the assembly and optic properties of the resultant film.

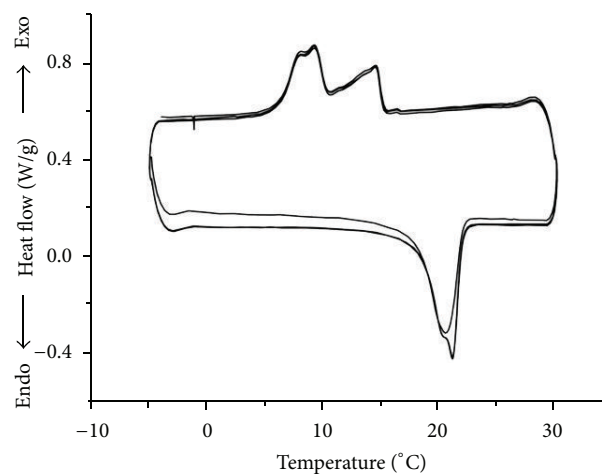


FIGURE 6: DSC measurement of the as-prepared phase-change polymer colloidal PCs. The phase-change material is n-dodecanol.

Phase-change properties of the resultant colloidal PCs could be clearly seen from DSC measurement in Lissajous figures of Figure 6. Because the melting point of the n-dodecanol is about 24°C , we characterize the thermal properties of as-prepared phase-change colloidal PCs ranging from 0 to 30°C with a heating/cooling rate of $4^\circ\text{C}/\text{min}$ for three cycles. The as-prepared colloidal PCs have two obvious absorb and release processes which correspond to the melting point and freezing point of the n-dodecanol, respectively. Among these peaks, the melting point (21.23°C) and the freezing point (8 and 14°C) indicate the existence of the n-dodecanol in the as-prepared colloidal PCs. It should be noted that two exothermic peaks occur during the cooling process, which may be attributed to the influence of the latex

polymer on bulk crystallization, which leads to the lower enthalpy than that of melt peak. The measured enthalpy of melting of the sample was about 14.01 J/g; it could be calculated that about 35% n-dodecanol is encapsulated into the latex particle. More importantly, the good repeatability of cycle measurement indicates that the PCMs have been encapsulated independently in the latex spheres without leakage.

4. Conclusion

The paper demonstrated a facile fabrication of hollow latex spheres from phase separation of core-shell latex spheres and the hollow latex spheres were encapsulated with n-dodecanol. The phase-change polymer colloidal crystals assembled from latex spheres filled with n-dodecanol showed stable phase-change behavior. The fabrication of phase-change colloidal PCs is significant for the promising application in functional coatings.

Conflict of Interests

The authors declare that there is no conflict of interests regarding the publication of this paper.

Acknowledgments

This work is supported by National Natural Science Foundation of China (nos. 21101010, 91127029, 51373183, and 21074139) and 973 Program (nos. 2011CB932303 and 2011CB8084004).

References

- [1] Y. Huang, J. Zhou, B. Su et al., "Colloidal photonic crystals with narrow stopbands assembled from low-adhesive superhydrophobic substrates," *Journal of the American Chemical Society*, vol. 134, no. 41, pp. 17053–17058, 2012.
- [2] R. Wagner and F. Cichos, "Fast measurement of photonic stop bands by back focal plane imaging," *Physical Review B: Condensed Matter and Materials Physics*, vol. 87, no. 16, Article ID 165438, 2013.
- [3] X. Huang, Y. Lai, Z. H. Hang, H. Zheng, and C. T. Chan, "Dirac cones induced by accidental degeneracy in photonic crystals and zero-refractive-index materials," *Nature Materials*, vol. 10, no. 8, pp. 582–586, 2011.
- [4] A. Mihi, C. Zhang, and P. V. Braun, "Transfer of preformed three-dimensional photonic crystals onto dye, sensitized solar cells," *Angewandte Chemie*, vol. 123, pp. 5830–5833, 2011.
- [5] C. I. Aguirre, E. Reguera, and A. Stein, "Tunable colors in opals and inverse opal photonic crystals," *Advanced Functional Materials*, vol. 20, no. 16, pp. 2565–2578, 2010.
- [6] C. Zhu, L. Chen, H. Xu, and Z. Gu, "A magnetically tunable colloidal crystal film for reflective display," *Macromolecular Rapid Communications*, vol. 30, no. 22, pp. 1945–1949, 2009.
- [7] H. Wang, Q.-W. Chen, Y.-F. Yu, K. Cheng, and Y.-B. Sun, "Size- and solvent-dependent magnetically responsive optical diffraction of carbon-encapsulated superparamagnetic colloidal photonic crystals," *Journal of Physical Chemistry C*, vol. 115, no. 23, pp. 11427–11434, 2011.
- [8] A. Ghadimi, L. Cademartiri, U. Kamp, and G. A. Ozin, "Plasma within templates: molding flexible nanocrystal solids into multifunctional architectures," *Nano Letters*, vol. 7, no. 12, pp. 3864–3868, 2007.
- [9] M. E. Calvo, S. Colodrero, N. Hidalgo et al., "Porous one dimensional photonic crystals: novel multifunctional materials for environmental and energy applications," *Energy and Environmental Science*, vol. 4, no. 12, pp. 4800–4812, 2011.
- [10] C.-Y. Liu and L.-W. Chen, "Tunable channel drop filter in a two-dimensional photonic crystal modulated by a nematic liquid crystal," *Journal of Nanomaterials*, vol. 2006, Article ID 52946, 6 pages, 2006.
- [11] J. Riedrich-Möller, L. Kipfstuhl, C. Hepp et al., "One- and two-dimensional photonic crystal microcavities in single crystal diamond," *Nature Nanotechnology*, vol. 7, no. 1, pp. 69–74, 2012.
- [12] P. Alivisatos, "The use of nanocrystals in biological detection," *Nature Biotechnology*, vol. 22, no. 1, pp. 47–52, 2004.
- [13] B. You, N. Wen, L. Shi, L. Wu, and J. Zi, "Facile fabrication of a three-dimensional colloidal crystal film with large-area and robust mechanical properties," *Journal of Materials Chemistry*, vol. 19, no. 22, pp. 3594–3597, 2009.
- [14] J. Zhou, H. Li, L. Ye et al., "Facile fabrication of tough SiC inverse opal photonic crystals," *Journal of Physical Chemistry C*, vol. 114, no. 50, pp. 22303–22308, 2010.
- [15] J. Wang, Y. Wen, H. Ge et al., "Simple fabrication of full color colloidal crystal films with tough mechanical strength," *Macromolecular Chemistry and Physics*, vol. 207, no. 6, pp. 596–604, 2006.
- [16] J. Wang, Y. Zhang, S. Wang, Y. Song, and L. Jiang, "Bioinspired colloidal photonic crystals with controllable wettability," *Accounts of Chemical Research*, vol. 44, no. 6, pp. 405–415, 2011.
- [17] L. Cui, Y. Li, J. Wang et al., "Fabrication of large-area patterned photonic crystals by ink-jet printing," *Journal of Materials Chemistry*, vol. 19, no. 31, pp. 5499–5502, 2009.
- [18] O. Sato, S. Kubo, and G. U. Zhong-Ze, "Structural color films with lotus effects, superhydrophilicity, and tunable stop-bands," *Accounts of Chemical Research*, vol. 42, no. 1, pp. 1–10, 2009.
- [19] J. Wang, Y. Wen, J. Hu, Y. Song, and L. Jiang, "Fine control of the wettability transition temperature of colloidal-crystal films: from superhydrophilic to superhydrophobic," *Advanced Functional Materials*, vol. 17, no. 2, pp. 219–225, 2007.
- [20] J. R. Dorvee, A. M. Derfus, S. N. Bhatia, and M. J. Sailor, "Manipulation of liquid droplets using amphiphilic, magnetic one-dimensional photonic crystal chaperones," *Nature Materials*, vol. 3, no. 12, pp. 896–899, 2004.
- [21] M. Kuang, J. Wang, B. Bao et al., "Inkjet printing patterned photonic crystal domes for wide viewing, angle displays by controlling the sliding three phase contact line," *Advanced Optical Materials*, vol. 2, no. 1, pp. 34–38, 2014.
- [22] G. Jianping, H. Le, J. Goebl, and Y. Yin, "Assembly of magnetically tunable photonic crystals in nonpolar solvents," *Journal of the American Chemical Society*, vol. 131, no. 10, pp. 3484–3486, 2009.
- [23] X. Xu, S. A. Majetich, and S. A. Asher, "Mesoscopic monodisperse ferromagnetic colloids enable magnetically controlled photonic crystals," *Journal of the American Chemical Society*, vol. 124, no. 46, pp. 13864–13868, 2002.
- [24] J. Ge and Y. Yin, "Responsive photonic crystals," *Angewandte Chemie*, vol. 50, no. 7, pp. 1492–1522, 2011.
- [25] H. Wang, Y.-B. Sun, Q.-W. Chen, Y.-F. Yu, and K. Cheng, "Synthesis of carbon-encapsulated superparamagnetic colloidal

- nanoparticles with magnetic-responsive photonic crystal property,” *Dalton Transactions*, vol. 39, no. 40, pp. 9565–9569, 2010.
- [26] S. Raoux and M. Wuttig, *Phase Change Materials*, Springer, 2009.
- [27] M. Wuttig and N. Yamada, “Phase-change materials for rewritable data storage,” *Nature Materials*, vol. 6, no. 11, pp. 824–832, 2007.
- [28] M. Wuttig, “Phase-change materials: towards a universal memory?” *Nature Materials*, vol. 4, no. 4, pp. 265–266, 2005.
- [29] A. Sharma, V. V. Tyagi, C. R. Chen, and D. Buddhi, “Review on thermal energy storage with phase change materials and applications,” *Renewable and Sustainable Energy Reviews*, vol. 13, no. 2, pp. 318–345, 2009.
- [30] L. F. Cabeza, A. Castell, C. Barreneche, A. De Gracia, and A. I. Fernández, “Materials used as PCM in thermal energy storage in buildings: a review,” *Renewable and Sustainable Energy Reviews*, vol. 15, no. 3, pp. 1675–1695, 2011.
- [31] D. Zhou, C. Y. Zhao, and Y. Tian, “Review on thermal energy storage with phase change materials (PCMs) in building applications,” *Applied Energy*, vol. 92, pp. 593–605, 2012.
- [32] L. Bayés-García, L. Ventolà, R. Cordobilla, R. Benages, T. Calvet, and M. A. Cuevas-Diarte, “Phase Change Materials (PCM) microcapsules with different shell compositions: preparation, characterization and thermal stability,” *Solar Energy Materials and Solar Cells*, vol. 94, no. 7, pp. 1235–1240, 2010.
- [33] C. Y. Zhao and G. H. Zhang, “Review on microencapsulated phase change materials (MEPCMs): fabrication, characterization and applications,” *Renewable and Sustainable Energy Reviews*, vol. 15, no. 8, pp. 3813–3832, 2011.
- [34] S.-H. Lee, Y. Jung, and R. Agarwal, “Highly scalable non-volatile and ultra-low-power phase-change nanowire memory,” *Nature Nanotechnology*, vol. 2, no. 10, pp. 626–630, 2007.
- [35] J. Wang, Y. Wen, X. Feng, Y. Song, and L. Jiang, “Control over the wettability of colloidal crystal films by assembly temperature,” *Macromolecular Rapid Communications*, vol. 27, no. 3, pp. 188–192, 2006.
- [36] J. Wang and M. Jiang, “Polymeric self-assembly into micelles and hollow spheres with multiscale cavities driven by inclusion complexation,” *Journal of the American Chemical Society*, vol. 128, no. 11, pp. 3703–3708, 2006.
- [37] Q. Zhang, E. E. Remsen, and K. L. Wooley, “Shell cross-linked nanoparticles containing hydrolytically degradable, crystalline core domains,” *Journal of the American Chemical Society*, vol. 122, no. 15, pp. 3642–3651, 2000.
- [38] J. Fu, J. Wang, Q. Li, D. H. Kim, and W. Knoll, “3D hierarchically ordered composite block copolymer hollow sphere arrays by solution wetting,” *Langmuir*, vol. 26, no. 14, pp. 12336–12341, 2010.
- [39] F. Hoshino, H. Kawaguchi, and Y. Ohtsuka, “N-Substituted acrylamide-styrene copolymer latices. III: morphology of latex particles,” *Polymer Journal*, vol. 19, no. 10, pp. 1157–1164, 1987.
- [40] Y. Liang and H. S. Lee, “Surface-induced crystal orientation of poly(trimethylene 2,6-naphthalate) films studied by polarized FTIR-ATR and grazing incidence X-ray diffraction,” *Macromolecules*, vol. 38, no. 23, pp. 9885–9888, 2005.

Research Article

The Effect of Silver Nanofibers on the Deformation Properties of Blood Vessels: Towards the Development of New Nanotechnologies to Prevent Rupture of Aneurysms

Miguel Gonzalez,¹ Daniel Rivera,¹ Alam Marcelino,¹
Gabriela Agront,¹ Rafael Rodriguez,² and Miguel Castro¹

¹ Department of Chemistry, Chemical Imaging Center, The University of Puerto Rico at Mayaguez, Mayaguez, PR 00682, USA

² University of Puerto Rico, Medical Sciences Campus, San Juan, PR 00936, USA

Correspondence should be addressed to Miguel Castro; miguel.castro2@upr.edu

Received 30 October 2013; Revised 10 January 2014; Accepted 9 February 2014; Published 15 May 2014

Academic Editor: Jingxia Wang

Copyright © 2014 Miguel Gonzalez et al. This is an open access article distributed under the Creative Commons Attribution License, which permits unrestricted use, distribution, and reproduction in any medium, provided the original work is properly cited.

An aneurysm is the result of a widening or ballooning of a portion of a blood vessel. The rupture of an aneurysm occurs when the mechanical stress acting on the inner wall exceeds the failure strength of the blood vessel. We propose an innovative approach to prevent the rupture of an aneurysm based on the use of nanotechnology to improve the strength of the blood vessel. We present results on the effect of silver nanofibers on the resistance toward deformation of blood vessels. The silver nanofibers are grown on the surface of the blood vessels. The nanofibers are 120 ± 30 nm in diameter and 2.7 ± 0.8 μ m in length. The deformation per applied force of blood vessels was found to decrease from 0.15 m/N in control blood vessels to 0.003 m/N in blood vessels treated with the nanofibers. This represents an increase in the resistance towards deformation of a factor of 50. The increase in the resistance towards deformation is clinically significant since blood pressure increases by factors slightly larger than one in the human body. Treatment of blood vessels with silver nanofibers is a potential translational clinical tool for preventing rupture of aneurysms in a clinical setting.

1. Background

An aneurysm is a condition identified as an abnormal widening or ballooning formation on segments of blood vessels that can result in adverse health effects in the population [1–5]. A few of direct implications of different types of the disease in humans are highlighted in Table 1. The development of an aneurysm in a blood vessel is summarized on Figure 1. The biomechanical properties of blood vessels are disrupted by the shear stress associated with the hemodynamics in the region of an aneurysm. Loss of the blood vessel characteristic elasticity allows a persistent widening of the area and the formation and growth of the aneurysm [4, 5]. The biomechanical stress exerted by the regional hemodynamic condition allows for a weakening of vessel walls and increases the risk of aneurysm rupture [4, 5]. Open or endovascular surgery is the recommended treatment for aneurysms that reach a critical

size to prevent rupture [2–5]. Open surgery is performed to replace the affected vessel area with a man-made graft [3–6]. Endovascular surgery, on the other hand, is performed with the insertion of a catheter through the vascular system to reach the affected area. A variety of apparatus or materials, including stents, coils, and polymers, can be inserted through the catheter and placed on the aneurysm area to protect the affected region of the vessel wall from hemodynamic effects [1, 3–5, 7–10]. In the context of the discussion presented above, devices employed to prevent aneurysm rupture are expected to become smaller to reduce the risks associated with invasive endovascular procedures and improve biocompatibility [11–17].

Developments of new imaging tools with increased spatial resolution and the general interest in the biomedical applications of nanotechnology motivate the present study [18–27]. In particular, the use of nanotechnologies to increase

TABLE 1: Incidence and risk factors of aneurysms.

Aneurysm type	Incidence and risk factors
Intracranial aneurysm (IC) [7]	About 30,000 patients are treated for IC ruptures each year in the US 60% of these cases ended up with disabilities or dead
Thoracic aortic aneurysm (TAA) [32, 33]	Incidence of 10.4 per 100,000 persons per year 2.9 to 3.5 rupture cases per 100,000 people annually
Abdominal aortic aneurysm (AAA) [4, 32, 34, 35]	150,000 cases per year Distribution of 12.5% in men and 5.2% in women in people between 75 and 84 years of age Ruptures have a 90% risk of death

the strength of blood vessels in the early stages of formation of aneurysms may prevent growth of the widening area. In this regard, molecularly guided assembly offers the opportunity to grow nanofibers directly on the tissue and it represents a unique opportunity for developing technologies acting on tissue-specific locations [28, 29]. Here, we report on the use of molecularly guided assembly of nanoparticles into a mesh consisting of nanofibers for improving the strength of blood vessels. We have explored the growth of silver nanofibers on the surface of blood vessels endothelial surfaces obtained from *sus scrofa domestica* (domestic pig) with the purpose of contributing to the current body of knowledge related to the applications of nanotechnology in biomedical science and tissue bioengineering research. The nanofibers are composed of small particles and clusters. This innovative approach targets novel biomedical applications for preventing the rupture of aneurysms. It is based on the assembly of silver into one dimensional nanostructures guided by mercaptoacetic acid ($\text{HSCH}_2\text{CO}_2\text{H}$) [30, 31]. The sulfur end of the thiol molecule attaches to silver, while the carboxylic acid end of another thiol which in turn is bonded to silver. The nanofibers form when water is removed from the dispersion and is completely irreversible. We found that the silver nanofibers increase the resistance of blood vessels towards deformation as compared to untreated tissue.

2. Materials and Methods

2.1. Synthesis of Silver-Thiol Dispersion: Precursors to Silver Nanofibers. About two (2) micrograms (μg) of silver nitrate (AgNO_3 , Fisher) were mixed with an equivalent number of moles of mercaptoacetic acid ($\text{HSCH}_2\text{CO}_2\text{H}$, Aldrich) and 10.0 mL of deionized water. The mixture was shaken by hand for a few of seconds and the suspension was stored at dark under room temperature.

2.2. Blood Vessels. Blood vessels were obtained from the head of a *sus scrofa domestica* that was donated by a local slaughter house: the animal was killed for marketing purposes and not for the measurements reported here. The head was kept frozen in a refrigerator and was allowed to defrost prior to the removal of samples containing blood vessels. Blood vessel-containing tissue samples were cut in sections measuring

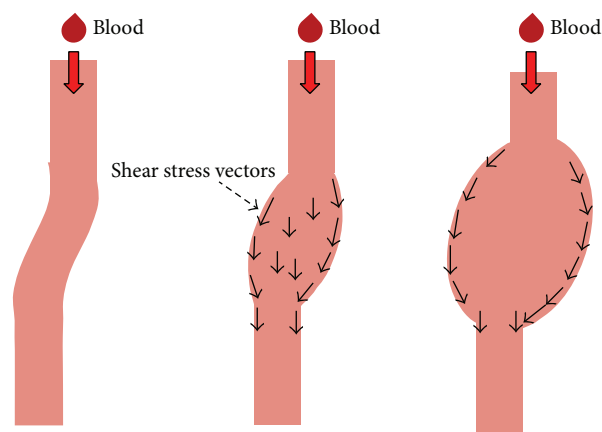


FIGURE 1: The formation and growth of aneurysm due to the shear stress caused by the intermittent blood flow. The drawing is intended to guide the eye through the text.

approximately 10 cm in length. A flow of air was passed through selected blood vessels to facilitate the dissection from the tissue (Figure 2(a)). Sections of the blood vessels were cut wide open to expose the internal endothelial surface. The blood vessel sections employed for the measurements presented in this work were 2 cm long, 2 cm wide and between 1 and 4 mm in depth (Figure 2(b)).

2.3. Preparation of Blood Vessels Treated with Nanofibers and Control Tissue. Regions of the internal endothelial surface of the blood vessels were treated with a total volume of 60.0 μL of the silver-thiol dispersion in 10 μL incremental steps. The internal blood vessels' endothelial surfaces were allowed to dry in air to allow for the formation of the silver nanofibers. Control tissue was prepared by treating regions of the internal endothelial surface of the blood vessels with a total volume of 60.0 μL of H_2O in 10 μL incremental steps.

2.4. Characterization of Nanofibers

2.4.1. SEM Imaging. SEM images were obtained with an environmental JEOL JSM-6460 LV SEM. Blood vessels were fixed to a conductive carbon tape and placed in the SEM analysis chamber. SEM images were collected with an acceleration

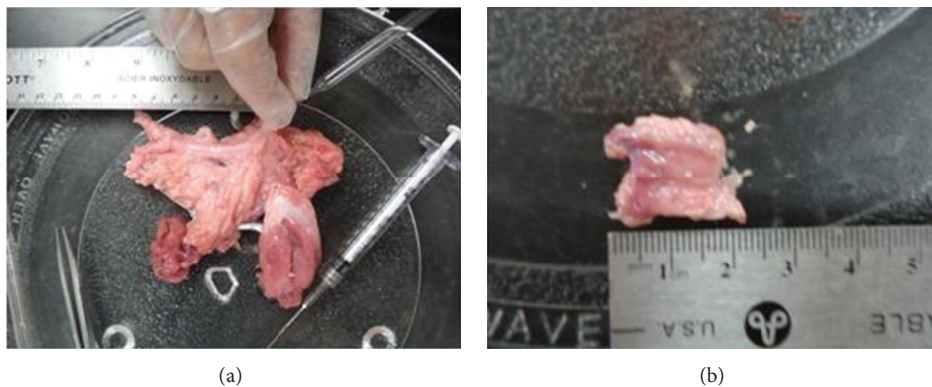


FIGURE 2: (a) Representative images of pieces of tissue containing blood vessels and (b) a piece of blood vessel cut wide open.

voltage of 5 kV in the high vacuum mode with spot sizes between 35 and 40. The diameter and length of the nanofibers were estimated from the SEM images using the software package provided by JEOL.

2.4.2. UV-Visible Measurements. UV-visible absorption spectroscopy measurements on dry deposits of the nanofibers formed on the surface of the blood vessels were performed with an Ocean Optics 2000 spectrometer coupled to an Olympus microscope operated in the reflection mode and UV grade optics. The Mie model of spheres and wires was used for simulation of the optical absorption spectrum [36]. The simulations were performed in a Dell PC using Igor software.

2.5. Determination of Displacement as a Function of Pressure. The deformation of the tissue was determined by applying a force with a pin. The blood vessel samples were placed on a flat aluminum holder. The holder has an aperture that is 1 cm in diameter to allow the pin to come in contact with the blood vessel surfaces. The area of the pin that comes into contact with the sample is 1.5 mm^2 . A cantilever system was developed and employed to apply the force on the tissue (see Figure 3). The cantilever consisted of a pin ($d = 1.4 \text{ mm}$) glued to the inner wall of a glass cylinder and a recipient at the other end to place a weight. The force was controlled by placing a known weight of sand on the recipient to drive the movement of the tip upward at the other end. The mass of the sand was determined with a Mettler Toledo microbalance model AT 20. The microbalance allowed the determination of the mass of the sand to within 10^{-6} grams. The displacement was determined using a calibrated ruler placed next to the tip. The displacement was recorded with a standard digital camera and was determined using commercially available software. A few micrograms of sand are needed to get the pin in touch with the tissue (region A). There is a region in which further addition of mass does not result in a measureable displacement (region B) until a small amount of sand added to the counterweight results in a displacement of the tip (Region C). That point is taken to correspond to the minimum force required to bend the internal blood vessels' endothelial surface.

3. Results

3.1. Optical Absorption Spectroscopy Measurements. The absorption spectra of thiol-silver dispersions have been published elsewhere [30]. It has absorption peaks due to silver dimers (Ag_2) in the ultraviolet region at 260 nm and 280 nm as well as a broader band resulting from light absorption by silver nanoparticles at 360 nm. Representative UV-visible absorption spectrum of the nanofibers grown on the blood vessel surface is illustrated on Figure 4. The experimental spectrum of the nanofibers that are formed when the water is removed from the dispersion has a continuous absorption band from the UV to the visible. No evidence is found for a localized band in the absorption spectrum of the nanofibers, in marked contrast to the absorption spectrum of the dispersion used to prepare the nanofibers that exhibits well-defined bands due to the absorption of light by silver nanoclusters and nanoparticles [30].

Light absorption by metallic silver results from a collective excitation of electrons known as plasmons. Silver nanoparticles have a transverse plasmon mode while a longitudinal plasmon mode can be observed in the spectrum of silver nanowires. Simulations of the absorption spectrum of wires and particles provided insight about the electronic excitations that contribute to the absorption spectrum of the nanofibers. The inserts (b) and (c) in Figure 4 illustrate computer simulations using Mie theory of the light absorption of particles and wires, respectively [36]. The simulation assumes wires with a length and diameter of $1 \mu\text{m}$ and 50 nm, respectively. The diameter of the spheres used in the simulation is 30 nm. The light absorbed by the wires is predicted to decrease with wavelength between 200 and 300 nm and to exhibit a sharp increase at 310 nm until it peaks at 360 nm. The amount of light absorbed by the wires is predicted to decrease gradually with wavelength from 360 nm up to 1000 nm. The spectrum simulated for the spheres, on the other hand, has a well-defined absorption band centered on 380 nm. The absorption spectrum of the nanofibers is remarkably similar to the one simulated for the wires. Thus, the tail toward long absorption wavelengths observed in the spectrum of the nanofibers results from excitations of the longitudinal plasmon mode in silver. This interpretation highlights the metallic character of the nanofibers that result

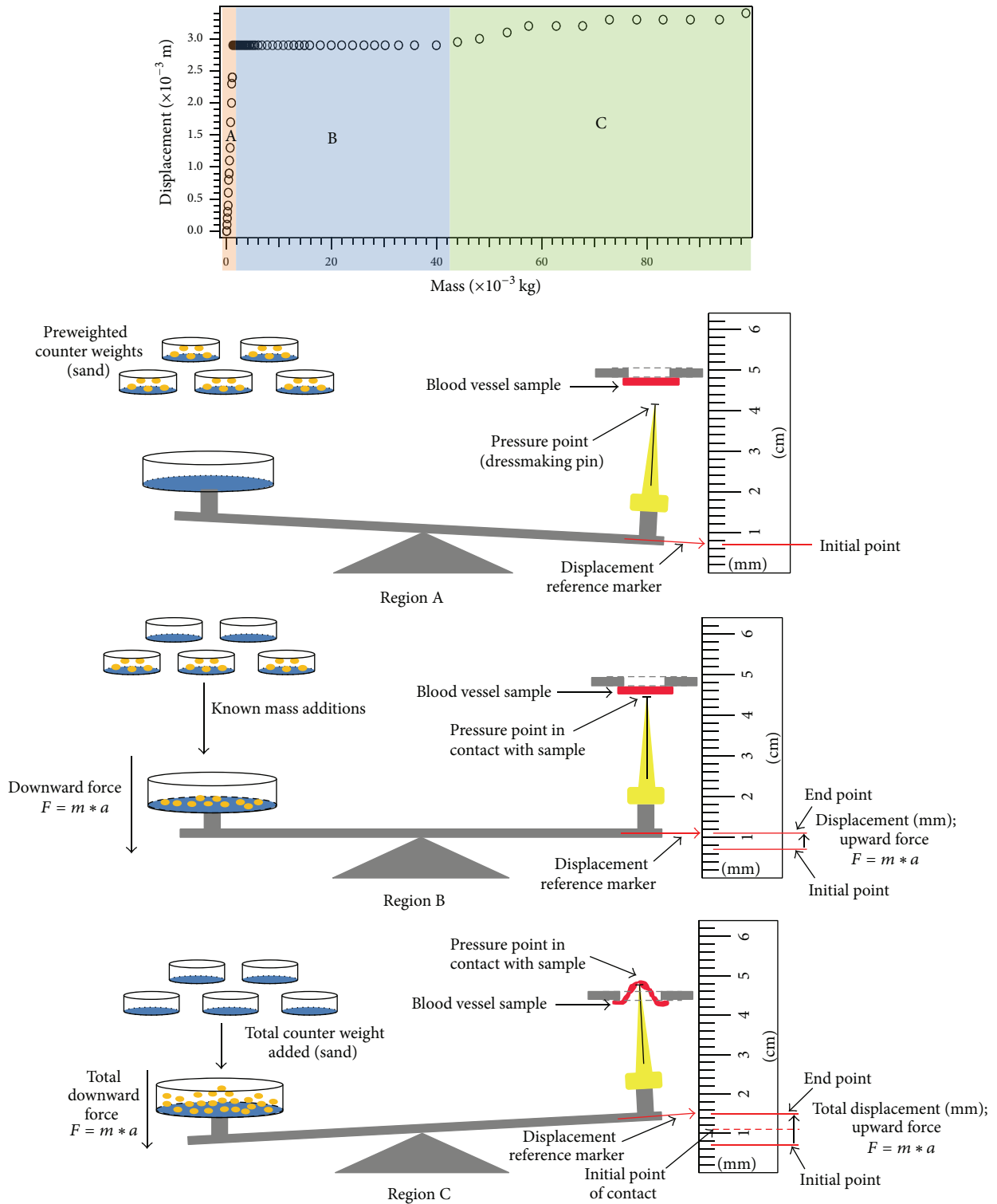


FIGURE 3: Experimental set up used to measure tissue deformation as a function of applied pressure. The pin has a free displacement (region A) until it reaches contact with the tissue (region B). There is a range in which the pressure applied with the pin is not enough to cause a deformation in the tissue, highlighted as region B in the figure. Further increase in the force applied with the pin results in the deformation of the tissue which is measured by a change in the displacement of the pin as highlighted by region C in the same figure. The force applied is estimated by the mass of the sand used to drive the movement of the pin.

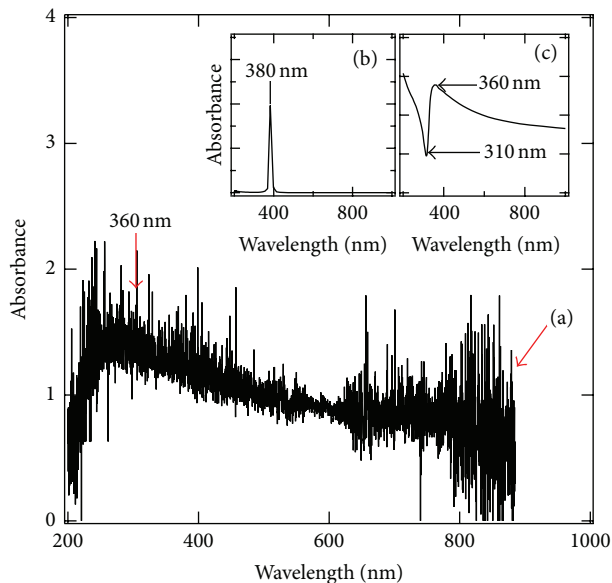


FIGURE 4: A representative absorption-reflection spectrum silver nanofiber deposited on the blood vessels is displayed on (a). The inserts (b) and (c) simulated absorption spectra of silver nanospheres with a diameter of 30 nm and silver nanowires with a length of $1 \mu\text{m}$ and 50 nm in diameter, respectively.

from coupling silver through molecular interactions among the thiol molecules. The absorption of light between 200 and 360 nm in the experimental spectrum likely results from the presence of thiol molecules in the sample.

3.2. Electron Microscopy Measurements. SEM measurements were performed to establish the morphology of the nanofibers grown on the surface of the blood vessel walls. A representative image of a region of the interior surface of blood vessels is labeled (a) on the upper left hand side of Figure 5. Representative images of areas of blood vessel surfaces where we have grown the nanofibers are labeled (b), (c), and (d) on Figure 5. The deposit of the nanofibers resembles a mesh of the order of several microns in the SEM image labeled (b). The nanofibers that compose the mesh can be identified in images obtained at slightly higher magnifications, like in Figures 5(c) and 5(d). The diameter and length distribution of the nanofibers grown on the surface of the blood vessels are summarized on Figures 5(e) and 5(f), respectively. The nanofibers are (120 ± 30) nm in diameter and have lengths of the order of $(2.7 \pm 0.8) \mu\text{m}$.

3.3. Effect of Silver Nanofibers on the Deformation of the Blood Vessel Tissue. The squares and circles in Figure 6 represent the displacement of the blood vessel surface as a function of the applied force in a control and nanofiber modified blood vessel, respectively. The deformation of the blood vessel is measured from the displacement of a pin head that exerts the indicated force on a 1.5 mm^2 area. There is an initial tension due to the procedure employed to hold the tissues that is

taken to be the same on both types of tissue samples; thus, our results must be taken by comparison among the control and modified tissue samples and should not be considered to represent absolute numbers. There is a region where no displacement is detected upon the application of an external force. This region is evident in the data summarized in the insert on the right hand side of Figure 6. The onset of displacement in the control and nanofiber treated blood vessel are observed around 3×10^{-3} and 3.4×10^{-1} N, respectively. We conclude that the resistance of the blood vessels toward deformation is increased by the presence of the nanofibers. This is further supported by analysis of the initial slope in the rise of the displacement with applied force. The slope of the initial rise in displacement with applied force is markedly different in both cases. The slopes of the rise in displacement with force are 0.15 and 0.003 m/N for the control and nanofibers modified tissue, respectively. The smaller slope in the deformation curve of the blood vessels modified by the nanofibers lead us to conclude that these nanostructures increase the resistance to deform the tissue.

4. Discussion

Metallic silver nanofibers form on the internal surface of blood vessel tissues from a silver-thiol dispersion. The silver nanofibers grown on the blood vessel surface are arranged in a mesh-like structure. We estimate a density of silver nanofibers of about 2 nanofibers/ μm^2 from the SEM measurements. This number is in close agreement to the average length of $(2.7 \pm 0.8) \mu\text{m}$ as well as with the peak in the distribution of lengths displayed on Figure 5.

The *tunica intima* is the layer of blood vessels closest to the blood. It is composed of a thin layer of endothelial cells, an internal elastic lamina and collagen fibers. Bundles of collagen fibrils and collagen fibers are found in the *tunica media* and *tunica adventitia*. The collagen fibers have an anisotropic arrangement and are an important element in providing resistance to the pressure load in blood vessels. Collagen is synthesized as pre procollagen, which is a primary structure containing specific regions of glycine, proline, and lysine residues.

Blood vessels modified by the silver nanofibers have a higher resistance toward deformation than control tissues. This is evidenced by the deformation measurements as a function of force. The initial slope of the deformation as a function of applied pressure in blood vessels modified with the silver nanofibers and the control are 0.003 m/N and 0.15 m/N, respectively. Thus, a given force will deform the modified tissue by a smaller amount than the control. This represents an increase in the resistance towards deformation of a factor of 50. This is clinically significant if we consider that blood pressure increases by factors slightly larger than one in the human body.

The blood vessels modified by the silver nanofibers are tissue that can carry the pressure load better than the tissue found in animals and humans. The Young's modulus or elastic modulus is a measure of the stiffness of a material. The elastic modulus (E) is directly proportional to the ratio of the applied

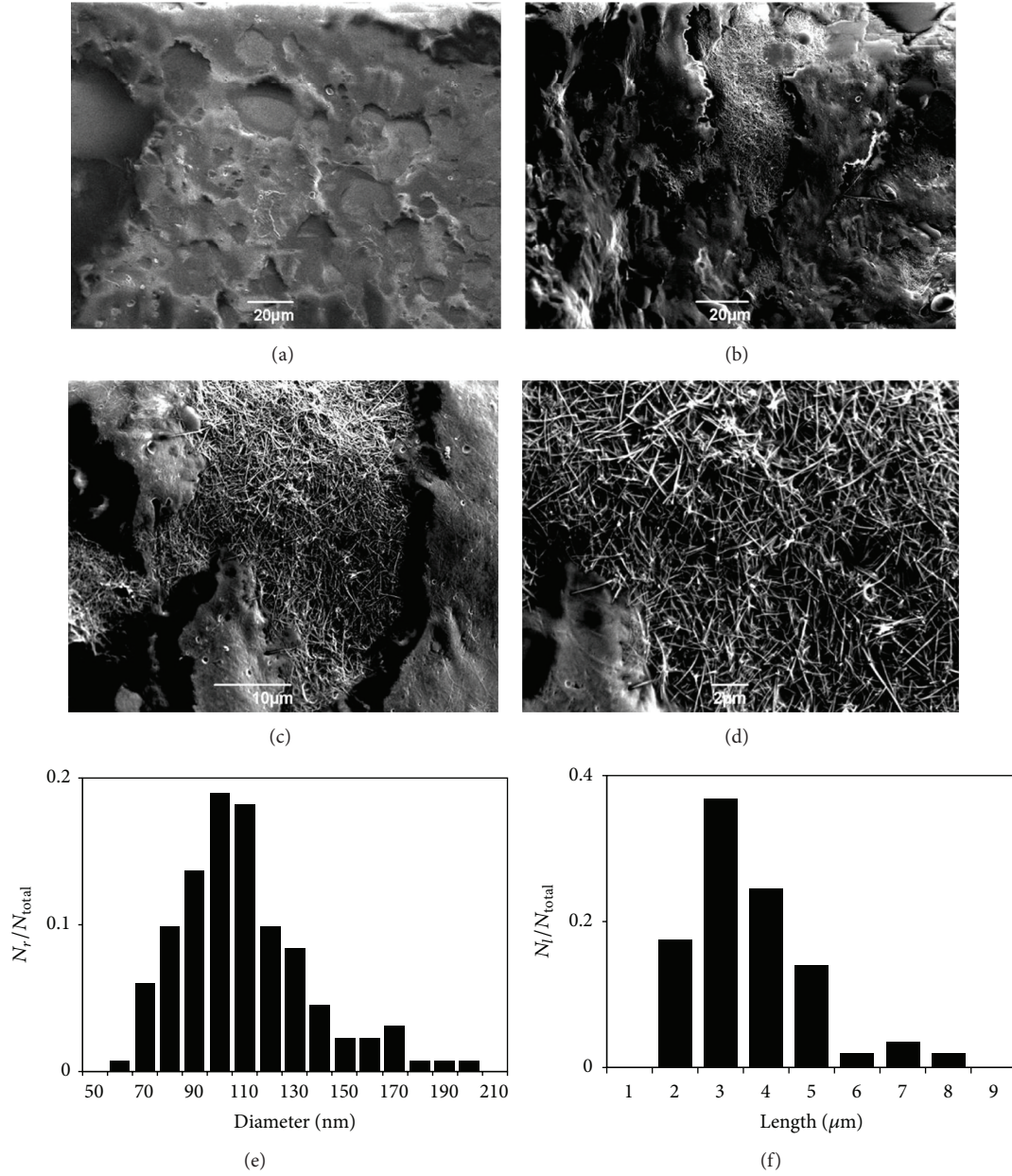


FIGURE 5: Representative SEM images of (a) the control blood vessel. Images of the surface of a blood vessel where the silver nanofibers were grown are labeled (b), (c), and (d). The diameter and length distribution of the one dimensional nanostructures grown on the surface of the blood vessels are illustrated in (e) and (f), respectively.

force (F) per unit area (A) and inversely proportional to the displacement (ΔL) relative to the length (L_o) of a material:

$$E = \frac{(F/A)}{(\Delta L/L_o)}. \quad (1)$$

An estimate of the elastic modulus of the system composed by the nanofibers on the blood vessel can be obtained from the slope of the dependence of the deformation on applied force. We estimate an elastic modulus between 1 and $3 \times 10^3 \text{ N/m}^2$ and $0.15 \times 10^3 \text{ N/m}^2$ for the blood vessels modified with the silver nanofibers and control, respectively. These values fall within the elastic modulus reported for blood vessels [37, 38].

The smaller displacement found in the tissue modified silver nanofibers as compared to the original material is consistent with the formation of stiff areas in the modified blood vessels. The risk of rupture of the blood vessel wall is reduced by the resistance towards deformation exhibited by the silver nanofibers treated blood vessel.

The measurements reported here were performed under static conditions and outside the physiological environment where blood vessels are found in humans. Further work in the use of this nanotechnology requires measurements of the effect of pressure on deformation of silver-nanofiber modified blood vessels in a dynamic and pulsed flow set up similar to

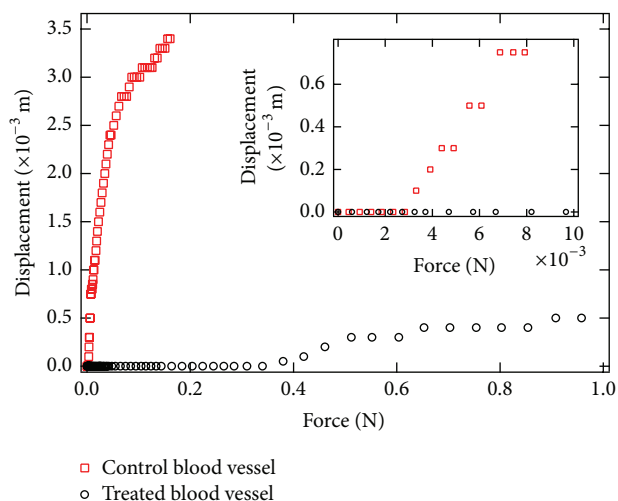


FIGURE 6: Dependence of the displacement, in meters (m), on the applied force, in newtons (N).

the one found in physiologically relevant environments and with tools to measure the deformation of the blood vessels *in vivo* [39]. Such experiments are currently outside the reach of our experimental setup and scope, yet this study advances the development of new nanotechnologies based on the use of silver nanostructures to prevent the rupture of aneurysms.

Conflict of Interests

The authors declare that there is no conflict of interests regarding the publication of this paper.

Acknowledgments

Miguel Gonzalez and Daniel Rivera acknowledge financial support from the National Institutes of Health RISE2BEST program under Grant no. R25GM088023. Miguel Gonzalez and Daniel Rivera also acknowledge partial financial support from the UPRM Sloan Graduate Program. Alam Marcelino and Gabriela Agront acknowledge support from the NIH/NIDDK Step Up Program Short-Term Education Program, grant number 1R25DK098067-01. Miguel Castro acknowledges support from UPR.

References

- [1] Aneurysm-PubMed Health, 2012, <http://www.ncbi.nlm.nih.gov/pubmedhealth/PMH0002109/>.
- [2] Aneurysm in the brain-PubMed Health, 2012, <http://www.ncbi.nlm.nih.gov/pubmedhealth/PMH0002387/>.
- [3] Abdominal aortic aneurysm-PubMed Health, 2012, <http://www.ncbi.nlm.nih.gov/pubmedhealth/PMH0001215/>.
- [4] D. A. Vorp, "Biomechanics of abdominal aortic aneurysm," *Journal of Biomechanics*, vol. 40, no. 9, pp. 1887–1902, 2007.
- [5] J. C. Lasheras, "The biomechanics of arterial aneurysms," *Annual Review of Fluid Mechanics*, vol. 39, pp. 293–319, 2007.
- [6] Abdominal aortic aneurysm repair-open, 2012, <http://www.umm.edu/ency/article/007392all.htm>.

- [7] Cerebral Aneurysms, 2012, <http://emedicine.medscape.com/article/1161518-overview>.
- [8] T. Mita, T. Arita, N. Matsunaga et al., "Complications of endovascular repair for thoracic and abdominal aortic aneurysm: an imaging spectrum," *Radiographics*, vol. 20, no. 5, pp. 1263–1278, 2000.
- [9] G. Piffaretti, M. Tozzi, C. Lomazzi, N. Rivolta, R. Caronno, and P. Castelli, "Complications after endovascular stent-grafting of thoracic aortic diseases," *Journal of Cardiothoracic Surgery*, vol. 1, no. 1, p. 26, 2006.
- [10] H. Meng, Z. Wang, Y. Hoi et al., "Complex hemodynamics at the apex of an arterial bifurcation induces vascular remodeling resembling cerebral aneurysm initiation," *Stroke*, vol. 38, no. 6, pp. 1924–1931, 2007.
- [11] R. Taylor and J. J. Norman, Nano and the Future of Endovascular Medicine: A Look at the Medical Advances We Expect in the Coming Decades.
- [12] Endovascular image-guided interventions (EIGIs) Browse-Medical Physics, 2013, <http://online.medphys.org/resource/1/mphysa6/v35/il/p301.s1?isAuthorized=no>.
- [13] A. W. Martinez and E. L. Chaikof, "Microfabrication and nanotechnology in stent design," *Wiley Interdisciplinary Reviews: Nanomedicine and Nanobiotechnology*, vol. 3, no. 3, pp. 256–268, 2011.
- [14] E. Fine, L. Zhang, H. Fenniri, and T. J. Webster, "Enhanced endothelial cell functions on rosette nanotube-coated titanium vascular stents," *International Journal of Nanomedicine*, vol. 4, no. 1, pp. 91–97, 2009.
- [15] K. Ishizaki, Y. Sugita, F. Iwasa et al., "Nanometer-thin TiO₂ enhances skeletal muscle cell phenotype and behavior," *International Journal of Nanomedicine*, vol. 6, pp. 2191–2203, 2011.
- [16] X. Li, R. Cui, W. Liu et al., "The use of nanoscaled fibers or tubes to improve biocompatibility and bioactivity of biomedical materials," *Journal of Nanomaterials*, vol. 2013, Article ID 728130, 16 pages, 2013.
- [17] H. Plenk Jr., G. M. Cruise, and J. C. Shum, "Hydrogel-coated and platinum coils for intracranial aneurysm embolization compared in three experimental models using computerized angiographic and histologic morphometry," *Journal of Materials Chemistry*, vol. 17, no. 38, pp. 3965–3973, 2007.
- [18] R. H. Baughman, "Playing nature's game with artificial muscles," *Science*, vol. 308, no. 5718, pp. 63–65, 2005.
- [19] J. Choi, Y. Jun, S. Yeon, H. C. Kim, J. Shin, and J. Cheon, "Biocompatible heterostructured nanoparticles for multimodal biological detection," *Journal of the American Chemical Society*, vol. 128, no. 50, pp. 15982–15983, 2006.
- [20] D. K. Yi, S. T. Selvan, S. S. Lee, G. C. Papaefthymiou, D. Kundaliya, and J. Y. Ying, "Silica-coated nanocomposites of magnetic nanoparticles and quantum dots," *Journal of the American Chemical Society*, vol. 127, no. 14, pp. 4990–4991, 2005.
- [21] I.P. Chang, C. H. Kuo, and C. Chiang, "Preparation of fluorescent magnetic nanodiamonds and cellular imaging," *Journal of the American Chemical Society*, vol. 130, no. 46, pp. 15476–15481, 2008.
- [22] Y. Jun, J. Seo, and J. Cheon, "Nanoscaling laws of magnetic nanoparticles and their applicabilities in biomedical sciences," *Accounts of Chemical Research*, vol. 41, no. 2, pp. 179–189, 2008.
- [23] Y.-E. L. Koo, R. Agayan, M. A. Philbert, A. Rehemtulla, B. D. Ross, and R. Kopelman, "Photonic explorers based on multifunctional nanoplatforms: in vitro and in vivo biomedical applications," *ACS Symposium Series*, vol. 963, pp. 200–218, 2007.

- [24] S. Lal, S. E. Clare, and N. J. Halas, "Nanoshell-enabled photothermal cancer therapy: impending clinical impact," *Accounts of Chemical Research*, vol. 41, no. 12, pp. 1842–1851, 2008.
- [25] M. R. Abidian, K. A. Ludwig, T. C. Marzullo, D. C. Martin, and D. R. Kipke, "Interfacing conducting polymer nanotubes with the central nervous system: chronic neural recording using poly(3,4-ethylenedioxythiophene) nanotubes," *Advanced Materials*, vol. 21, no. 37, pp. 3722–3770, 2009.
- [26] F. Yang, R. Murugan, S. Ramakrishna, X. Wang, Y.-X. Ma, and S. Wang, "Fabrication of nano-structured porous PLLA scaffold intended for nerve tissue engineering," *Biomaterials*, vol. 25, no. 10, pp. 1891–1900, 2004.
- [27] S. L. Bechara, A. Judson, and K. C. Papat, "Template synthesized poly(ϵ -caprolactone) nanowire surfaces for neural tissue engineering," *Biomaterials*, vol. 31, no. 13, pp. 3492–3501, 2010.
- [28] M. Wahab, P. Schiller, R. Schmidt, and H.-J. Mögel, "Monte Carlo study of the self-assembly of achiral bolaform amphiphiles into helical nanofibers," *Langmuir*, vol. 26, no. 5, pp. 2979–2982, 2010.
- [29] M. Elango, V. Subramanian, A. P. Rahalkar, S. R. Gadre, and N. Sathyamurthy, "Structure, energetics, and reactivity of boric acid nanotubes: a molecular tailoring approach," *Journal of Physical Chemistry A*, vol. 112, no. 33, pp. 7699–7704, 2008.
- [30] E. A. Hernandez, B. Posada, R. Irizarry, and M. E. Castro, "Role of hydrogen bonding interactions in directing one-dimensional thiol-assisted growth of silver-based nanofibers," *Journal of Physical Chemistry B*, vol. 109, no. 15, pp. 7251–7257, 2005.
- [31] N. A. Kotov, Ed., *Nanoparticle Assemblies and Superstructures*, CRC Press, New York, NY, USA, 2005.
- [32] CDC-DHDSP-Fact Sheets-Aortic Aneurysm Fact Sheet, 2012, http://www.cdc.gov/dhdsp/data_statistics/fact_sheets/fs_aortic_aneurysm.htm.
- [33] W. D. Clouse, J. W. Hallett Jr., H. V. Schaff et al., "Acute aortic dissection: population-based incidence compared with degenerative aortic aneurysm rupture," *Mayo Clinic Proceedings*, vol. 79, no. 2, pp. 176–180, 2004.
- [34] D. Lloyd-Jones, R. J. Adams, T. M. Brown et al., "Executive summary: heart disease and stroke statistics—2010 update: a report from the american heart association," *Circulation*, vol. 121, no. 7, pp. e46–e215, 2010.
- [35] J. J. A. Mooij, "Neurosurgery [Springer: Erste Auflage]," in *European Manual of Medicine*, C. B. Lumenta, C. Di Rocco, and J. Haase, Eds., vol. 3, Springer, New York, NY, USA, 2010.
- [36] E. Mercado, S. Santiago, L. Baez et al., "One-dimensional silver nanostructures on single-wall carbon nanotubes," *Nanoscale Research Letters*, vol. 6, p. 602, 2011.
- [37] R. L. Wesly, R. N. Vaishnav, and J. C. A. Fuchs et al., "Static linear and nonlinear elastic properties of normal and arterialized venous tissue in dog and man," *Circulation Research*, vol. 37, no. 4, pp. 509–520, 1975.
- [38] J. Fromageau, S. Lerouge, R. L. Maurice, G. Soulez, and G. Cloutier, "Noninvasive vascular ultrasound elastography applied to the characterization of experimental aneurysms and follow-up after endovascular repair," *Physics in Medicine and Biology*, vol. 53, no. 22, pp. 6475–6490, 2008.
- [39] C. Robertson, K. Ikemura, T. B. Krasieva, and S. C. George, "Multiscale analysis of collagen microstructure with generalized image correlation spectroscopy and the detection of tissue prestress," *Biomaterials*, vol. 34, no. 26, pp. 6127–6132, 2013.

Research Article

Visualization of Iron-Binding Micelles in Acidic Recombinant Biom mineralization Protein, MamC

Sanjay Kashyap,¹ Taylor Woehl,¹ Carmen Valverde-Tercedor,² Miguel Sánchez-Quesada,² Concepción Jiménez López,² and Tanya Prozorov¹

¹ Ames Laboratory, U.S. Department of Energy, Ames, IA 50011, USA

² Department of Microbiology, University of Granada, Campus de Fuentenueva s/n, 18071 Granada, Spain

Correspondence should be addressed to Tanya Prozorov; tprozoro@ameslab.gov

Received 13 January 2014; Revised 1 March 2014; Accepted 2 March 2014; Published 7 April 2014

Academic Editor: Hao Bai

Copyright © 2014 Sanjay Kashyap et al. This is an open access article distributed under the Creative Commons Attribution License, which permits unrestricted use, distribution, and reproduction in any medium, provided the original work is properly cited.

Biological macromolecules are utilized in low-temperature synthetic methods to exert precise control over nanoparticle nucleation and placement. They enable low-temperature formation of a variety of functional nanostructured materials with properties often not achieved via conventional synthetic techniques. Here we report on the *in situ* visualization of a novel acidic bacterial recombinant protein, MamC, commonly present in the magnetosome membrane of several magnetotactic bacteria, including *Magnetococcus marinus*, strain MC-1. Our findings provide an insight into the self-assembly of MamC and point to formation of the extended protein surface, which is assumed to play an important role in the formation of biotemplated inorganic nanoparticles. The self-organization of MamC is compared to the behavior of another acidic recombinant iron-binding protein, Mms6.

1. Introduction

Biomimetics employs a variety of biological macromolecules such as matrices, scaffolds, and templating agents, with the protein-driven nucleation playing an important role in the formation and growth of templated inorganic nanocrystals [1–12]. Bioinspired synthesis of uniform magnetic functional materials is a subject of intense research worldwide, owing to the interest in their functionality and performance in many fields of technology, from high-density magnetic data recording to catalysis and cancer therapy [13–23]. The full-length recombinant acidic bacterial iron-binding protein, *his*-Mms6, was shown to promote the shape-specific formation of the nanocrystals, and this bioinspired approach was later utilized for templated synthesis of more complex and highly magnetic cobalt ferrite nanocrystals [13, 17, 21, 23–26]. Formation of an extended protein surface was assumed to facilitate nucleation and growth of uniform nanocrystals [15, 17, 22, 27]. Much less research has been done on MamC, a magnetosome protein present in *Magnetospirillum magnetotacticum* MS-1, *M. gryphiswaldense* MSR-1, *M. magneticum* AMB-1 magnetotactic vibrio MV-1, and *Magnetococcus marinus* MC-1 [28–31]. Similar to Mms6, MamC has a hydrophilic

C-terminus rich in amino acids containing hydroxyl and carboxyl groups; it also contains a hydrophobic N-terminus. The acidic C-terminus is assumed to have an active role in magnetite biomineralization [32].

While obtaining X-ray quality crystals of novel proteins and solving their structure can take years [33, 34], the latest generation scanning transmission electron microscopes (STEM) allow visualization of the functionality and templating action of these biomacromolecules with sufficiently high resolution at the nanoscale [12, 20, 35–53]. Moreover, use of fluid cell TEM holders allows examination of a variety of macromolecular complexes in their native, unaltered, fully hydrated state, providing a unique window into the high-resolution characterization of the dynamic phenomena taking place in biological structures in liquid [50, 54–57].

Here we report on the *in situ* characterization of a novel bacterial recombinant acidic biomineralization protein, MamC, and the binding of iron to the surface of this protein. Another bacterial recombinant iron-binding protein, Mms6, is used as a reference. Our results aid in understanding the protein self-assembly and the role it plays in the nucleation and growth of a biotemplated nanoparticle. Among the

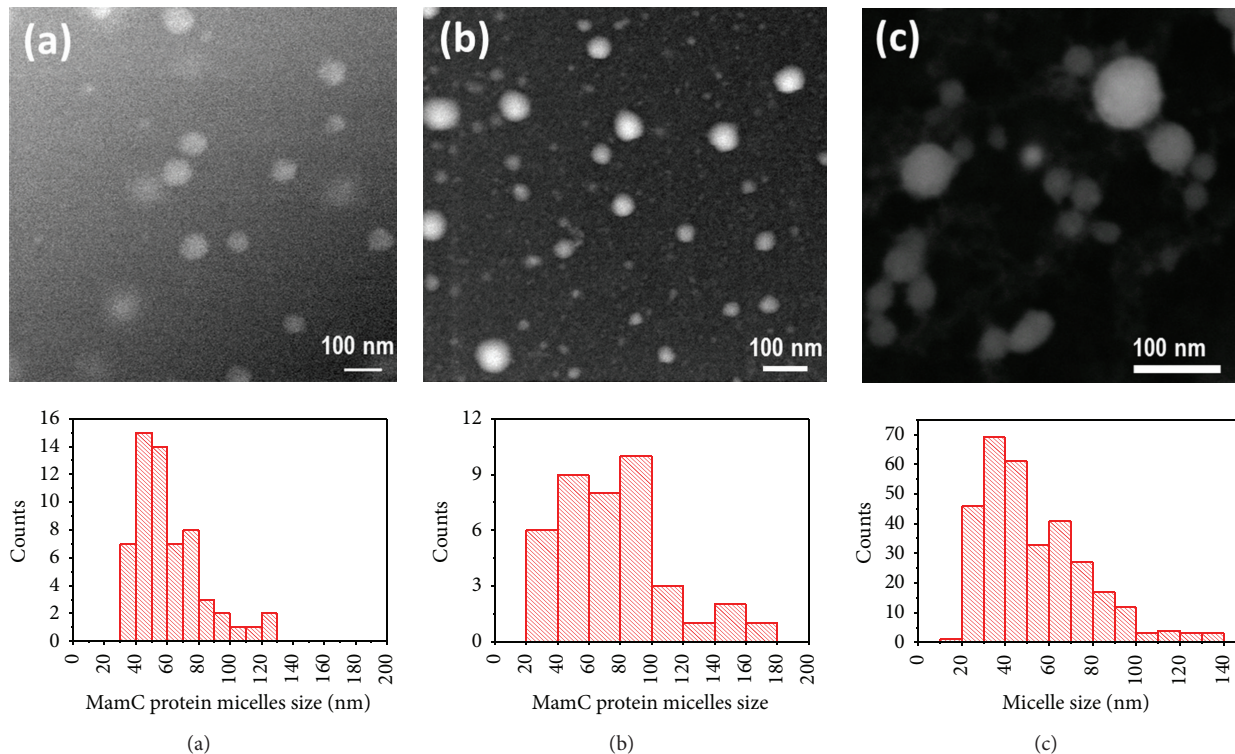


FIGURE 1: *In situ* HAADF-STEM images and size distribution of micelles of biomineralization recombinant proteins in liquid: (a) MamC before incubation and (b) after incubation with iron chloride; (c) Mms6 incubated with iron chloride, shown for comparison. Scale bars: 100 nm.

several acidic membrane proteins associated with the magnetosome magnetite membrane of magnetotactic bacteria, Mms6 and MamC are believed to be the dominant proteins involved in magnetosome formation and growth [24, 29, 58]. Moreover, since MamC represents one of the most commonly present and abundant proteins, and it is believed to be involved in regulating the size of the magnetosome magnetite crystals, MamC could be used in the biomimetic synthesis of shape-specific magnetite nanocrystals [59].

2. Results and Discussion

Figure 1 shows *in situ* fluid cell HAADF images of MamC micelles in liquid and micelle size distribution obtained (a) before and (b) after overnight incubation with ferric chloride. The intensity of the HAADF-STEM images depends primarily on the atomic number, Z , and mass thickness of the specimen, thus providing chemical, compositional, and morphological information of the sample. The enhancement in the contrast of the iron-incubated micelles in Figure 1(b) was attributed to the surface localization of iron: due to iron's higher atomic number with respect to the surrounding organic material, it is easily detected with the HAADF detector. Here the positively charged ferrous ions appear to bind preferentially to the negatively charged protein micelles. *In situ* HAADF STEM provides a visual qualitative confirmation of surface iron binding. These findings are in good agreement with the zeta potential of MamC, $\zeta = -22.5 \pm 2$ mV, which is

indicative of a net negative surface charge, thus facilitating the binding of iron cations. Figure 1(c) shows iron-incubated micelles in Mms6 and their size distribution for comparison. Similar to the iron-incubated MamC micelles, the Mms6 micelle shows a relatively large HAADF signal compared to the background, due to the presence of iron.

The iron-incubated protein micelles appear to undergo further self-assembly and form an extended surface (Figures 2 and 4). Iron surface binding results in an increased surface concentration of iron ions with higher atomic number, rendering the micelle-bound ferrous iron highly visible in the HAADF image. The surface-localized iron binding leads to a local increase in the iron supersaturation at the surface of the protein micelles, enabling the biomimetic formation of biomimetic iron oxide nanocrystals external to the micelle core, with virtually no size restrictions. For example, magnetite nanocrystals synthesized in the presence of Mms6 exhibit, on average, the mean size of 30 nm, while those synthesized in the presence of MamC have an average size of 80 nm [57, 59, 60]. Such a scenario is drastically different from the case of the ferritin-templated nanocrystals growth, where the nanoparticles nucleate and mature within the protein cages and cannot outgrow the cage size, and yields the nanocrystals of 5–8 nanometers [1, 61].

To ensure stability of specimens, minimize their thickness, and provide an adequate signal, additional characterization of MamC incubated with ferric chloride was performed with the protein prepared on a conventional EM grid.

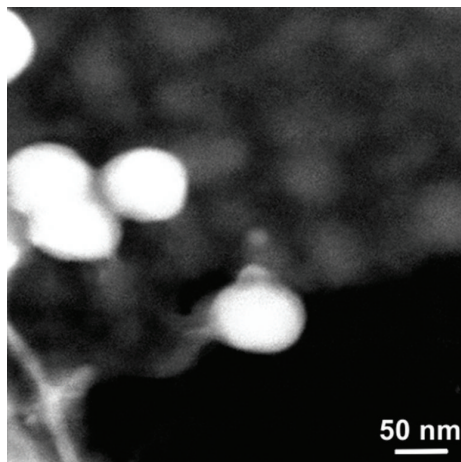


FIGURE 2: HAADF-STEM *in situ* characterization of MamC incubated with ferric chloride: (a) the iron-rich micelles are aggregating into larger hierarchical structures. The micelles in front are closer to the surface and appear in focus, whereas the micelles in the back, slightly out of focus, appear to be tightly packed.

Figures 3(a)–3(c) show elemental maps acquired in EFTEM mode for the zero loss region (a), Fe $L_{2,3}$ -edge (b), and O K-edge (c) energy loss values. EFTEM confirms the localized presence of oxygen and iron in MamC proteinaceous micelles incubated with ferric chloride. Since the iron energy loss is observed at higher energy levels compared to that of oxygen, the iron peaks are weaker; however, the elements are clearly distinguishable. The *in situ* HAADF (Figures 1 and 2) and EFTEM (Figure 3) images together provide strong evidence for the iron-binding ability of MamC micelles.

3. Experimental Section

3.1. Materials and Reagents. All aqueous solutions were prepared with deionized water passed through a Millipore Milli-Q Plus water purification system ($\lambda = 18.2 \text{ M}\Omega$) and sparged with argon for 15 min. (3-Aminopropyl)triethoxysilane (APTES, 99%) and ferric chloride hexahydrate ($\text{FeCl}_3 \cdot 6\text{H}_2\text{O}$, >99%) were purchased from Sigma Aldrich and used without purification. The amount of protein in solution was maintained at $0.67 \mu\text{M}$; MamC was incubated with $10 \mu\text{M}$ ferric chloride solution prepared from the deoxygenated 0.5 M stock solution.

Purified recombinant protein MamC from *Magnetococcus marinus* was obtained by cloning and expressing the gene *mmc1_2265* [31] into *E. coli* (TOP10) then disrupting the cells, and purifying the lysate following the protocol described by Valverde-Tercedor et al. [62], with the following modifications: (1) *mmc1_2265* was amplified by polymerase chain reaction by using the following specific primers: fw3 (5'-ATGGCTGCCTTTAATTTGGCACTG-3') and rev2 (5'-TTACGGAGTTTCCAACCTCGGGATC-3'). (2) The expression conditions for the recombinant MamC protein by *E. coli* (TOP10) (TrcHisTOPO_ *mmc1_2265*) were 2 mM of IPTG for 5 hours at 37°C . (3) The purification was done using ÄKTA Prime Plus FPLC System (GE Healthcare) under denaturing conditions in a urea gradient. After elution of the

protein, it was dialyzed overnight at 4°C against 1 L of Buffer 1 (20 mM phosphate buffer pH 8.0, 4 M urea, and 0.5 M NaCl). To reduce the concentration of urea, the dialysis buffer was diluted stepwise 1:2 (four times) with Buffer 2 (50 mM Tris, 150 mM NaCl, pH 8.5) and dialyzed for another 2–4 h after each dilution step. The isoelectric point for MamC (I_{ep} 5.09) was calculated using the ExPASy ProtParam tool [59].

Cloning and purification of the recombinant Mms6 from the *M. Magnetococcus* AMB-1 have been reported previously [17, 25, 27]. The Mms6 used in the study was dialyzed against 20 mM TRIS, 100 mM KCl, pH 7.45 buffer.

3.2. Specimen Preparation. To minimize the thickness of the liquid layer, the protein solutions were deposited onto plasma-cleaned TEM-transparent substrates, silicon nitride window membranes for the *in situ* imaging (Figures 1 and 2), and carbon-coated Au grids (QuantiFoil) for EFTEM imaging (Figure 3), using a Nano eNabler molecular printer (BioForce). Use of the Nano eNabler permitted the deposition of femtoliter volume droplets of liquid [63, 64]. Surface patterning tools (SPTs) with diameters of $10 \mu\text{m}$ and $30 \mu\text{m}$ were used for the specimen patterning. Prior to the liquid specimen loading, SPTs were treated with UV/ O_3 plasma for 30 min to oxidize organic residues and form a thin layer of silicon oxide on the wall of channels and reservoirs, rendering them highly hydrophilic. Loading of the liquid specimen was performed immediately after the UV/ O_3 plasma cleaning [64].

3.3. Functionalization of Silicon Nitride Windows. Silicon nitride windows membranes were cleaned by triple rinsing in toluene, then chemically pure acetone, and finally ethanol, followed by cleaning in UV/ O_3 plasma for 45 minutes. Immediately after the plasma cleaning, the window membranes were functionalized with (3-aminopropyl)triethoxysilane (APTES), which is a covalent linker to facilitate protein immobilization on the surface [65, 66]. To ensure protein integrity during the specimen deposition, silicon nitride windows were patterned on a custom-made cold stage at 7°C .

3.4. Dynamic Light Scattering. Dynamic light scattering (DLS) and measurements of zeta potentials of the protein solutions were carried out with a Zetasizer Nanoparticle analyzer (Model: ZEN3690, Malvern Instrument Ltd., Southborough, MA). Prior to analysis, the buffer was filtered through a $0.2 \mu\text{m}$ nitrocellulose membrane and the protein specimens were centrifuged for 20 minutes (1000 rpm, 23°C). The measurements were performed on numerous 10-second acquisitions with 3 repeats. Data were processed by using Dispersion Technology Software 5.00 (Malvern Instrument Ltd.).

3.5. In Situ Fluid Cell Characterization. The iron-binding proteins were examined with a Continuous Flow Fluid Cell TEM Holder Platform (Hummingbird Scientific). After the patterning with the Nano eNabler, the windows were assembled and sealed in the liquid cell holder platform, resulting in the liquid specimen being sandwiched between the electron-transparent silicon nitride window membranes. Imaging and

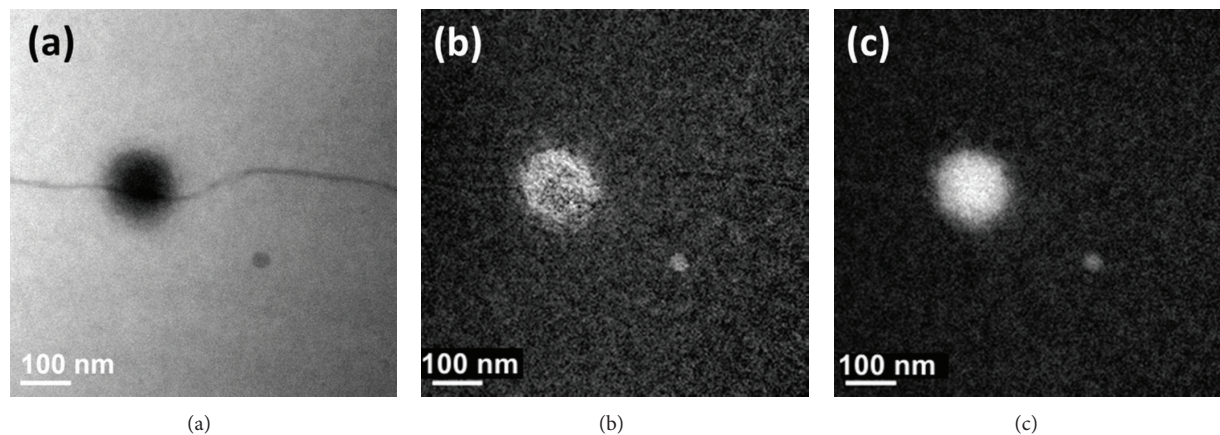


FIGURE 3: EFTEM images of MamC micelles prepared on a carbon grid. (a) Zero-loss image and elemental maps of (b) iron and (c) oxygen. Scale bar: 100 nm.

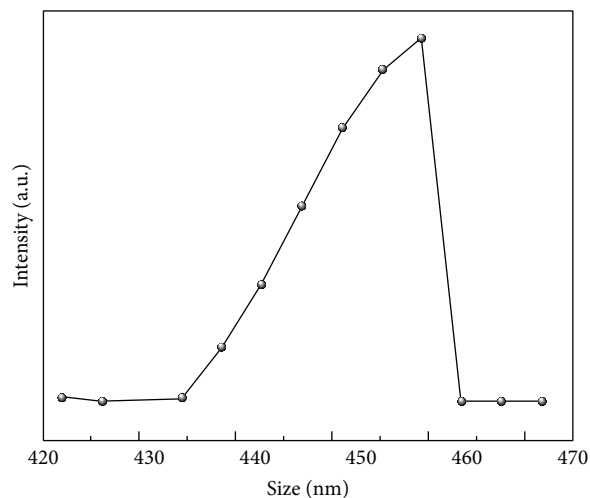
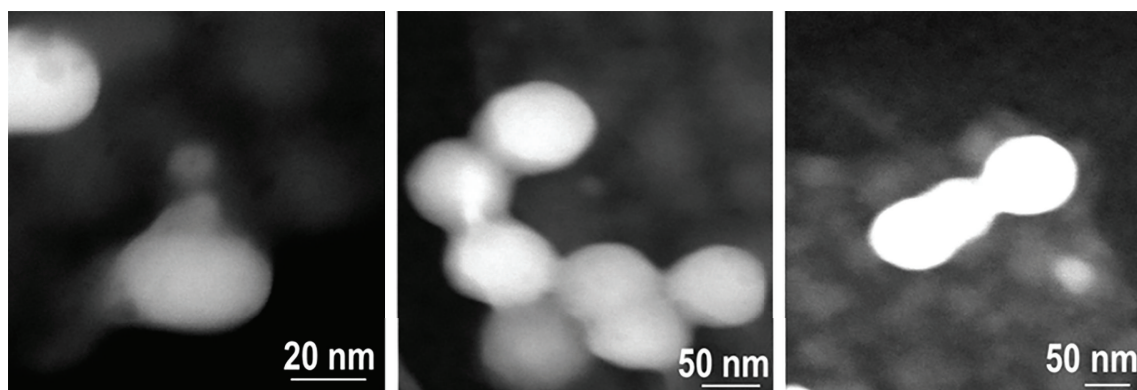


FIGURE 4: HAADF-STEM *in-situ* visualization of micellar aggregates in MamC incubated with ferric chloride overnight. The micelles in the back, slightly out of focus, appear to be tightly packed. (a) Representative images. Note the differences in the scale bars. Scale bar on the left: 20 nm; scale bars in the middle and on the right: 50 nm. (b) Intensity-based particle size distribution of micellar aggregates in MamC specimen incubated with iron overnight.

characterization of the specimens were carried out with an FEI Tecnai G² F20 (S)TEM operating at an accelerating voltage of 200 kV equipped with a Tridiem Gatan Imaging Filter (GIF), High Angle Annular Dark Field (HAADF), and energy dispersive X-ray spectroscopy (EDS) detectors. *In situ* fluid delivery was carried out with a syringe pump with the variable pumping speed (2–5 $\mu\text{L}/\text{min}$). For comparison, specimens were also printed on conventional EM grids and examined with a standard single-tilt holder. To ensure reproducibility of results, the sizes of micelles were determined from numerous HAADF images. Electron energy loss spectroscopy (EELS) was used to probe the localized chemical composition of the liquid specimens. EELS spectra and elemental maps were acquired in energy-filtered transmission electron microscopy (EFTEM) mode. Elemental maps of oxygen and iron were acquired with a slit width of $30\text{ eV} \pm 1\text{ eV}$. EELS spectra were acquired with a slit width of 10 eV and dispersion of 0.5 eV/pixel. Data analysis was performed with Digital Micrograph software (GMS version 2.11.1404.0) and OriginPro 9.0 software. To ensure reproducibility of results, micelle sizes were measured on micelles imaged in numerous micrographs obtained with the HAADF detector.

4. Conclusions

We have visualized micelles of MamC recombinant iron-binding protein *in situ* by utilizing the STEM-HAADF contrast enhancement of surface bound iron species. Further self-organization of iron-incubated MamC micelles produced iron-rich extended surfaces and points to enhanced iron binding. Our results represent a significant step forward in understanding the process of self-organization of iron-binding recombinant proteins employed in bioinspired synthesis of magnetic nanoparticles. Our findings are applicable for the *in situ* characterization of a variety of inorganic-organic interfaces in protein solutions.

Conflict of Interests

The authors declare that there is no conflict of interests regarding the publication of this paper.

Acknowledgments

This work was supported by the U.S. Department of Energy, Office of Science, Basic Energy Sciences, Materials Sciences and Engineering Division. The research was performed at the Ames Laboratory, which is operated for the U.S. Department of Energy by Iowa State University under Contract no. DE-AC02-07CH11358. MamC cloning and purification were done at the University of Granada, Spain. Concepción Jiménez López acknowledges the support from the Spanish Government through Grant CGL2010-18274 and the program Salvador de Madariaga. The authors thank the Laboratory of Professor Marit Nilsen-Hamilton for providing the recombinant biomineralization protein, Mms6.

References

- [1] M. T. Klem, M. Young, and T. Douglas, "Biomimetic magnetic nanoparticles," *Materials Today*, vol. 8, no. 9, pp. 28–37, 2005.
- [2] F. C. Meldrum, B. R. Heywood, and S. Mann, "Magnetoferritin: in vitro synthesis of a novel magnetic protein," *Science*, vol. 257, no. 5069, pp. 522–523, 1992.
- [3] D. Resnick, K. Gilmore, Y. U. Idzerda, M. Klem, E. Smith, and T. Douglas, "Modeling of the magnetic behavior of $\gamma\text{-Fe}_2\text{O}_3$ nanoparticles mineralized in ferritin," *Journal of Applied Physics*, vol. 95, no. 11, pp. 7127–7129, 2004.
- [4] I. Grunwald, K. Rischka, S. M. Kast, T. Scheibel, and H. Bargel, "Mimicking biopolymers on a molecular scale: nano(bio)technology based on engineered proteins," *Philosophical Transactions of the Royal Society A: Mathematical, Physical and Engineering Sciences*, vol. 367, no. 1894, pp. 1727–1747, 2009.
- [5] J. J. de Yoreo and P. M. Dove, "Shaping crystals with biomolecules," *Science*, vol. 306, no. 5700, pp. 1301–1302, 2004.
- [6] S. Foerster, "Amphiphilic block copolymers for templating applications," in *Colloid Chemistry I*, vol. 226 of *Topics in Current Chemistry*, pp. 1–28, Springer, Berlin, Germany, 2003.
- [7] D. E. Morse, M. M. Murr, B. Schwenzer, J. R. Gomm, and R. L. Brutchey, "Silicatein proteins reveal unique mechanisms of hierarchical self-assembly and catalytic nanofabrication, leading to a new, generic, low-temperature method for catalytic nanofabrication," in *Proceedings of the 233rd ACS National Meeting*, vol. 96, p. 1, 2007.
- [8] C. Nardin and W. Meier, "Hybrid materials from amphiphilic block copolymers and membrane proteins," *Reviews in Molecular Biotechnology*, vol. 90, no. 1, pp. 17–26, 2002.
- [9] A. Wolff, K. Frese, M. Wissbrock et al., "Influence of the synthetic polypeptide c25-mms6 on cobalt ferrite nanoparticle formation," *Journal of Nanoparticle Research*, vol. 14, article 1161, 2012.
- [10] D. W. P. M. Löwik, L. Ayres, J. M. Smeenk, and J. C. M. van Hest, "Synthesis of bio-inspired hybrid polymers using peptide synthesis and protein engineering," *Advances in Polymer Science*, vol. 202, no. 1, pp. 19–52, 2006.
- [11] C. Tamerler and M. Sarikaya, "Molecular biomimetics: nanotechnology and bionanotechnology using genetically engineered peptides," *Philosophical Transactions of the Royal Society A: Mathematical, Physical and Engineering Sciences*, vol. 367, no. 1894, pp. 1705–1726, 2009.
- [12] M. H. Nielsen, J. R. Lee, S. Aloni, and J. J. de Yoreo, in *Proceedings of the 239th ACS National Meeting*, San Francisco, Calif, USA, March 2010.
- [13] Y. Amemiya, A. Arakaki, S. S. Staniland, T. Tanaka, and T. Matsunaga, "Controlled formation of magnetite crystal by partial oxidation of ferrous hydroxide in the presence of recombinant magnetotactic bacterial protein Mms6," *Biomaterials*, vol. 28, no. 35, pp. 5381–5389, 2007.
- [14] A. Arakaki, M. Tanaka, and T. Matsunaga, in *Proceedings of the International Chemical Congress of Pacific Basin Societies (Pacifichem '10)*, Honolulu, Hawaii, USA, December 2010.
- [15] T. Prozorov, D. A. Bazylnski, S. K. Mallapragada, and R. Prozorov, "Novel magnetic nanomaterials inspired by magnetotactic bacteria: topical review," *Materials Sciences and Engineering R: Reports*, vol. 74, no. 5, pp. 133–172, 2013.
- [16] T. Prozorov, S. K. Mallapragada, B. Narasimhan et al., "Protein-mediated synthesis of uniform superparamagnetic magnetite nanocrystals," *Advanced Functional Materials*, vol. 17, no. 6, pp. 951–957, 2007.

- [17] T. Prozorov, P. Palo, L. Wang et al., "Cobalt ferrite nanocrystals: out-performing magnetotactic bacteria," *ACS Nano*, vol. 1, no. 3, pp. 228–233, 2007.
- [18] K.-I. Sano, K. Ajima, K. Iwahori et al., "Endowing a ferritin-like cage protein with high affinity and selectivity for certain inorganic materials," *Small*, vol. 1, no. 8-9, pp. 826–832, 2005.
- [19] P. Tartaj, M. del Puerto Morales, S. Veintemillas-Verdaguer, T. González-Carreño, and C. J. Serna, "The preparation of magnetic nanoparticles for applications in biomedicine," *Journal of Physics D: Applied Physics*, vol. 36, no. 13, pp. R182–R197, 2003.
- [20] Y. Y. Zheng, X. B. Wang, L. Shang et al., "Fabrication of shape controlled Fe_3O_4 nanostructure," *Materials Characterization*, vol. 61, no. 4, pp. 489–492, 2010.
- [21] J. M. Galloway, A. Arakaki, F. Masuda, T. Tanaka, T. Matsunaga, and S. S. Staniland, "Magnetic bacterial protein Mms6 controls morphology, crystallinity and magnetism of cobalt-doped magnetite nanoparticles in vitro," *Journal of Materials Chemistry*, vol. 21, no. 39, pp. 15244–15254, 2011.
- [22] J. M. Galloway, J. P. Bramble, A. E. Rawlings, G. Burnell, S. D. Evans, and S. S. Staniland, "Biotemplated magnetic nanoparticle arrays," *Small*, vol. 8, no. 2, pp. 204–208, 2012.
- [23] J. M. Galloway, J. P. Bramble, A. E. Rawlings, G. Burnell, S. D. Evans, and S. S. Staniland, "Nanomagnetic arrays formed with the biomineralization protein Mms6," *Journal of Nano Research*, vol. 17, pp. 127–146, 2012.
- [24] A. Arakaki, J. Webb, and T. Matsunaga, "A novel protein tightly bound to bacterial magnetic particles in *Magnetospirillum magneticum* strain AMB-1," *The Journal of Biological Chemistry*, vol. 278, no. 10, pp. 8745–8750, 2003.
- [25] T. Prozorov, S. K. Mallapragada, B. Narasimhan et al., "Protein-mediated synthesis of uniform superparamagnetic magnetite nanocrystals," *Advanced Functional Materials*, vol. 17, no. 6, pp. 951–957, 2007.
- [26] L. Wang, T. Prozorov, P. E. Palo et al., "Self-assembly and biphasic iron-binding characteristics of Mms6, a bacterial protein that promotes the formation of superparamagnetic magnetite nanoparticles of uniform size and shape," *Biomacromolecules*, vol. 13, no. 1, pp. 98–105, 2012.
- [27] S. Feng, L. Wang, P. Palo, X. Liu, S. K. Mallapragada, and M. Nilsen-Hamilton, "Integrated self-assembly of the Mms6 magnetosome protein to form an iron-responsive structure," *International Journal of Molecular Sciences*, vol. 14, no. 7, pp. 14594–14606, 2013.
- [28] K. Grünberg, E. C. Mueller, A. Otto et al., "Biochemical and proteomic analysis of the magnetosome membrane in *Magnetospirillum gryphiswaldense*," *Applied and Environmental Microbiology*, vol. 70, no. 2, pp. 1040–1050, 2004.
- [29] K. Grünberg, C. Wawer, B. M. Tebo, and D. Schüler, "A large gene cluster encoding several magnetosome proteins is conserved in different species of magnetotactic bacteria," *Applied and Environmental Microbiology*, vol. 67, no. 10, pp. 4573–4582, 2001.
- [30] M. Tanaka, Y. Okamura, A. Arakaki, T. Tanaka, H. Takeyama, and T. Matsunaga, "Origin of magnetosome membrane: proteomic analysis of magnetosome membrane and comparison with cytoplasmic membrane," *Proteomics*, vol. 6, no. 19, pp. 5234–5247, 2006.
- [31] S. Schübbe, T. J. Williams, G. Xie et al., "Complete genome sequence of the chemolithoautotrophic marine magnetotactic coccus strain MC-1," *Applied and Environmental Microbiology*, vol. 75, no. 14, pp. 4835–4852, 2009.
- [32] A. Scheffel, A. Gärdes, K. Grünberg, G. Wanner, and D. Schüler, "The major magnetosome proteins MamGFDC are not essential for magnetite biomineralization in *Magnetospirillum gryphiswaldense* but regulate the size of magnetosome crystals," *Journal of Bacteriology*, vol. 190, no. 1, pp. 377–386, 2008.
- [33] I. D. Campbell and B. Sheard, "Protein structure determination by NMR," *Trends in Biotechnology*, vol. 5, no. 11, pp. 302–306, 1987.
- [34] A. Ilari and C. Savino, "Protein structure determination by X-ray crystallography," in *Bioinformatics*, J. Keith, Ed., vol. 452 of *Methods in Molecular Biology*, pp. 63–87, Humana Press, 2008.
- [35] J. S. Kim, T. LaGrange, B. W. Reed et al., "Imaging of transient structures using nanosecond in situ TEM," *Science*, vol. 321, no. 5895, pp. 1472–1475, 2008.
- [36] R. Sharma, "Kinetic measurements from in situ TEM observations," *Microscopy Research and Technique*, vol. 72, no. 3, pp. 144–152, 2009.
- [37] G. H. Campbell, T. B. LaGrange, W. E. King et al., "The HCP to BCC phase transformation in Ti characterized by nanosecond electron microscopy," in *Proceedings of the International Conference on Solid-Solid Phase Transformations in Inorganic Materials*, vol. 2, pp. 443–448, June 2005.
- [38] X. D. Bai, Z. Xu, K. H. Liu, and E. G. Wang, "In situ TEM probing properties of individual one-dimensional nanostructures," *International Journal of Nanotechnology*, vol. 4, no. 1-2, pp. 119–128, 2007.
- [39] L. J. Chen, W. W. Wu, and C. H. Liu, "In situ ultrahigh vacuum transmission electron microscope investigations of dynamical changes of nanostructures on silicon," *Advanced Science and Technology*, vol. 46, pp. 111–119, 2006.
- [40] M. Tanase and A. K. Petford-Long, "In situ TEM observation of magnetic materials," *Microscopy Research and Technique*, vol. 72, no. 3, pp. 187–196, 2009.
- [41] H. Zheng, R. K. Smith, Y.-W. Jun, C. Kisielowski, U. Dahmen, and A. P. Alivisatos, "Observation of single colloidal platinum nanocrystal growth trajectories," *Science*, vol. 324, no. 5932, pp. 1309–1312, 2009.
- [42] C. B. Murray, "Watching nanocrystals grow," *Science*, vol. 324, no. 5932, pp. 1276–1277, 2009.
- [43] Z. H. Cao, P. Liu, X. K. Meng, S. C. Tang, and H. M. Lu, "In situ transmission electron microscopy observations of the crystallization of amorphous Ge films," *Applied Physics A: Materials Science and Processing*, vol. 94, no. 2, pp. 393–398, 2009.
- [44] H. D. Espinosa, B. Peng, R. Agrawal, and R. A. Bernal, "In situ TEM experiments to assess the predictive capability of atomistic models," *Microscopy and Microanalysis*, vol. 16, pp. 1756–1757, 2010.
- [45] D. H. Anjum, R. M. Stiger, J. J. Finley, and J. F. Conway, "Cryo-transmission electron microscopy of Ag nanoparticles grown on an ionic liquid substrate," *Journal of Materials Research*, vol. 25, no. 7, pp. 1264–1271, 2010.
- [46] J. M. Grogan and H. H. Bau, "The nanoaquarium: a platform for in situ transmission electron microscopy in liquid media," *Journal of Microelectromechanical Systems*, vol. 19, no. 4, pp. 885–894, 2010.
- [47] J. E. Evans, I. Arslan, N. D. Browning et al., "Studying materials in-situ with the dynamic transmission electron microscope (DTEM)," *Microscopy and Microanalysis*, vol. 16, pp. 320–321, 2010.

- [48] G. H. Campbell, T. Lagrange, J. S. Kim, B. W. Reed, and N. D. Browning, "Quantifying transient states in materials with the dynamic transmission electron microscope," *Journal of Electron Microscopy*, vol. 59, no. 1, pp. S67–S74, 2010.
- [49] G. Crivat and J. W. Taraska, "Imaging proteins inside cells with fluorescent tags," *Trends in Biotechnology*, vol. 30, no. 1, pp. 8–16, 2012.
- [50] J. E. Evans, K. L. Jungjohann, P. C. K. Wong et al., "Visualizing macromolecular complexes with in situ liquid scanning transmission electron microscopy," *Micron*, vol. 43, no. 11, pp. 1085–1090, 2012.
- [51] L. Zhang, J. Song, G. Cavigliolo et al., "Morphology and structure of lipoproteins revealed by an optimized negative-staining protocol of electron microscopy," *Journal of Lipid Research*, vol. 52, no. 1, pp. 175–184, 2011.
- [52] B. Jachimska, M. Wasilewska, and Z. Adamczyk, "Characterization of globular protein solutions by dynamic light scattering, electrophoretic mobility, and viscosity measurements," *Langmuir*, vol. 24, no. 13, pp. 6867–6872, 2008.
- [53] T. Uchihashi, N. Kodera, and T. Ando, "Guide to video recording of structure dynamics and dynamic processes of proteins by high-speed atomic force microscopy," *Nature Protocols*, vol. 7, pp. 1193–1206, 2012.
- [54] C. Colliex, "Materials science: watching solution growth of nanoparticles in graphene cells," *Science*, vol. 335, no. 6077, pp. 44–45, 2012.
- [55] K. L. Klein, I. M. Anderson, and N. de Jonge, "Transmission electron microscopy with a liquid flow cell," *Journal of Microscopy*, vol. 242, no. 2, pp. 117–123, 2011.
- [56] E. A. Ring and N. de Jonge, "Microfluidic system for transmission electron microscopy," *Microscopy and Microanalysis*, vol. 16, no. 5, pp. 622–629, 2010.
- [57] L. Wang, T. Prozorov, P. E. Palo et al., "Self-assembly and biphasic iron-binding characteristics of Mms6, a bacterial protein that promotes the formation of superparamagnetic magnetite nanoparticles of uniform size and shape," *Biomacromolecules*, vol. 13, no. 1, pp. 98–105, 2012.
- [58] N. Ginot, R. Pardoux, G. Adryanczyk, D. Garcia, C. Brutesco, and D. Pignol, "Single-step production of a recyclable nanobio-catalyst for organophosphate pesticides biodegradation using functionalized bacterial magnetosomes," *PLoS ONE*, vol. 6, no. 6, Article ID e21442, 2011.
- [59] C. Valverde-Tercedor, M. Montalbán-López, T. Trubitsyn et al., "Size control of in vitro synthesized magnetite crystals by MamC from *Magnetococcus marinus* MC-1," *Biomaterials*. In press.
- [60] A. Wolff, N. Mill, K. Eckstadt et al., "Oriented attachment explains cobalt ferrite nanoparticle growth in bioinspired syntheses," *Beilstein Journal of Nanotechnology*, vol. 5, p. 210, 2014.
- [61] T. Douglas and V. T. Stark, "Nanophase cobalt oxyhydroxide mineral synthesized within the protein cage of ferritin," *Inorganic Chemistry*, vol. 39, no. 8, pp. 1828–1830, 2000.
- [62] C. Valverde-Tercedor, F. Abadía-Molina, M. Martínez-Bueno et al., "Subcellular localization of the magnetosome protein MamC in the marine magnetotactic bacterium *Magnetococcus marinus* strain MC-1 using immunoelectron microscopy," *Archives of Microbiology*. In press.
- [63] J. Xu, M. Lynch, J. L. Huff et al., "Microfabricated quill-type surface patterning tools for the creation of biological micro/nano arrays," *Biomedical Microdevices*, vol. 6, no. 2, pp. 117–123, 2004.
- [64] J. Xu, M. Lynch, S. Nettikadan, C. Mosher, S. Vegasandra, and E. Henderson, "Microfabricated "biomolecular ink cartridges"—surface patterning tools (SPTs) for the printing of multiplexed biomolecular arrays," *Sensors and Actuators B: Chemical*, vol. 113, no. 2, pp. 1034–1041, 2006.
- [65] K.-W. Huang, C.-W. Hsieh, H.-C. Kan et al., "Improved performance of aminopropylsilatrane over aminopropyltriethoxysilane as a linker for nanoparticle-based plasmon resonance sensors," *Sensors and Actuators B: Chemical*, vol. 163, no. 1, pp. 207–215, 2012.
- [66] A. Huang, F. Liang, F. Steinbach, and J. Caro, "Preparation and separation properties of LTA membranes by using 3-aminopropyltriethoxysilane as covalent linker," *Journal of Membrane Science*, vol. 350, no. 1–2, pp. 5–9, 2010.

Research Article

The Promotion of Human Neural Stem Cells Adhesion Using Bioinspired Poly(norepinephrine) Nanoscale Coating

Minah Park,¹ Mikyung Shin,² Eunmi Kim,¹ Slgirim Lee,¹ Kook In Park,³
Haeshin Lee,^{2,4} and Jae-Hyung Jang¹

¹ Department of Chemical and Biomolecular Engineering, Yonsei University, 262 Seongsanno, Seodaemun-gu, Seoul 120-749, Republic of Korea

² The Graduate School of Nanoscience and Technology, KAIST, Daejeon 305-701, Republic of Korea

³ Department of Pediatrics, College of Medicine, Yonsei University, Seoul 120-749, Republic of Korea

⁴ Department of Chemistry, The Graduate School of Nanoscience and Technology, Korea Advanced Institute of Science and Technology (KAIST), 291 University Road, Daejeon 305-701, Republic of Korea

Correspondence should be addressed to Haeshin Lee; haeshin@kaist.ac.kr and Jae-Hyung Jang; j-jang@yonsei.ac.kr

Received 21 November 2013; Accepted 12 February 2014; Published 7 April 2014

Academic Editor: Jingxia Wang

Copyright © 2014 Minah Park et al. This is an open access article distributed under the Creative Commons Attribution License, which permits unrestricted use, distribution, and reproduction in any medium, provided the original work is properly cited.

The establishment of versatile biomaterial interfaces that can facilitate cellular adhesion is crucial for elucidating the cellular processes that occur on biomaterial surfaces. Furthermore, biomaterial interfaces can provide physical or chemical cues that are capable of stimulating cellular behaviors by regulating intracellular signaling cascades. Herein, a method of creating a biomimetic functional biointerface was introduced to enhance human neural stem cell (hNSC) adhesion. The hNSC-compatible biointerface was prepared by the oxidative polymerization of the neurotransmitter norepinephrine, which generates a nanoscale organic thin layer, termed poly(norepinephrine) (pNE). Due to its adhesive property, pNE resulted in an adherent layer on various substrates, and pNE-coated biointerfaces provided a highly favorable microenvironment for hNSCs, with no observed cytotoxicity. Only a 2-hour incubation of hNSCs was required to firmly attach the stem cells, regardless of the type of substrate. Importantly, the adhesive properties of pNE interfaces led to micropatterns of cellular attachment, thereby demonstrating the ability of the interface to organize the stem cells. This highly facile surface-modification method using a biomimetic pNE thin layer can be applied to a number of suitable materials that were previously not compatible with hNSC technology.

1. Introduction

Creating biomaterial interfaces that are capable of inducing intimate interactions with cells is a crucial step to elucidating the sophisticated cellular processes occurring on biomaterial surfaces in numerous biomedical applications. The surface properties of cell-material interfaces can influence cellular events related to cellular attachment, patterning, proliferation, and differentiation [1, 2]. Indeed, interfaces contacting the cellular membrane not only influence cellular morphology but also function as intermediates that can supplement the molecular signals that direct various biological processes [3, 4]. However, the generation of appropriate interfacial environments that can effectively regulate intracellular signaling

cascades and control cellular fates remains a challenge. One solution is the use of a material that is capable of functioning as an interface, with the crucial requirement that the material be able to promote cellular attachment on its surface.

Numerous surface-modification methods have been employed to enhance cellular adhesion. The majority of modification approaches have attempted to interact with target cells through the chemical tethering or physical adsorption of particular biological moieties, such as integrin ligands [5], specialized peptides [6], growth factors [7], or functionalized chemicals [8], onto the modified surfaces. Additionally, modifications of surface properties, as achieved by producing self-assembled monolayers or by engaging organosilane chemistry, have been employed to regulate interactions with

cells [9]. The manipulation of surface properties, resulting in variations in cellular attachment and cellular patterning, has been attempted using various lithographic techniques, including writing-based lithography [10–12] or surface graft polymerization approaches [13]. Additionally, the topographical changes of three-dimensional cell-culture structures [14], well-defined structural patterns [15], and surface rigidity [16] directly influenced cell adhesion on substrates and survivals as well. However, several issues, such as the requirement of organic solvents, difficulty in the large-scale production of modified surfaces, requirement of expensive instruments, or time-consuming labor requirements, may limit the extensive utilization of these techniques in various applications.

The adhesive properties of catecholamine compounds, as characterized by the sticky characteristics of the foot proteins of marine mussels, have been reported to be useful sources for universally modifying numerous surfaces [9, 17, 18]. The adhesive properties of catecholamines, representatively as poly(dopamine), have helped to realize the efficient immobilization of biomolecules onto surfaces with various chemistries [18]. A surface can also be functionalized by dissolving biomolecules with catecholamine, particularly poly(dopamine), during nanoscale organic thin layer formation, ultimately leading to the surface immobilization of biomolecules. Furthermore, secondary modifications can be performed through surface-initiated polymerization and biomineralization [19]. Importantly, the facile approach of using a catecholamine group as a coating agent not only allows flexibility in the selection of the substrate materials but is also an inexpensive and ecofriendly process [20]. Lastly, the spatial arrangement of the surface adhesiveness may result in the patterned regulation of cellular behaviors, including differentiation, proliferation, and migration [17, 21].

Recently, the neurotransmitter norepinephrine has been shown to functionalize virtually any material surface when it is oxidatively polymerized to produce poly(norepinephrine) (pNE) [22, 23]. The pNE coating layer exhibits unique properties, such as ring-opening polymerization and the storage/release of nitric oxide [24]. Nonetheless, the capability of facilitating stem cell adhesion onto a pNE layer has not been investigated to date. In this study, we demonstrate that a pNE layer can be formed on various substrates (poly(dimethylsiloxane) (PDMS), poly(tetrafluoroethylene) (PTFE), tissue culture polystyrene (TCP), and glass), resulting in the dramatic enhancement of the adhesion of hNSCs isolated from human fetal brain. Additionally, the hNSC viability was not compromised, and cellular and cytoskeletal morphology were assessed. Considering the very low adhesive properties of hNSCs, our study shows that the formation of a pNE nanolayer can be a good platform for the stable culture of hNSCs, which may support the *ex vivo* expansion of therapeutic stem cells.

2. Experimental Section

2.1. Cell Culture. Human fetal neural stem cells (hNSC, 13 weeks of gestational age) were utilized to analyze cellular adhesion, patterning, and proliferation on pNE interfaces

formed on various substrates and transduction efficiencies. hNSCs were derived from the telencephalon (HFT13) as previously described [25] and cultured in Dulbecco's modified Eagle's medium/F12 (Invitrogen, Carlsbad, CA, USA) containing N-2 supplement, 8 mg/mL heparin (Sigma-Aldrich, St Louis, MO, USA), 20 ng/mL fibroblast growth factor-2 (FGF-2; R&D Systems, Minneapolis, MN, USA), and 10 ng/mL leukemia inhibitory factor (LIF; Chemicon, Temecula, CA, USA).

2.2. Substrate Preparation and pNE Coating. Four different substrates, including glass (Marienfeld GmbH, Germany), poly(dimethylsiloxane) (PDMS; Sylgard 184, Dow Corning, MI, U.S.A), poly(tetrafluoroethylene) (PTFE; Hanmi Rubber & Plastics, Korea), and tissue culture polystyrene surfaces, were sterilized in 70% ethanol and rinsed with sterile-distilled water prior to pNE modification. PDMS was prepared using a SYLGARD 184 silicone elastomer kit (Dow Corning Corporation, Midland, MI, USA) according to the manufacturer's guidelines. Each substrate was immersed in 1 mL of 10 mM Tris (pH 8.5) solution containing 2 mg L-(-)-norepinephrine in 1 mL of 10 mM Tris (pH 8.5) at room temperature for 24 hours. During this procedure, norepinephrine monomers polymerize to form pNE interfaces on the surface of each substrate. The coated substrates were additionally sterilized with 70% ethanol, rinsed twice with sterile-distilled water, and air-dried. The surface wettability and morphology of each pNE-coated surface were determined by contact angle measurements (CAM 101, KSV Instruments Ltd., Espoo, Finland) and atomic force measurements (AFM) (XE-BIO AFM, Parks Systems, Korea), respectively. Additionally, the root mean square (RMS) roughness (R_q) of the modified surfaces was measured by the AFM analysis.

2.3. Cellular Attachment on pNE-Coated Substrate. Each substrate coated with the pNE interface was placed in the wells of a 48-well tissue culture plate using silicone grease, and hNSCs were seeded at a cell density of 10^4 cells/ $10 \mu\text{L}$. The cells were incubated for an hour at 37°C and 5% CO_2 , and $200 \mu\text{L}$ of medium was subsequently added to feed the cells on each substrate. An hour later, the substrates with cells were placed in new wells, and the cells were trypsinized from the surface to quantify the number of cells that had successfully attached to the surface during the short culture period (~1 hour). The number of cells was counted using a hemocytometer.

2.4. Morphologies of Cells Attached on pNE-Coated Substrate. The cytoskeletal morphology of the cells adhered to each pNE-coated substrate was assessed by visualizing filamentous actin, which was stained using rhodamine-labeled phalloidin (1:50 dilution in PBS) (Invitrogen, Carlsbad, CA, USA); the nuclei were counterstained using DAPI (Vector Laboratories, Burlingame, CA). Briefly, the coating of each substrate with the pNE interface and cellular attachment was performed according to the aforementioned methodology, and the remaining cells on each substrate were cultured for 2 days prior to the histological analysis. The cells were subsequently

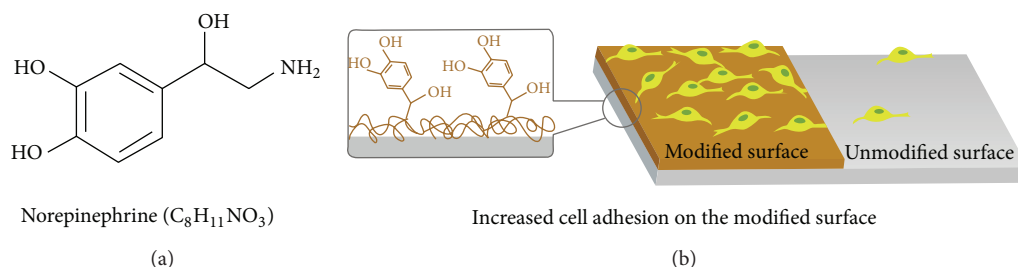


FIGURE 1: Surface modification using pNE. (a) Chemical structure of norepinephrine. (b) Schematic illustration of the pNE-coated biointerfaces onto which hNSCs are adhered.

fixed in 4% paraformaldehyde (PFA) for 20 minutes and blocked with 5% goat serum supplemented with 0.1% Triton X-100. The cells were incubated with rhodamine-labeled phalloidin (Invitrogen, Carlsbad, CA, USA) for 30 minutes in the dark, rinsed three times with PBS, and counterstained with DAPI for 30 minutes. The fluorescence images of both the cytoskeletal morphology and nucleus of the cells were acquired using confocal microscopy (LSM 700, Carl Zeiss).

2.5. Cellular Cytotoxicity Assay on pNE-Coated Substrates.

To determine the cytotoxicity of the pNE interfaces, the metabolic activities of hNSCs cultured on each pNE-coated surface were analyzed using a WST-1 assay kit (Roche Applied Science, Indianapolis, IN) according to the manufacturer's protocol. After 2, 4, and 6 days of culture on each pNE-coated substrate, a 0.1 volume of WST-1 solution (as a proportion of the culture medium) was directly added to each well and incubated for an additional 2 hours at 37°C. The supernatants were collected, and the colorimetric changes at 440 nm were measured using a spectrophotometer (NanoDrop 2000, Thermo Scientific, West Palm Beach, FL, USA).

2.6. Macro- or Microscale Cellular Patterning on pNE-Coated Substrates.

To produce cellular patterns with macroscales (~mm), specific patterns of the pNE interfaces, such as a "Y" shape, were generated by simply drawing the shape with the pNE solution using a micropipette and incubating at 37°C overnight to form the patterned interface. Tissue culture plates were employed as a representative of the cellular patterning due to the ease of analyzing the cellular patterns with a microscope. After washing with PBS, the cells were subsequently seeded at 6×10^6 cells/mL; after 2 hours, the cells barely attached to the substrate were removed by gently washing with PBS. After being fixed with 4% PFA, the remaining cells were stained with Hoechst dye (Sigma-Aldrich, St Louis, MO, USA). The images of the cellular patterns were acquired using a fluorescence microscope (Nikon TE2000E2, Nikon, Japan). PDMS stamping technology was utilized to generate cellular patterns on a microscale (~100 μm). Briefly, a PDMS micropattern with line alignments was initially generated with a specified dimension (ridge, 100 μm ; groove, 200 μm ; and depth, 120 μm). The PDMS stamp was immersed into a pNE solution (2 mg/mL of norepinephrine in 10 mM Tris at pH 8.5), which was prepolymerized for 24 hours, placed on the tissue culture plate, and pressed manually for 2

minutes. The unbound pNE interfaces on the tissue culture plates were removed by rinsing twice with PBS, and cells at 6×10^6 cells/mL were seeded for attachment to the pNE interfaces on the glass. As with the macroscale patterning, the cells barely attached to the pNE interface were removed by washing with PBS after 2 hours, and the nuclei of the remaining cells were stained with DAPI and imaged using a fluorescence microscope (Nikon TE2000E2, Nikon, Japan) to visualize the cellular alignment and the pNE patterns generated by the PDMS stamp.

2.7. Statistics. All of the experimental data are illustrated as the mean \pm the standard deviation (SD), and statistical significances were analyzed by a one-way analysis of variance (ANOVA) with a post hoc Dunnett's test using the SPSS 18.0 software package (IBM Corporation, Somers, NY, USA).

3. Results and Discussion

Figure 1 schematically shows the generation of biointerfaces by pNE coating. The chemical structure shown in the figure is catechol, which is responsible for robust adhesion onto substrates and the rapid immobilization of biological components for cell adhesion. As illustrated, the pNE layer is rich in hydroxyl groups: two hydroxyl groups from catechol and one from alkyl chain. It is known that a new intermediate component, 3,4-dihydroxybenzaldehyde (DHBA), is formed, which subsequently reacts with norepinephrine (NE) to yield DHBA-NE during the oxidative polymerization of norepinephrine. It has recently been shown that DHBA functions as a key factor contributing a conformal, smooth coating on a substrate in comparison to the well-known surface functionalization of poly(dopamine) [24]. Similar to the case of poly(dopamine), we hypothesized that pNE thin layers can effectively promote neural stem cell adhesion. Unlike typical mammalian cells, hNSCs do not adhere stably to tissue culture polystyrene dishes. Thus, the development of a culture platform promoting hNSC adhesion is a critical issue in the ex vivo expansion of stem cells for cell therapy. To test the functionality of pNE as a coating agent, a wide range of materials, including poly(tetrafluoroethylene) (PTFE), poly(dimethylsiloxane) (PDMS), glass, and tissue culture polystyrene (TCP) surfaces, were modified using the dip-coating method in an alkaline norepinephrine solution [22], as described in Figure 1(b). These substrates were chosen

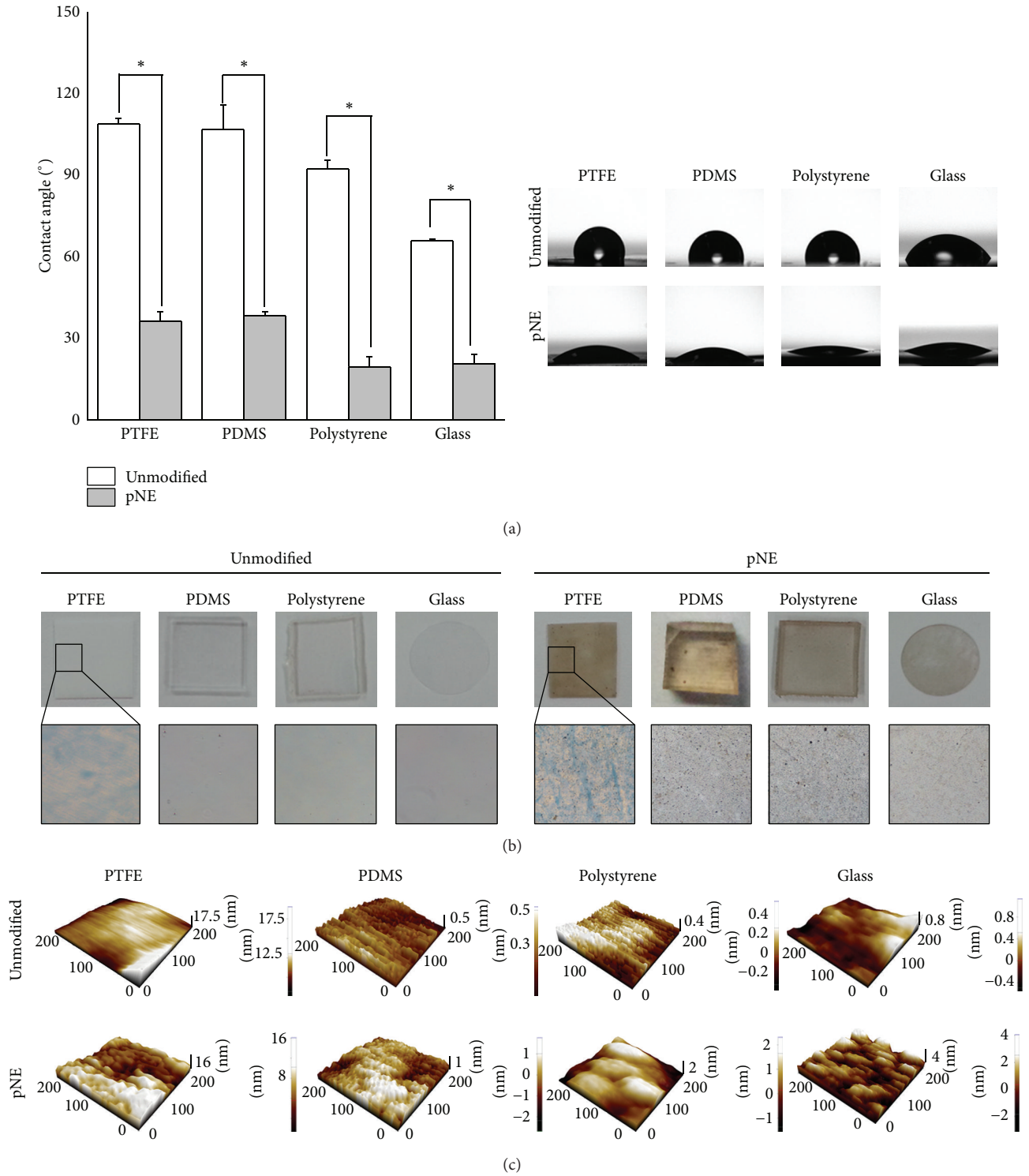


FIGURE 2: Characterization of pNE surfaces. (a) Surface wettability is measured by a goniometer. The symbol * indicates a significant difference compared to each unmodified substrate ($P < 0.005$). (b) Representative digital images of pNE-coated PTFE, PDMS, glass, and TCP substrates. The dark brown colors indicate pNE coating. (c) Topographical images of pNE interfaces using AFM analysis.

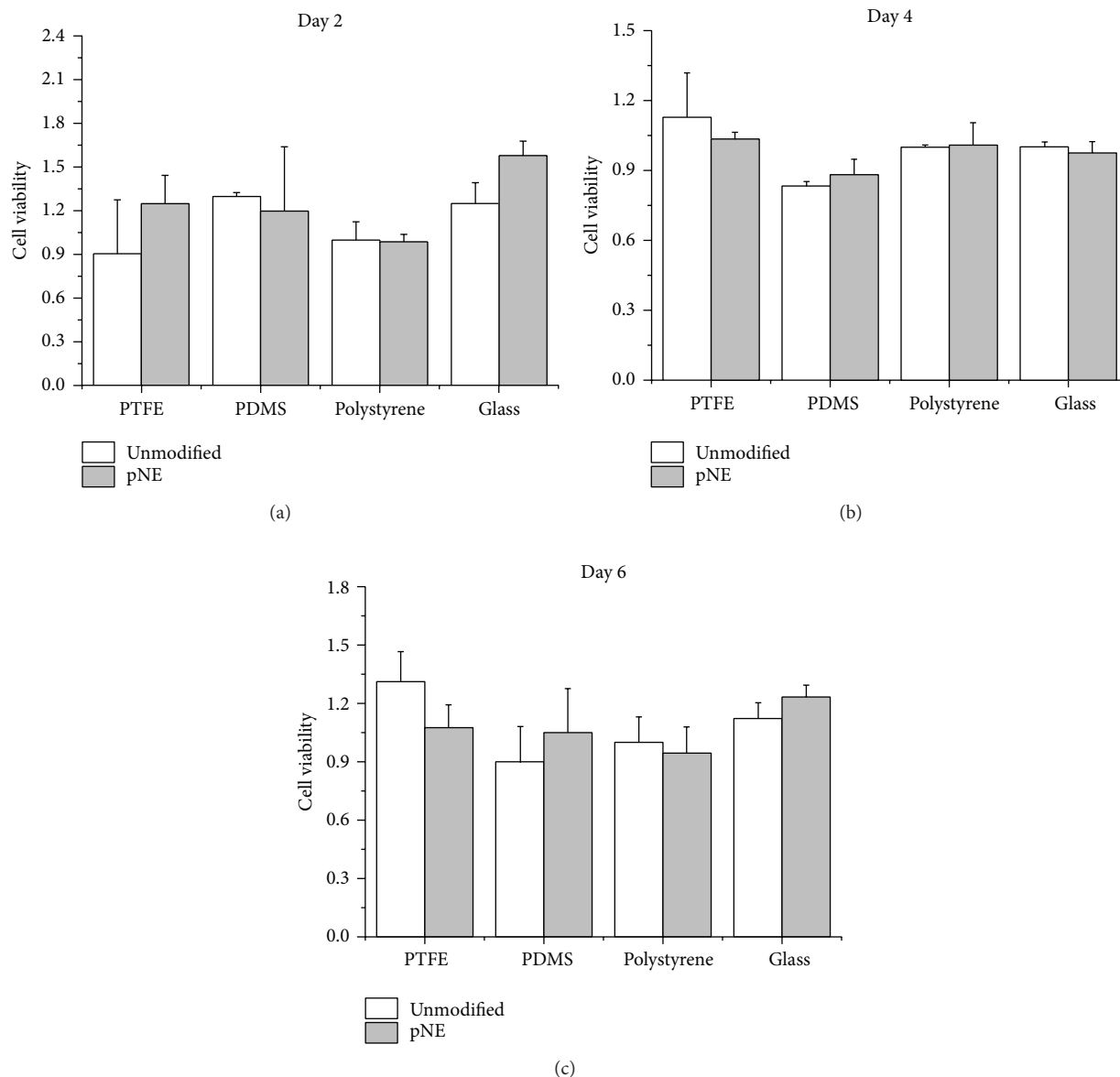


FIGURE 3: The cytotoxicity of pNE-functionalized biointerfaces. The metabolic activity of hNSCs grown on pNE interfaces at 2, 4, and 6 days was measured using WST-1 and compared to the unmodified substrates.

to demonstrate the versatility of norepinephrine, which can form interfaces on various types of materials to facilitate cellular adhesion.

The characterization of the pNE-coated surfaces revealed that the polymerization of norepinephrine (NE) in a weak alkaline solution (pH 8.5) on various materials resulted in similar properties of the exterior surfaces, regardless of the substrate type. As demonstrated in Figure 2, coating with the pNE interface allowed various substrates to acquire a similar wettability and surface morphology. Variations in the wettability of each substrate coated with pNE were detected by measuring the water-contact angles on each substrate (Figure 2(a)). Regardless of the substrate properties, the pNE coating dramatically reduced the contact angles of all the substrates, with final values ranging from 22.76° to 39.86°.

The results were originated from the hydrophilic properties of the pNE coating, which had many hydrophilic moieties such as hydroxyl groups and amine groups. Additionally, both digital images and atomic force microscopy (AFM) analyses revealed that the substrates coated with pNE had smooth surface topographies, regardless of the substrate type (Figures 2(b) and 2(c)). Furthermore, the AFM analysis confirmed no large aggregates when each surface was modified with pNE (Figure 2(c)). Table 1 shows the root-mean-square (RMS) roughness values of the pNE interfaces, confirming significant differences from those of the unmodified substrates ($P < 0.001$). All of these pNE surface characterization results indicate its remarkable capability to induce material-independent surface modification with uniform properties.

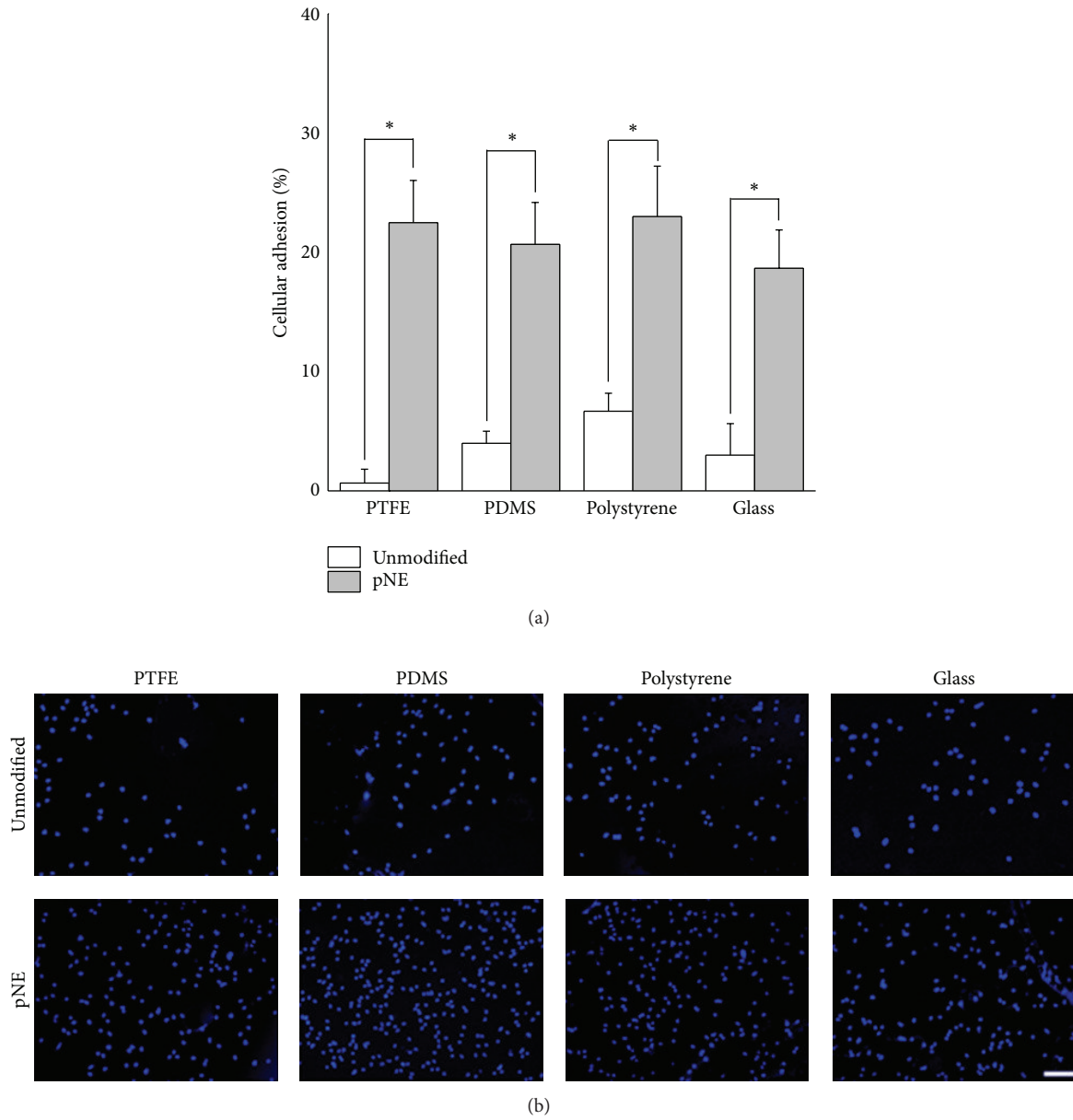
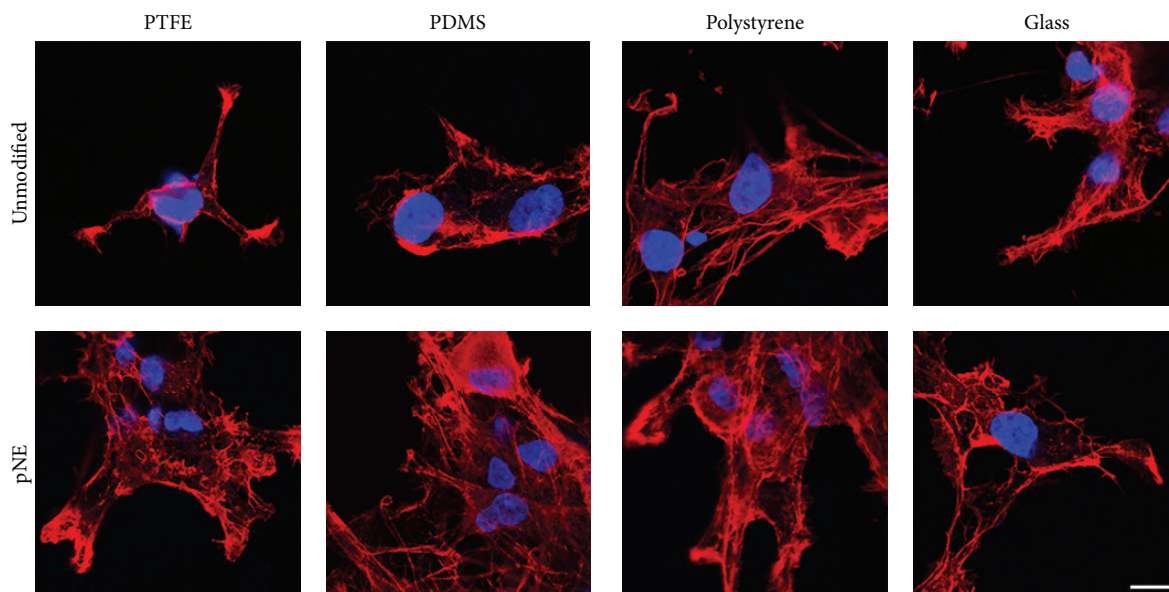


FIGURE 4: Cellular adhesion on pNE interfaces. (a) The percentage of cells was attached to each substrate, indicating the ratio of the number of cells remaining on each substrate to the initial number prior to seeding. To quantify the cell number, hNSCs were rinsed twice with PBS after 2 hours of culture and trypsinized; the cell number was manually counted using a hemocytometer. The symbol * indicates a significant difference compared to each ($P < 0.005$). (b) Fluorescence images of hNSCs were adhered to each substrate. After 2 hours of culture, hNSCs were rinsed twice with PBS, and the nuclei were stained with DAPI to visualize the cells on each substrate. The scale bar indicates 10 micrometers.

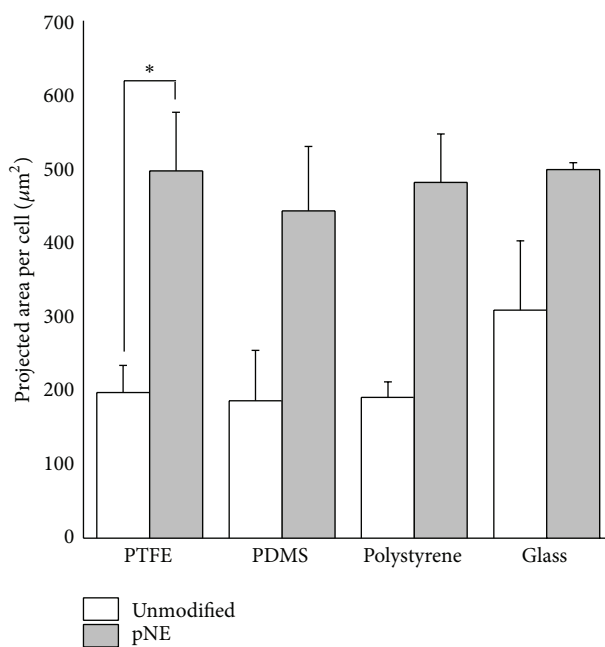
TABLE 1: RMS roughness values of pNE-modified surfaces determined by AFM analysis.

	PTFE (nm)	PDMS (nm)	Polystyrene (nm)	Glass (nm)
Unmodified	1.239 ± 0.021	0.091 ± 0.006	0.138 ± 0.011	0.257 ± 0.012
pNE	$3.391 \pm 0.007^*$	$0.687 \pm 0.032^*$	$0.709 \pm 0.054^*$	$1.119 \pm 0.038^*$

The symbol * indicates significant differences compared to each unmodified substrate ($P < 0.001$).



(a)



(b)

FIGURE 5: The projected area of hNSCs grown on each substrate. (a) Fluorescence images of actin filaments were stained with rhodamine-labeled phalloidin after 48 hours of culture. The nuclei of hNSCs were stained with DAPI. The scale bar indicates 10 μm . (b) The total projected areas of the cells were attached to each substrate. Five random images showing actin filaments were acquired, and the total projected areas were quantified using Image J software. The total projected areas were subsequently normalized to the number of cells observed in each image. The symbol * indicates a significant difference compared to the unmodified substrates ($P < 0.005$).

Subsequently, the metabolic activity of hNSCs adhered to each pNE-coated substrate was analyzed to test the potential of pNE to be employed as a biointerface. Interestingly, the unmodified substrates resulted in no significant reduction in cellular viability compared to that of TCP. Additionally, cellular viability on the pNE-coated substrates at 2, 4, and 6 days of culture was comparable to that of cells grown

under normal culture conditions (i.e., cultured on TCP plates) (Figure 3), suggesting the feasibility of the use of pNE interfaces as a cell-culture substrate.

Importantly, the pNE interface on each substrate resulted in the facilitation of cell adhesion (Figure 4). To evaluate the capability of the pNE-coated surfaces to promote cellular attachment, the cells seeded on each substrate were rinsed

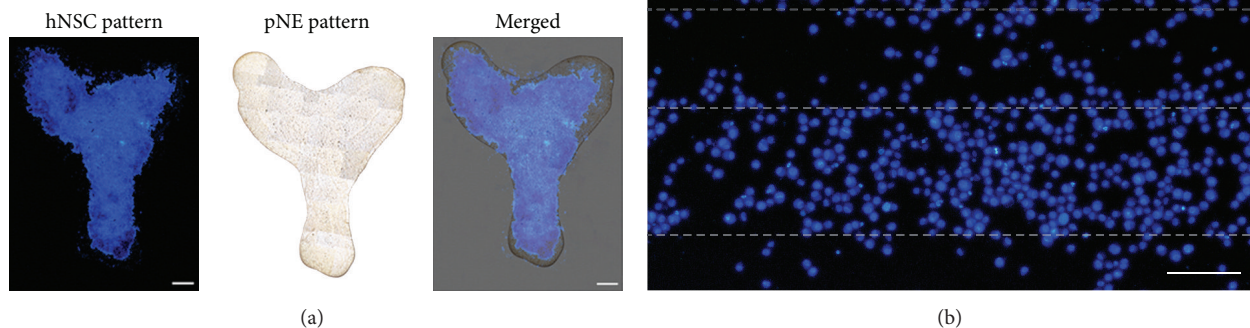


FIGURE 6: Cellular patterns created using pNE interfaces. (a) Macroscale cellular patterns were created using a micropipette. The “Y” shape of the pNE interfaces was generated with a pipette, and hNSCs were seeded onto the entire TCP substrate. After 2 hours of culture, the loose cells were removed by rinsing with PBS, and the adherent cells were stained with Hoechst dye and imaged using fluorescence microscopy. To visualize the entire cellular pattern, individual images were collected and combined to obtain the entire image. The scale bar indicates 1 mm. (b) Microscale cellular patterns were created with a PDMS stamp. The PDMS stamp was immersed in pNE solution and placed on a TCP plate. The substrate was rinsed with PBS; the cells were seeded onto the entire substrate, rinsed with PBS after 2 hours of culture, and imaged. The nuclei were stained using Hoechst dye. The scale bar indicates 100 micrometers.

twice with PBS after only 2 hours of culture. To measure the enhancement of cellular attachment precisely, the cells remaining on each substrate were trypsinized again and manually counted using a hemocytometer (Figure 4(a)), and the nuclei of the cells remaining on each substrate after rinsing with PBS were visualized (Figure 4(b)). The surface modification with pNE resulted in at least a fourfold enhancement in cellular adherence (20–25%) relative to the unmodified naïve material (less than 5%) ($P < 0.005$), even after the short exposure of the cells to the sticky surface. The ultrasmooth surface caused by the pNE coating might distribute sticky moieties homogeneously throughout the entire surface, thereby potentially causing further intimate interactions with a variety of receptors or proteins residing on the cellular membrane for robust cellular adhesion.

Although the pNE coating substantially increased the surface wettability, the pNE interfaces exhibited enhanced adherent properties. The preferred surface wettability for effective cellular attachment has been reported to be static contact angles ranging from 40° to 70° [26]. Also, the reasons explaining the enhanced hNSC adhesion are that the pNE-coated surface is abundant in amine groups, which was demonstrated to facilitate stem cell adhesion, for example, polyD-lysine. Another mechanism might be covalent bond formation between cell-surface proteins and pNE. The redox properties of catechol groups in pNE allow protein/peptide/oligonucleotide covalent conjugations [22, 27, 28].

The enhanced interactions of the cellular membrane with the pNE-modified surfaces led to increases in the projected area of adherent cells (Figure 5). The actin filaments were stained with rhodamine-labeled phalloidin (Figure 5(a)), and the total spreading areas of the cells were subsequently

normalized to the total cell number (Figure 5(b)). Regardless of the substrate type, the hNSCs adhering to the pNE interfaces exhibited an approximately 1.5- to 6-fold increase in spreading areas per cell compared to the unmodified substrates (Figure 5(b)). Interestingly, marked increases in the projected area per cell adhering to the pNE-coated substrate were observed for the hydrophobic surfaces (i.e., PTFE and PDMS) compared to the unmodified surfaces. The well-stretched actin filaments of cells adhering to pNE interfaces may result from increased surface hydrophilicity [29]. Catecholamine compounds can interact with a variety of proteins or moieties to induce cellular attachment and can subsequently protect cell-surface proteins from the denaturation that can occur upon contact with substrates [29]. The improved stability of the proteins or ligands that have a key role in surface interactions might promote cellular adhesion onto pNE-coated surfaces. Additionally, previous studies have demonstrated that the enhancement of cellular adhesion can alter cytoskeletal development, thereby resulting in increased cell spreading [29, 30]. This evidence further supports the notion that modulating the cellular microenvironment by manipulating the surface properties of substrates can be critical for elucidating a variety of cellular events, including adhesion, patterning, and proliferation.

The adhesive property of the pNE interfaces enabled the creation of sticky surfaces onto which cells could adhere in a well-defined pattern (Figure 6). Simply drawing the pNE interface with a micropipette followed by cells incubation for 2 hours generated well-defined cellular patterns corresponding to the preformed pNE patterns on a macroscale (Figure 6(a)). The resolution of these cellular patterns was improved using PDMS stamps with straight-line ridges. As shown in Figure 6(b), well-patterned edges between the

pNE interfaces and nonmodified surfaces were observed, and hNSCs specifically adhered to the pNE patterns. The capability of the pNE interfaces to induce spatial cellular patterns demonstrates their potential as a powerful substrate that can be utilized in tissue engineering applications that require directional cellular growth, such as spinal cord regeneration.

4. Conclusions

A simple and facile interface modification strategy to enhance hNSC adhesion and its viability was examined in this study. The surface-modification method is inspired by the neurotransmitter NE, which is oxidatively polymerized in an alkaline solution to generate pNE. pNE becomes an adherent nanolayer during polymerization, resulting in the functionalization of various material surfaces. The pNE interfaces exhibited superior performances in promoting the cellular adhesion of hNSCs, which are recognized as relatively nonadherent primary cells on typical tissue culture plates. The adhered hNSCs exhibited good viability and spreading on these surfaces. Importantly, the adhesive properties of the pNE interfaces led to well-defined patterns of cellular attachment, thereby demonstrating the ability of the cells to organize into micropatterns. Evaluation of the pNE interfaces as a powerful platform to modulate stem cell fates (e.g., proliferation or differentiation) is highly required to be further studied. All of these data indicate that this pNE coating can be a powerful tool to broaden the range of material choices for the ex vivo expansion of hNSCs, an important goal for cell therapy.

Conflict of Interests

The authors declare that there is no conflict of interests regarding the publication of this paper.

Acknowledgments

This work was supported by the National Research Foundation of Korea (NRF) Grant through the Active Polymer Center for Pattern Integration (no. 2007-0056091, Jae-Hyung Jang), Basic Science Research Program (2012R1A1A1003397, Jae-Hyung Jang), and Biomedical Technology Development Program (2012-0006085, Haeshin Lee) funded by the Ministry of Science, ICT & Future Planning (MSIP).

References

- [1] M. D. Mager, V. Lapointe, and M. M. Stevens, "Exploring and exploiting chemistry at the cell surface," *Nature Chemistry*, vol. 3, no. 8, pp. 582–589, 2011.
- [2] A. E. Nel, L. Mädler, D. Velegol et al., "Understanding biophysicochemical interactions at the nano-bio interface," *Nature Materials*, vol. 8, no. 7, pp. 543–557, 2009.
- [3] M. M. Stevens and J. H. George, "Exploring and engineering the cell surface interface," *Science*, vol. 310, no. 5751, pp. 1135–1138, 2005.
- [4] J. Y. Lim and H. J. Donahue, "Cell sensing and response to micro- and nanostructured surfaces produced by chemical and topographic patterning," *Tissue Engineering*, vol. 13, no. 8, pp. 1879–1891, 2007.
- [5] U. Hersel, C. Dahmen, and H. Kessler, "RGD modified polymers: biomaterials for stimulated cell adhesion and beyond," *Biomaterials*, vol. 24, no. 24, pp. 4385–4415, 2003.
- [6] L. Kam, W. Shain, J. N. Turner, and R. Bizios, "Selective adhesion of astrocytes to surfaces modified with immobilized peptides," *Biomaterials*, vol. 23, no. 2, pp. 511–515, 2002.
- [7] Z. Ma, C. Gao, Y. Gong, and J. Shen, "Cartilage tissue engineering PLLA scaffold with surface immobilized collagen and basic fibroblast growth factor," *Biomaterials*, vol. 26, no. 11, pp. 1253–1259, 2005.
- [8] L. Richert, F. Boulmedais, P. Lavalle et al., "Improvement of stability and cell adhesion properties of polyelectrolyte multilayer films by chemical cross-linking," *Biomacromolecules*, vol. 5, no. 2, pp. 284–294, 2004.
- [9] H. Lee, S. M. Dellatore, W. M. Miller, and P. B. Messersmith, "Mussel-inspired surface chemistry for multifunctional coatings," *Science*, vol. 318, no. 5849, pp. 426–430, 2007.
- [10] K. Y. Suh, J. Seong, A. Khademhosseini, P. E. Laibinis, and R. Langer, "A simple soft lithographic route to fabrication of poly(ethylene glycol) microstructures for protein and cell patterning," *Biomaterials*, vol. 25, no. 3, pp. 557–563, 2004.
- [11] S. M. Kang, I. You, W. K. Cho et al., "One-step modification of superhydrophobic surfaces by a mussel-inspired polymer coating," *Angewandte Chemie—International Edition*, vol. 49, no. 49, pp. 9401–9404, 2010.
- [12] E. Kim, I. T. Song, S. Lee, J. S. Kim, H. Lee, and J. H. Jang, "Drawing sticky adeno-associated viruses on surfaces for spatially patterned gene expression," *Angewandte Chemie—International Edition*, vol. 51, no. 23, pp. 5598–5601, 2012.
- [13] M. Yamato, C. Konno, M. Utsumi, A. Kikuchi, and T. Okano, "Thermally responsive polymer-grafted surfaces facilitate patterned cell seeding and co-culture," *Biomaterials*, vol. 23, no. 2, pp. 561–567, 2002.
- [14] S. Wang, H. Wang, J. Jiao et al., "Three-dimensional nanostructured substrates toward efficient capture of circulating tumor cells," *Angewandte Chemie—International Edition*, vol. 48, no. 47, pp. 8970–8973, 2009.
- [15] L. Heng, R. Hu, S. Chen, M. Li, L. Jiang, and B. Z. Tang, "Ordered honeycomb structural interfaces for anticancer cells growth," *Langmuir*, vol. 29, no. 48, pp. 14947–14953, 2013.
- [16] X. C. Liu, C. Li, H. Liu et al., "Bio-inspired soft polystyrene nanotube substrate for rapid and highly efficient breast cancer-cell capture," *NPG Asia Materials*, vol. 5, p. e63, 2013.
- [17] S. H. Ku, J. S. Lee, and C. B. Park, "Spatial control of cell adhesion and patterning through mussel-inspired surface modification by polydopamine," *Langmuir*, vol. 26, no. 19, pp. 15104–15108, 2010.
- [18] H. Lee, J. Rho, and P. B. Messersmith, "Facile conjugation of biomolecules onto surfaces via mussel adhesive protein inspired coatings," *Advanced Materials*, vol. 21, no. 4, pp. 431–434, 2009.
- [19] S. M. Kang, N. S. Hwang, J. Yeom et al., "One-step multipurpose surface functionalization by adhesive catecholamine," *Advanced Functional Materials*, vol. 22, no. 14, pp. 2949–2955, 2012.
- [20] J. H. Waite, "Surface chemistry: mussel power," *Nature Materials*, vol. 7, no. 1, pp. 8–9, 2008.

- [21] C. R. Nuttelman, D. J. Mortisen, S. M. Henry, and K. S. Anseth, "Attachment of fibronectin to poly(vinyl alcohol) hydrogels promotes NIH3T3 cell adhesion, proliferation, and migration," *Journal of Biomedical Materials Research*, vol. 57, no. 2, pp. 217–223, 2001.
- [22] M. K. Sung, J. Rho, I. S. Choi, P. B. Messersmith, and H. Lee, "Norepinephrine: material-independent, multifunctional surface modification reagent," *Journal of the American Chemical Society*, vol. 131, no. 37, pp. 13224–13225, 2009.
- [23] S. M. Kang and H. Lee, "Surface Modification of Highly Ordered Pyrolytic Graphite (HOPG) by a mussel-inspired Poly(norepinephrine) coating: characterizations and cell adhesion test," *Bulletin of the Korean Chemical Society*, vol. 34, no. 3, pp. 960–962, 2013.
- [24] S. Hong, J. Kim, Y. S. Na et al., "Poly(norepinephrine): ultrasmooth material-independent surface chemistry and nanodepot for nitric oxide," *Angewandte Chemie—International Edition*, vol. 52, no. 35, pp. 9187–9191, 2013.
- [25] H.-T. Kim, I.-S. Kim, I.-S. Lee, J.-P. Lee, E. Y. Snyder, and K. I. Park, "Human neurospheres derived from the fetal central nervous system are regionally and temporally specified but are not committed," *Experimental Neurology*, vol. 199, no. 1, pp. 222–235, 2006.
- [26] Y. Arima and H. Iwata, "Effect of wettability and surface functional groups on protein adsorption and cell adhesion using well-defined mixed self-assembled monolayers," *Biomaterials*, vol. 28, no. 20, pp. 3074–3082, 2007.
- [27] K. Yang, J. S. Lee, J. Kim et al., "Polydopamine-mediated surface modification of scaffold materials for human neural stem cell engineering," *Biomaterials*, vol. 33, no. 29, pp. 6952–6964, 2012.
- [28] H. O. Ham, Z. Liu, K. H. A. Lau, H. Lee, and P. B. Messersmith, "Facile DNA immobilization on surfaces through a catecholamine polymer," *Angewandte Chemie—International Edition*, vol. 123, no. 3, pp. 758–762, 2011.
- [29] S. H. Ku, J. Ryu, S. K. Hong, H. Lee, and C. B. Park, "General functionalization route for cell adhesion on non-wetting surfaces," *Biomaterials*, vol. 31, no. 9, pp. 2535–2541, 2010.
- [30] K. Anselme, "Osteoblast adhesion on biomaterials," *Biomaterials*, vol. 21, no. 7, pp. 667–681, 2000.

Research Article

Preparation of Amino-Modified PAN Fibers with Triethylenetetramine as Aminating Reagents and Their Application in CO₂ Adsorption

Wenbo Zhao,¹ Biao Liu,¹ and Jian Chen²

¹ Faculty of Chemical Engineering, Kunming University of Science and Technology, Kunming 650500, China

² State Key Laboratory of Chemical Engineering, Department of Chemical Engineering, Tsinghua University, Beijing 100084, China

Correspondence should be addressed to Wenbo Zhao; wenshuixing@126.com and Jian Chen; cj-dce@mail.tsinghua.edu.cn

Received 26 December 2013; Revised 1 March 2014; Accepted 3 March 2014; Published 1 April 2014

Academic Editor: Yongping Hou

Copyright © 2014 Wenbo Zhao et al. This is an open access article distributed under the Creative Commons Attribution License, which permits unrestricted use, distribution, and reproduction in any medium, provided the original work is properly cited.

Amino-modified polyacrylonitrile (AMPAN) fiber was synthesized by the reaction of polyacrylonitrile (PAN) fiber and triethylenetetramine (TETA) in the presence of water. The effect of water amount, reaction temperature, and time on the weight increase degree and alkali content of the AMPAN fiber was investigated in detail. The characterization results indicated that TETA could be grafted onto the surface of PAN fiber by this method. However, the highest adsorption capacity of the AMPAN fibers was only 0.09 g/g even at 15 bar and 50°C, which was much lower than the porous materials. The reason for this result may be related to its low surface area.

1. Introduction

With the development of society and increase of live level, which mainly come from the combustion of fossil fuel and human activities, the excess emission of CO₂ has become a worldwide problem. The research of CO₂ capture attracted attention of world scientists in recent years [1–3]. At present, the CO₂ capture technology could be divided into three major processes: postcombustion, precombustion, and oxy-fuel combustion; among them, postcombustion is the best development technology for its favorable inheritance and extensive adaptability [4, 5]. For the CO₂ separation and capture of postcombustion technology, there are four possible methods: absorption with solution [6], adsorption with solid material [7], membrane diffusion [8], and cryogenic process [9]; among them, adsorption was considered to be promising because of its low energy consumption, low equipment cost, and easiness to be applied [10]. The key to this method is to discover or design an adsorption material with high CO₂ adsorption capacity and that is regenerable under mild condition.

A lot of materials have been tested in the research of CO₂ adsorption. Porous material, such as zeolite and activity

carbon, was investigated most extensively. However, the selectivity and adsorption capacity of CO₂ on these materials are not high. At present, amino-modified porous materials gradually become the research focus since it has some advantages of liquid amine, which was used in the industrial absorption process. MCM-41 [11–13], SBA-15 [14], SBA-16 [15], activated carbon [16], and anthracites [17] all have been used as supports. The amines to modify supports contain polyethylenimine (PEI), diethylenetriamine, pentaethylenhexamine, aminopropyl triethoxysilane, and so on. The main modification methods are impregnation and grafting. Recently, some fibrous CO₂ adsorbents modified with amino were reported in the literature for they have the advantage of high surface area, low price, and convenience in use. In these works, PEI was bonded to glass fiber with epoxy resin or epichlorohydrin as cross-linking agents; the highest capacity is 2.03 mmol CO₂/g and 4.12 mmol CO₂/g, respectively [18, 19]. However, PEI could leach from adsorbents and reduce the capacity of CO₂. On the other hand, too many PEI on the surface of adsorbents would lead to the formation of PEI multilayers. With the increase of thickness of PEI multilayers, the diffusion of CO₂ became more difficult, which would decrease the utilization efficiency

of PEI. Therefore, the CO₂ adsorption capacity would reach maximum when PEI loading amount reached a certain value. Grafting method of amine may be a better way to introduce monolayer amino onto support compared to physical coating because the reaction is homogenous in microscale. Yang et al. prepared an adsorbent by grafting allylamine onto polyacrylonitrile (PAN) fiber with preirradiation grafting copolymerization method. Its adsorption capacity could reach 6.22 mmol CO₂/g when the grafting degree was 60% [20].

In the present work, another amino-modified PAN (AMPAN) fiber was prepared with grafting method through the reaction of PAN fiber and triethylenetetramine (TETA) solution with the help of water. The product was characterized with FTIR, TG, BET, and EA. Its adsorption capacity of CO₂ was measured by magnetic suspension balance and automatic N₂ adsorption-desorption apparatus under different temperature and pressure.

2. Experimental

2.1. Material and Reagent. PANF was kindly provided by DongFuShengYing Company. TETA was purchased from J&k Company. CO₂ was purchased from Beijing Reagent Company. Deionized water (DI) was used in the whole study.

2.2. Preparation of AMPAN Fiber. In a typical preparation, PAN fiber was firstly extracted with methanol at boil temperature for 24 hours to remove the silicone oil at surface. Then, PAN fiber, TETA, and water (sometimes without water) were put into a glass reaction vessel with a reflux column; the mixture was stirred with a magnetic stirrer and the reaction proceeded at 110–180°C for 2–10 hour. The fibers were separated from the solution after the reaction, washed with DI water till neutral, dried at 50°C in an oven for 10 h, and stored in desiccators prior to use. The materials prepared at different temperatures will be designated as fiber-*T*, where *T* is the synthesis temperature.

2.3. Characterization. Acid exchange capacities of the AMPAN fibers were determined by automatic potential titration instrument. AMPAN fiber (0.200 g) was immersed into 20 mL of 0.100 M/L HCl for 0.5 h. Then, 5 mL solution was fetched out and its HCl concentration was determined by titration with 0.100 M/L NaOH. The exchange capacity was calculated based on the amount of acid consumed. The O content of AMPAN fibers was determined by element analyzer (PerkinElmer PE 2400II). FTIR spectra were recorded on a Fourier transform infrared spectrometer (Nicolet Magna 550) in the region 4000–200 cm⁻¹. The BET surface area of AMPAN fibers was measured at 77.3 K in an automatic N₂ adsorption-desorption apparatus (Quantachrome, Nova 4000). Thermogravimetric analysis (TG) was carried out by a simultaneous thermal analyzer (Netzsch STA 449) at a 5 K/min heating rate up to 473 K under a flow of air.

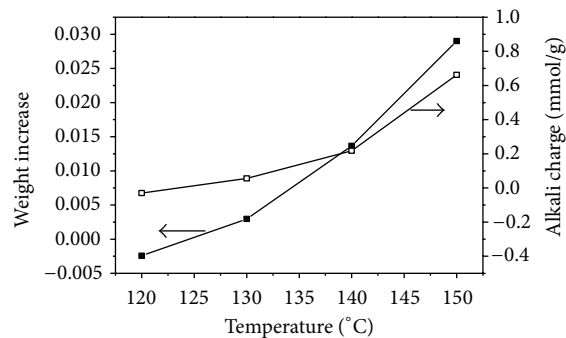


FIGURE 1: Effect of temperature on the weight-gain and alkali content of fiber without water. Reaction condition: 0.04 mol fiber; 0.2 mol TETA; 2 h.

2.4. Adsorption Experiment. The CO₂ adsorption experiments under atmospheric pressure were carried out on the automatic N₂ adsorption-desorption apparatus. At first, about 0.05 g sample was vacuumed for 1 h at 180°C, and then the sample pipe was installed on the equipment. Liquid nitrogen was used to keep the adsorption temperature at 77 K. At last, CO₂ gas was introduced into sample cell; the adsorption capacity was obtained by volumetric method. The CO₂ adsorption experiments above atmospheric pressure were conducted by using magnetic suspension balance (Rubotherm). In an adsorption experiment, about 0.1 g AMPAN fiber was pretreated at 180°C for 0.5 h under the flow of N₂ and degassed for 0.5 h in vacuum. Then, the CO₂ gas was introduced into sample cell with a flow rate of 50 mL/min for 0.5 h. The weight variation of fiber in this process was recorded by the balance.

3. Results and Discussion

3.1. Preparation of Fibers

3.1.1. Effect of Water Amount on the Weight Increase Degree and Alkali Content of Fiber. The weight increase degree of the PAN fiber is an important index of amino grafting degree, which would increase the alkali content of the fiber. Without water, the amino grafting degree was very low. As shown in Figure 1, the weight and alkali content of fibers increased with the improvement of temperature. However, the highest weight increase degree was less than 3.0% at the highest temperature 150°C; the corresponding alkali content was only about 0.7 mmol/g.

Under the reaction condition of 40 mmol PAN fiber and 200 mmol TETA at 150°C for 2 h, with the increase of water amount from 0 to 14.4 g, the weight of fiber increased from 2.9% to 48.8% firstly and then reduced to 19.3% and at last to 3.8% (see Figure 2). The alkali content variation characterization of the prepared AMPAN fiber was consistent with the weight variation characterization. It increased from 0.7 to 3.1 mmol/g and then reduced to 2.2 and at last to 0.2 mmol/g. The reason for the decrease of weight and alkali content was that the excess water would decrease the reaction temperature of solution despite the fact that the temperature

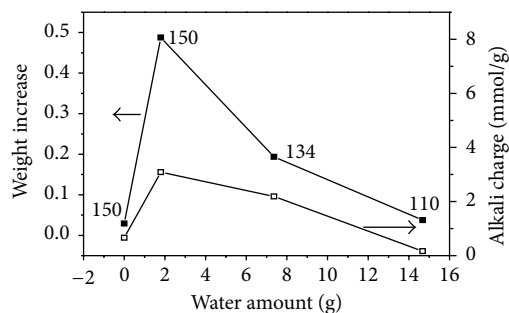


FIGURE 2: Effect of water amount on the weight increase degree and alkali content of fiber. Reaction condition: 0.04 mol fiber; 0.2 mol TETA; 150°C; 2 h.

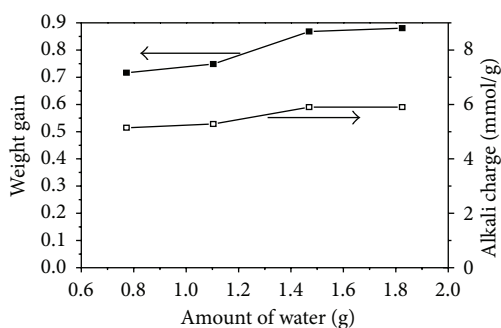


FIGURE 3: Effect of water amount on the weight increase degree and alkali content of fiber. Reaction condition: 0.04 mol fiber; 0.2 mol TETA; 160°C; 2 h.

of oil bath was the same. It was observed that the temperature of reaction solution was 150°C when the water amount was 1.8 g or without water, while the reaction temperature was only 134 and 110°C when the water amount was 7.2 g and 14.4 g, respectively, although the oil bath temperature was still 150°C.

Under the same reaction temperature, the effect of water amount on the weight increase degree was further investigated. As shown in Figure 3, with the amount of water increased from 0.72 to 1.80 g, the weight of fiber increased from 72% to 88%. The alkali content of the fiber also increased from 5.1 to 5.9 mmol/g. This phenomenon could be explained by Le Chatelier's principle: the yield of product would increase along with the increase of reactant concentration.

3.1.2. Effect of Reaction Temperature. The effect of reaction temperature on the weight increase degree and alkali content was investigated under the following conditions: 0.04 mol fiber; 0.2 mol TETA; 0.1 mol water; 2 h. The results indicated that the weight of fiber increased monotonously from 49% to 150% with the improvement of temperature from 150 to 180°C (see Figure 4). At the same time, the alkali content of fiber increased from 3.1 to 6.6 mmol/g. However, once the temperature was over 220°C, the fiber would dissolve into the TETA solution. There are two possible reasons for the phenomenon: (1) TETA was grafted on the surface of PAN fiber by the reaction, which enhances the mutual effect

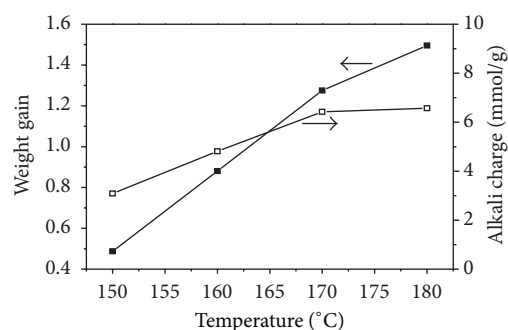


FIGURE 4: Effect of temperature on the weight increase degree and alkali content of fiber. Reaction condition: 0.04 mol fiber; 0.2 mol TETA; 0.1 mol water; 2 h.

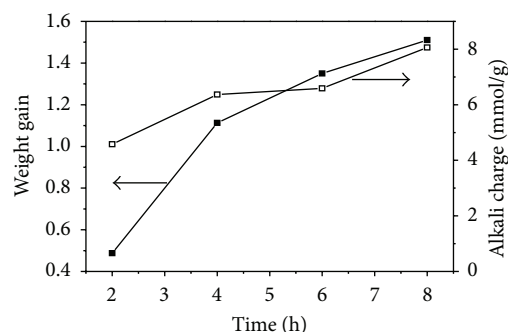


FIGURE 5: Effect of time on the weight increase degree and alkali content of fiber. Reaction condition: 0.04 mol fiber; 0.2 mol TETA; 0.1 mol water; 150°C.

between AMPAN fiber and solvent TETA through hydrogen-bond interaction; (2) the carbon-carbon bond of PAN fiber would be broken at high temperature.

3.1.3. Effect of Reaction Time. The effect of reaction time on the weight increase degree and alkali content was investigated under the following conditions: 0.04 mol fiber; 0.2 mol TETA; 0.1 mol water; 150°C. As shown in Figure 5, with the increase of reaction time from 2 to 8 h, the weight and alkali content of fiber would increase from 49% to 151% and from 4.6 to 8.1 mmol/g, respectively.

3.2. Characterization of Fibers

3.2.1. The Effect of Reaction Condition on the Oxygen Content of AMPAN Fibers. Figure 6 shows the effect of reaction condition on the oxygen content of AMPAN fibers. With the increase of reaction temperature, time, and water amount, the oxygen content of fiber also increased. These results are consistent with the conclusions of previous discussion. The highest oxygen content was 19.8% at 180°C, which indicated that the hydrolysis degree of cyano group was the deepest under this condition.

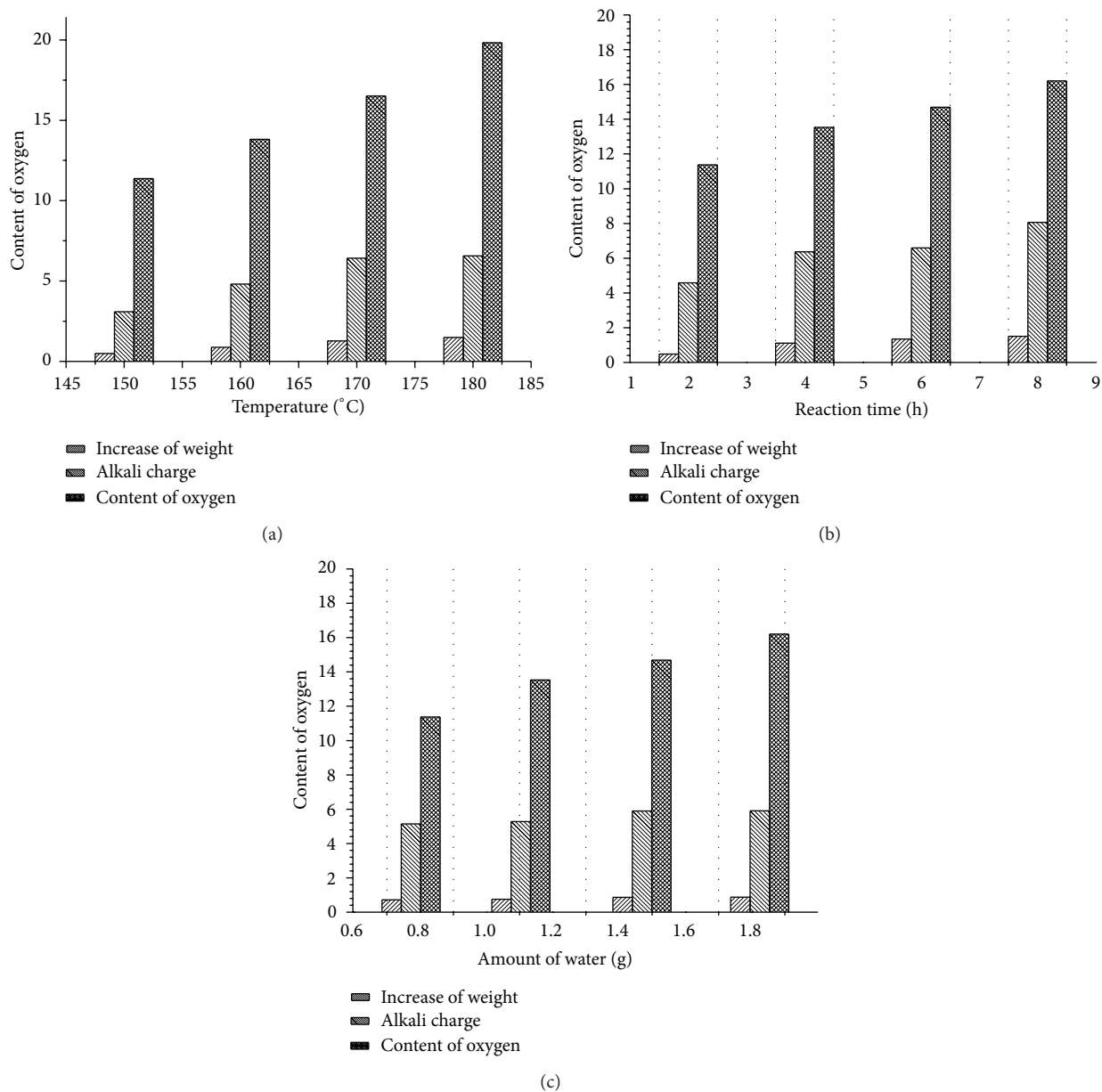


FIGURE 6: Effect of reaction condition on the oxygen content of AMPAN fiber: (a) temperature; (b) time; (c) amount of water.

3.2.2. FTIR Spectrum of Fibers. Figure 7 shows the FTIR spectra of PAN fiber and AMPAN fiber. The band in the spectrum of PAN fiber could be assigned as follows: 2945 cm^{-1} was the stretching vibration of CH , CH_2 , and CH_3 ; 2244 cm^{-1} was the stretching vibration of CN ; 1455 cm^{-1} was the bending stretching vibration of CH_2 and CH_3 . After reaction with TETA at different temperatures, some new peaks appeared in the spectrum of prepared AMPAN fiber: the band at 2840 cm^{-1} was the symmetry stretching vibration of CH_2 and the band at 1668 , 1558 , and 1120 cm^{-1} was the $\text{C}=\text{O}$ stretching vibration, $\text{N}-\text{H}$ bending vibration, and $\text{C}-\text{N}$ bending vibration in imide, respectively. At the same time, the band at 2244 cm^{-1} reduced more and more significantly with

the increase of temperature from 150 to 180°C . These results indicated that imide group was introduced to the surface of PAN fiber. The reaction mechanism in the preparation of AMPAN fiber from PAN fiber and TETA could be expressed by Scheme 1.

3.2.3. TG Analysis of Fibers. The TGA spectra of AMPAN fibers prepared under different temperature was presented in Figure 8. The mass loss profiles are similar for all the AMPAN fibers. In the TG curves, two weight loss steps were observed at 85 and 160°C . The first weight loss could be attributed to desorption of the moisture. The second one may be assigned to desorption of CO_2 , which were adsorbed in the previous

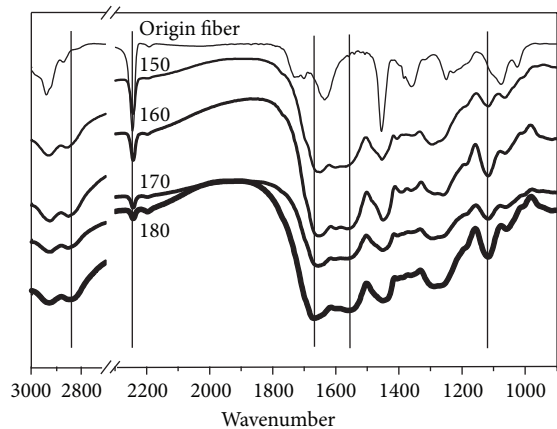


FIGURE 7: FTIR spectrum of fiber prepared at different temperatures.

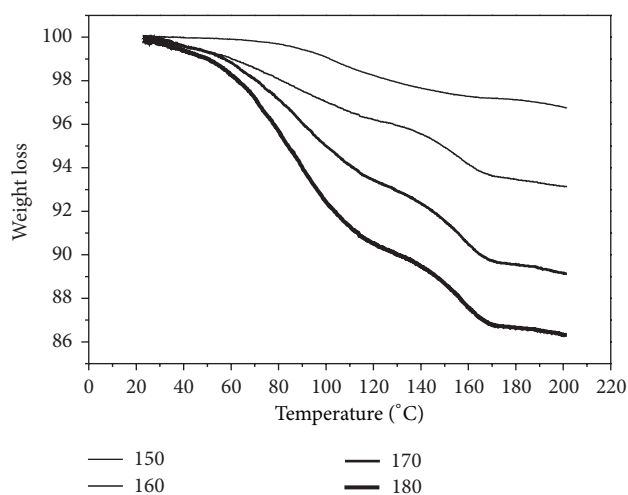
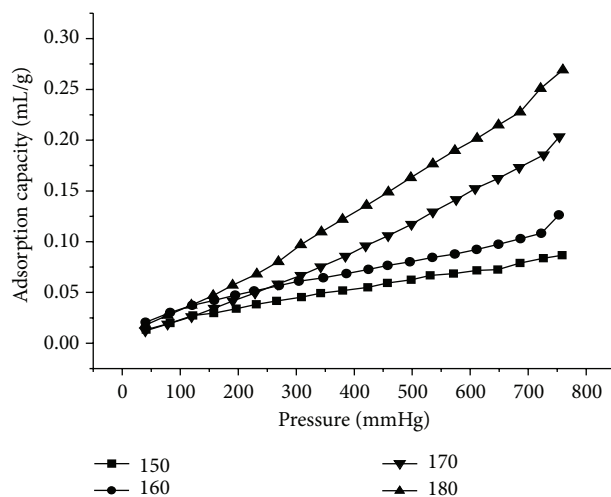


FIGURE 8: TG analysis of fiber prepared at different temperatures.

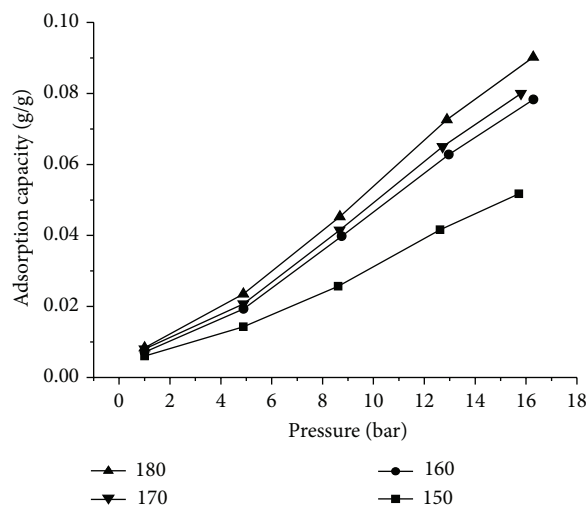
preparation process of AMPAN fiber. The highest weight loss was observed to be 14% for the fiber prepared at 180°C.

3.2.4. Surface Area of Fiber. The specific surface area of AMPAN fibers was determined by Brunauer-Emmett-Teller (BET) method based on N_2 adsorption isotherm at 77 K. The results were presented in Table 1. It was found that the surface area of fibers increased monotonously from 0.878 to 1.238 m^2/g , with the increase of preparing temperature from 150 to 180°C. These results indicate that reaction temperature did not affect the surface area of fiber significantly; they are all small.

3.3. Adsorption Property of AMPAN Fiber. The adsorption isotherms of CO_2 onto AMPAN fiber prepared at different temperatures were obtained at pressure from 0 to 15 bar. Figure 9(a) shows the CO_2 adsorption data of fiber at 77 K when the pressure is lower than atmospheric pressure. The adsorption capacities of fibers varied according to the following order: fiber-180 > fiber-170 > fiber-160 > fiber-150. The highest capacity was only 0.27 mL/g at atmospheric pressure.



(a)



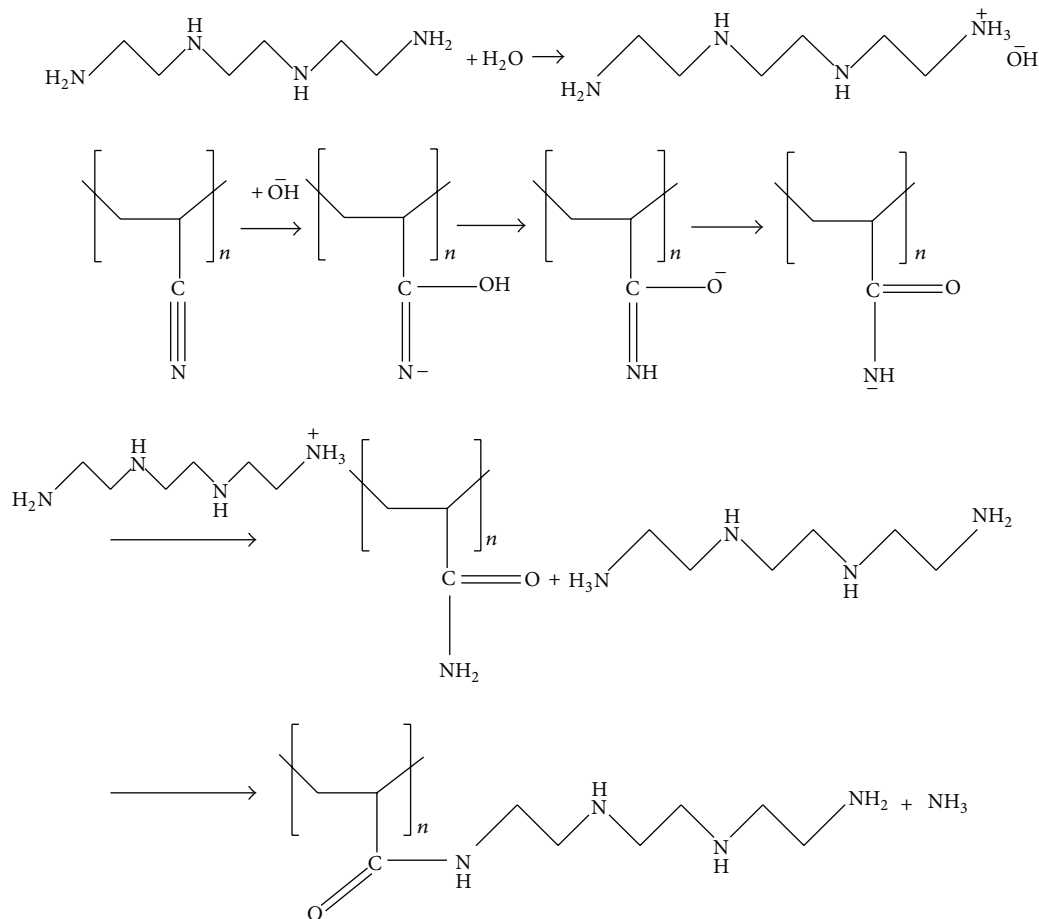
(b)

FIGURE 9: CO_2 adsorption capacity of fiber at different pressure: (a) pressure lower than atmospheric pressure; (b) pressure higher than 1 bar.

Figure 9(b) shows the CO_2 adsorption data of fiber at 50°C above the atmospheric pressure. The capacities of fibers variation characterization are consistent with that obtained under the atmospheric pressure. The highest capacity was 0.09 g/g for fiber 180. These results indicated that the adsorption capacity of AMPAN fiber was much lower than that of PEI and allylamine modified PAN fiber reported previously. The reason may be due to the small surface area of AMPAN fiber. Further research was not conducted for its adsorption capacity which was far from satisfactory.

4. Conclusions

A series of amino-modified PAN fibers were synthesized by the reaction of PAN fiber with TETA in the presence of water. The weight and alkali content, namely, amino grafting degree, would be improved by prolonging reaction time



SCHEME 1: Reaction mechanism of conversion from PAN to AMPAN fiber.

TABLE 1: Surface of AMPAN fiber prepared at different temperatures.

Fiber	Fiber 150°C	Fiber 160°C	Fiber 170°C	Fiber 180°C
Surface area (m^2/g)	0.878	0.976	1.048	1.238

and increasing reaction temperature. However, proper water amount was needed to improve the amino grafting degree, because excess water would reduce the temperature of the reaction solution. The oxygen content analysis and FTIR characterization results indicated that TETA was grafted onto the surface of PAN fiber. TG analysis demonstrated that the fibers would desorb water and CO_2 at about 85 and 160°C, respectively, which were adsorbed in the preparation process. The adsorption capacities of AMPAN fibers were very low, which may be attributed to its low surface area.

Conflict of Interests

The authors declared that they have no conflict of interests to this work.

Acknowledgments

The authors acknowledge the financial support from State Key Laboratory of Chemical Engineering (No. SKL-ChE-12A03) and National Natural Science Foundation of China (Grant No. 21306071).

References

- [1] E. S. Rubin, C. Chen, and A. B. Rao, "Cost and performance of fossil fuel power plants with CO_2 capture and storage," *Energy Policy*, vol. 35, no. 9, pp. 4444–4454, 2007.
- [2] J. C. Abanades, E. S. Rubin, and E. J. Anthony, "Sorbent cost and performance in CO_2 capture systems," *Industrial and Engineering Chemistry Research*, vol. 43, no. 13, pp. 3462–3466, 2004.
- [3] R. Steeneveldt, B. Berger, and T. A. Torp, "CO₂ capture and storage: closing the knowing-doing gap," *Chemical Engineering Research and Design*, vol. 84, no. 9, pp. 739–763, 2006.
- [4] J. Davison, "Performance and costs of power plants with capture and storage of CO_2 ," *Energy*, vol. 32, no. 7, pp. 1163–1176, 2007.
- [5] C. Kunze and H. Spliethoff, "Assessment of oxy-fuel, pre- and post-combustion-based carbon capture for future IGCC plants," *Applied Energy*, vol. 94, pp. 109–116, 2012.

- [6] M. Hasib-ur-Rahman, M. Sijaj, and F. Larachi, "Ionic liquids for CO₂ capture—development and progress," *Chemical Engineering and Processing: Process Intensification*, vol. 49, no. 4, pp. 313–322, 2010.
- [7] S. Araki, H. Doi, Y. Sano, S. Tanaka, and Y. Miyake, "Preparation and CO₂ adsorption properties of aminopropyl-functionalized mesoporous silica microspheres," *Journal of Colloid and Interface Science*, vol. 339, no. 2, pp. 382–389, 2009.
- [8] A. Brunetti, F. Scura, G. Barbieri, and E. Drioli, "Membrane technologies for CO₂ separation," *Journal of Membrane Science*, vol. 359, no. 1-2, pp. 115–125, 2010.
- [9] K. E. Zanganeh, A. Shafeen, and C. Salvador, "CO₂ capture and development of an advanced pilot-scale cryogenic separation and compression unit," *Energy Procedia*, vol. 1, pp. 247–252, 2009.
- [10] S. Choi, J. H. Drese, and C. W. Jones, "Adsorbent materials for carbon dioxide capture from large anthropogenic point sources," *ChemSusChem*, vol. 2, no. 9, pp. 796–854, 2009.
- [11] X. Xu, C. Song, B. G. Miller, and A. W. Scaroni, "Adsorption separation of carbon dioxide from flue gas of natural gas-fired boiler by a novel nanoporous "molecular basket" adsorbent," *Fuel Processing Technology*, vol. 86, no. 14-15, pp. 1457–1472, 2005.
- [12] X. Xu, C. Song, J. M. Andresen, B. G. Miller, and A. W. Scaroni, "Novel polyethylenimine-modified mesoporous molecular sieve of MCM-41 type as high-capacity adsorbent for CO₂ capture," *Energy and Fuels*, vol. 16, no. 6, pp. 1463–1469, 2002.
- [13] X. Xu, C. Song, J. M. Andrésen, B. G. Miller, and A. W. Scaroni, "Preparation and characterization of novel CO₂ "molecular basket" adsorbents based on polymer-modified mesoporous molecular sieve MCM-41," *Microporous and Mesoporous Materials*, vol. 62, no. 1-2, pp. 29–45, 2003.
- [14] H. Zhao, J. Hu, J. Wang, L. Zhou, and H. Liu, "CO₂ capture by the amine-modified mesoporous materials," *Acta Physico-Chimica Sinica*, vol. 23, no. 6, pp. 801–806, 2007.
- [15] C. Knöfel, J. Descarpentries, A. Benzaouia et al., "Functionalised micro-/mesoporous silica for the adsorption of carbon dioxide," *Microporous and Mesoporous Materials*, vol. 99, no. 1-2, pp. 79–85, 2007.
- [16] M. G. Plaza, C. Pevida, A. Arenillas, F. Rubiera, and J. J. Pis, "CO₂ capture by adsorption with nitrogen enriched carbons," *Fuel*, vol. 86, no. 14, pp. 2204–2212, 2007.
- [17] M. M. Maroto-Valer, Z. Tang, and Y. Zhang, "CO₂ capture by activated and impregnated anthracites," *Fuel Processing Technology*, vol. 86, no. 14-15, pp. 1487–1502, 2005.
- [18] P. Li, B. Ge, S. Zhang, S. Chen, Q. Zhang, and Y. Zhao, "CO₂ capture by polyethylenimine-modified fibrous adsorbent," *Langmuir*, vol. 24, no. 13, pp. 6567–6574, 2008.
- [19] P. Li, S. Zhang, S. Chen, Q. Zhang, J. Pan, and B. Ge, "Preparation and adsorption properties of polyethylenimine containing fibrous adsorbent for carbon dioxide capture," *Journal of Applied Polymer Science*, vol. 108, no. 6, pp. 3851–3858, 2008.
- [20] Y. Yang, H. Li, S. Chen, Y. Zhao, and Q. Li, "Preparation and characterization of a solid amine adsorbent for capturing CO₂ by grafting allylamine onto PAN fiber," *Langmuir*, vol. 26, no. 17, pp. 13897–13902, 2010.

Research Article

Variable Responsive Wettability Films via Electrospinning Induced by Solvents

Nü Wang, Fengyun Guo, Jing Wu, Yong Zhao, and Lei Jiang

Key Laboratory of Bioinspired Smart Interfacial Science and Technology of Ministry of Education, Beijing Key Laboratory of Bioinspired Energy Materials and Devices, School of Chemistry and Environment, Beihang University, Beijing 100191, China

Correspondence should be addressed to Nü Wang; wangn@buaa.edu.cn and Yong Zhao; zhaoyong@buaa.edu.cn

Received 2 January 2014; Accepted 22 January 2014; Published 2 March 2014

Academic Editor: Yongping Hou

Copyright © 2014 Nü Wang et al. This is an open access article distributed under the Creative Commons Attribution License, which permits unrestricted use, distribution, and reproduction in any medium, provided the original work is properly cited.

Three kinds of interesting distinct wettability films are fabricated by a facile electrospinning technique. The films are composites of poly(N-isopropylacrylamide) and polystyrene but different precursor solvents. By taking advantage of the conformational changes of poly(N-isopropylacrylamide) chains and polystyrene chains in different solvents, the films exhibit responsive wettability variation to temperature.

1. Introduction

Smart interfacial materials with special wettability have attracted considerable attention in recent years due to their importance for both fundamental research and practical applications [1–4]. Fruitful achievements have been proposed in many areas, for example, superhydrophobic surfaces used for self-cleaning and low-adhesion [5, 6] and superhydrophilic surfaces used for antifouling and biomedical devices [7]. Furthermore, special wettability surfaces that can respond to external environment stimuli (e.g., temperature, light, pH, electrical field, solvent, and magnetic field) [8–13] have been reported through various methods, such as sol-gel method, the plasma method, template method, electrospinning method, surface-initiated atom-transfer radical polymerization, hydrothermal approach, self-assembled monolayers, electrochemical deposition, and layer-by-layer technique [14–20]. Nevertheless, most of the smart surfaces fabricated are still limited to laboratory. With the unceasing in-depth exploration and consideration of these functional materials, it is of particular important to develop a facile method and manufacture on large scale.

Electrospinning has been widely recognized as an efficient and promising technique of preparing polymer micro/nanofibers in recent years [21, 22]. Researchers found that the structure and property of electrospinning fibers

can be influenced by many factors, including polymers' solubility, molecular weight, solvent, the solution properties (e.g., viscosity, elasticity, conductivity, and surface tension), and ambient parameters (e.g., temperature, humidity, and air velocity) [23–27], while it is well known that the solvent is an important factor affecting the morphology of fibers. Examples include that Megelski et al. investigated the influence of different polymer/solvent systems on the fiber micro-/nanoporous surface morphology [24]. As far as mentioned above, many researches have been interested in the influence of polymer/solvent on the fiber surface morphology in the process of electrospinning; few people pay attention to the property of the fiber surfaces. In addition, heterogeneous materials are attractive because they may endow new function different to the intrinsic properties of two original materials. Herein, we designed and fabricated poly(N-isopropylacrylamide) (PNIPAAm)/polystyrene (PS) composite films with various wettability via electrospinning by using different precursor solvents. By taking advantages of distinct conformational changes of PNIPAAm chains and PS chains in different solvents, variable responsive wettability films have been successfully realized. The water contact angle (CA) of the PNIPAAm/PS composite films with N,N-dimethylformamide (DMF) or dichloroethene (CH_2Cl_2) precursor solution is completely different. The as-prepared PNIPAAm/PS composite film which is formed from DMF

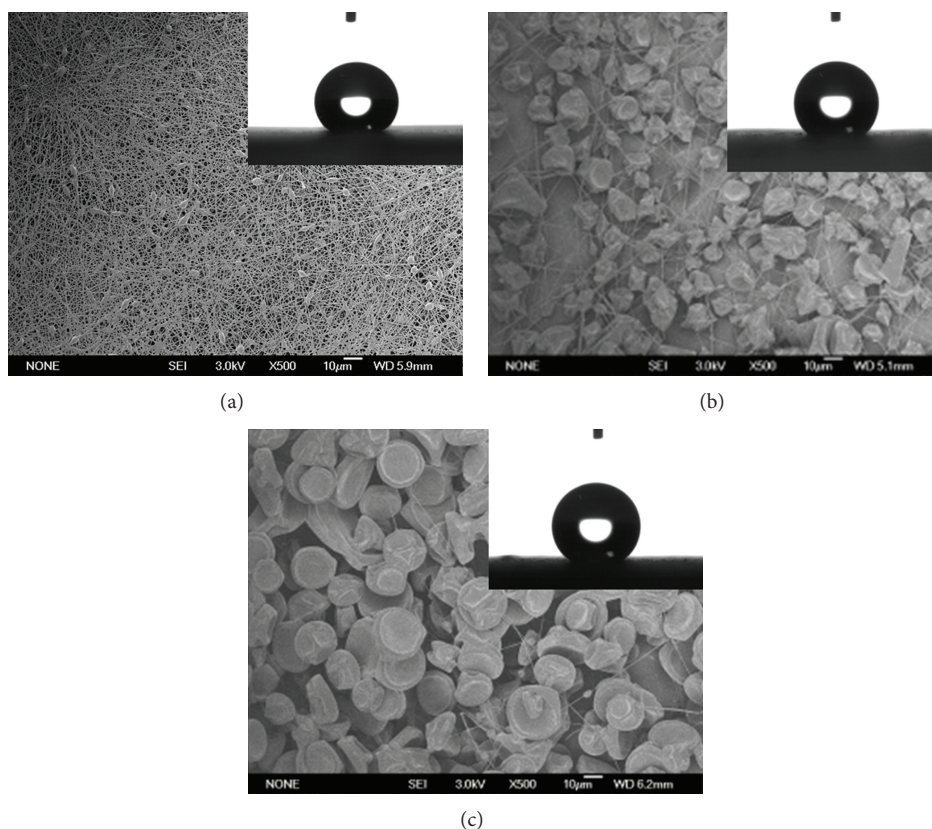


FIGURE 1: Typical SEM images of the PS films prepared by electrospinning. (a), (b), and (c) correspond to films I, II, and III which were fabricated from a 10 wt% solution of PS in DMF, CH_2Cl_2 , and THF, respectively. The insets are photographs of water-droplet shape on the films I, II, and III, respectively.

precursor solution showed superhydrophilicity both before and after increasing temperature. Inversely, the as-prepared PNIPAAm/PS composite film which is formed from CH_2Cl_2 precursor solution showed superhydrophobicity both before and after increasing temperature. Interestingly, in a proper proportion of PNIPAAm and PS, the water CA of the composite films in which the solvent is tetrahydrofuran (THF) in precursor solution could switch between superhydrophobic and superhydrophilic when changing the temperature. Distinct conformation of PNIPAAm chains and PS chains in different precursor solvents results in various wettability via electrospinning. It is important for the transformation of polymeric precursor solution into fibers during the process of electrospinning.

2. Experimental

2.1. Preparation of Polystyrene (PS) Films. PS (homopolymer, $M_w = 230,000$, Aldrich) was dissolved in solvents by stirring for 4 h to form 10 wt% transparent solution. The solvents are DMF, CH_2Cl_2 , and THF (A.R.), respectively, which were purchased from Beijing Yili Fine Chemical Co., Ltd. About 2 mL of the precursor solution was placed in a 5 mL syringe equipped with a blunt metal needle of 0.7 mm inner diameter. The solution feed rate is about 0.5 mL/h. The needle was connected to a high voltage generator, and a grounded metallic plate covered with a sheet of aluminum foil served as

a collecting substrate. The distance between the needle tip and collector was 10–20 cm, and the voltage was set at 15–20 kV.

2.2. Preparation of PNIPAAm/PS Composite Films. Preparation of PNIPAAm/PS composite films was similar to that of PS film. The PNIPAAm (poly(N-isopropylacrylamide), $M_n = 20000\text{--}25000$, Aldrich) and PS were mixed and dissolved in DMF, CH_2Cl_2 , and THF, respectively, and stirred for 4 h. The proportion of PNIPAAm, PS, and solvent is 2:10:90 (PNIPAAm/PS/solvent).

2.3. Characterization. The morphology and structure features of the composite films were characterized by field emission scanning electron microscopy (FE-SEM) (JEOL JSM-6700F) at 3.0 kV. Contact angle was measured on a data-physics OCA20 contact angle system at ambient temperature. The temperature was controlled by a superthermostat (Julabo F25, Germany). Water droplet (about $2\ \mu\text{L}$) was dropped carefully onto the samples. The average CA values were obtained by measuring five different positions of the same sample.

3. Results and Discussion

The PS films were prepared by electrospinning with a variety of PS/solvent solutions. Firstly, we prepared film I from

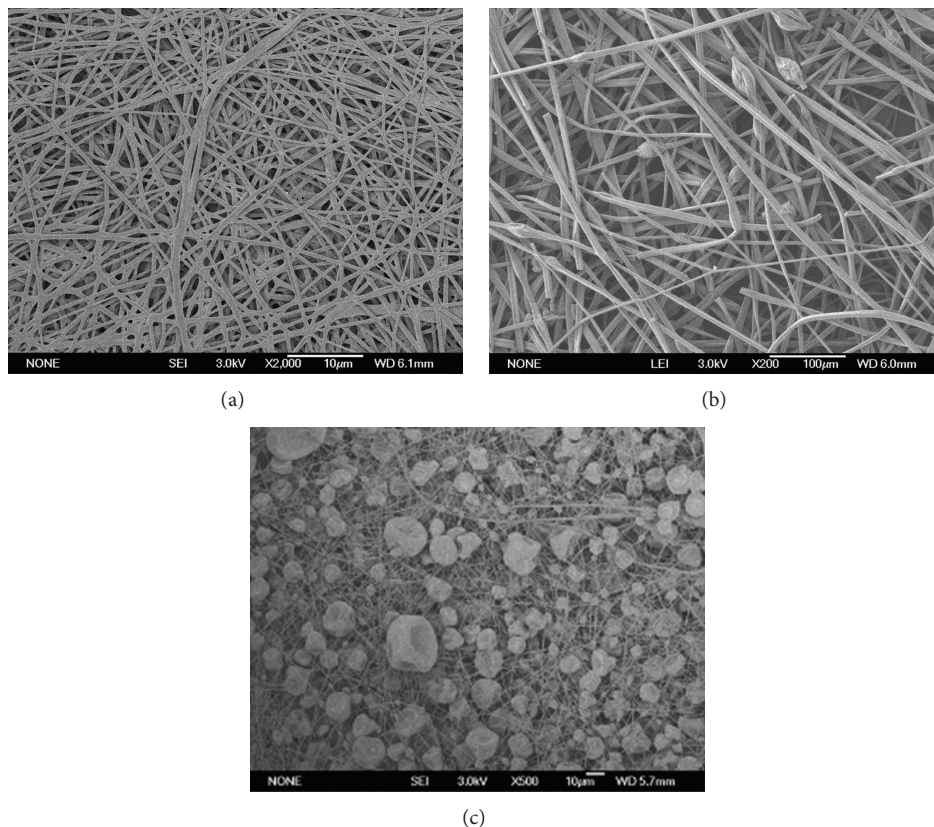


FIGURE 2: Typical SEM images of PNIPAAm/PS composite films which were fabricated from PNIPAAm/PS/solvents (2 : 10 : 90 w/w/w). (a), (b), and (c) correspond to films IV, V, and VI in which the solvent of the precursor solution is DMF, CH_2Cl_2 , and THF, respectively.

10 wt% PS/DMF solution by electrospinning. The typical field emission scanning electron microscopy (FE-SEM) image of film I is shown in Figure 1(a). The numerous nanofibers with spindle beads are randomly oriented on the substrate which displays a network structure. Then, we investigated the wetting properties of film I. Film I is hydrophobic with a water CA of $140 \pm 4^\circ$ (inset of Figure 1(a)) which is much higher than the flat PS film owing to the rough structure of the as-prepared PS film. This result is corresponding to our previous work [18]. Afterwards, films II and III were fabricated from a 10 wt% solution of PS in CH_2Cl_2 and THF by the similar electrospinning process. Figure 1(b) shows the SEM image of film II which exhibits hierarchical structure with nanofibers and microparticles over the whole substrate. Figure 1(c) shows the SEM image of film III which displays numerous microparticles and a few nanofibers. We measured the wettability of the films with water CA of $144 \pm 4^\circ$ and $144 \pm 3^\circ$. These results show that the as-prepared electrospun PS films are all hydrophobic because of the rough surface and hierarchical structure. The minor difference in surface structure is due to the influence viscosity and volatility with polymer in different solvents. Also, it will not affect the intrinsic hydrophobic-hydrophilic properties of original materials. Therefore, in order to study the facility we set the same weight proportion of the polymeric precursor solution during the experiment below.

Then, PNIPAAm/PS/solvent solution (2 : 10 : 90 w/w/w) was used to fabricate composite films IV, V, and VI in which the solvents are DMF, CH_2Cl_2 , and THF, respectively. Figures 2(a), 2(b), and 2(c) show the typical SEM images of films IV, V, and VI. The morphology of the films is not completely identical with the same polymer composition. Concretely, the nanofibers are randomly oriented on the surface of film IV which has a network structure like a spider's web. Compared with the surface of film I, the spindle beads are instead of the numerous uniform nanofibers. It can be easily understood by the addition of PNIPAAm leading to the increase of the viscosity [19, 28]. The surface of film V (Figure 2(b)) is almost covered with nanofibers except for a few spindle beads. The microparticles in film II surface almost disappear in the surface of film V when adding PNIPAAm. Figure 2(c) is the SEM image of film VI showing numerous microspheres and nanofibers distributed densely over the surface. It is obvious that the amount of nanofibers increases compared with the SEM image of film III without PNIPAAm. Films IV, V, and VI are prepared with the same polymer composition by electrospinning from different PNIPAAm/PS/solvent precursor solutions. These SEM results show that the surface morphology is not completely uniform with the same polymer composition. The amount of the microspheres and nanofibers is distinct mainly by the reason of the viscosity of precursor solution with different

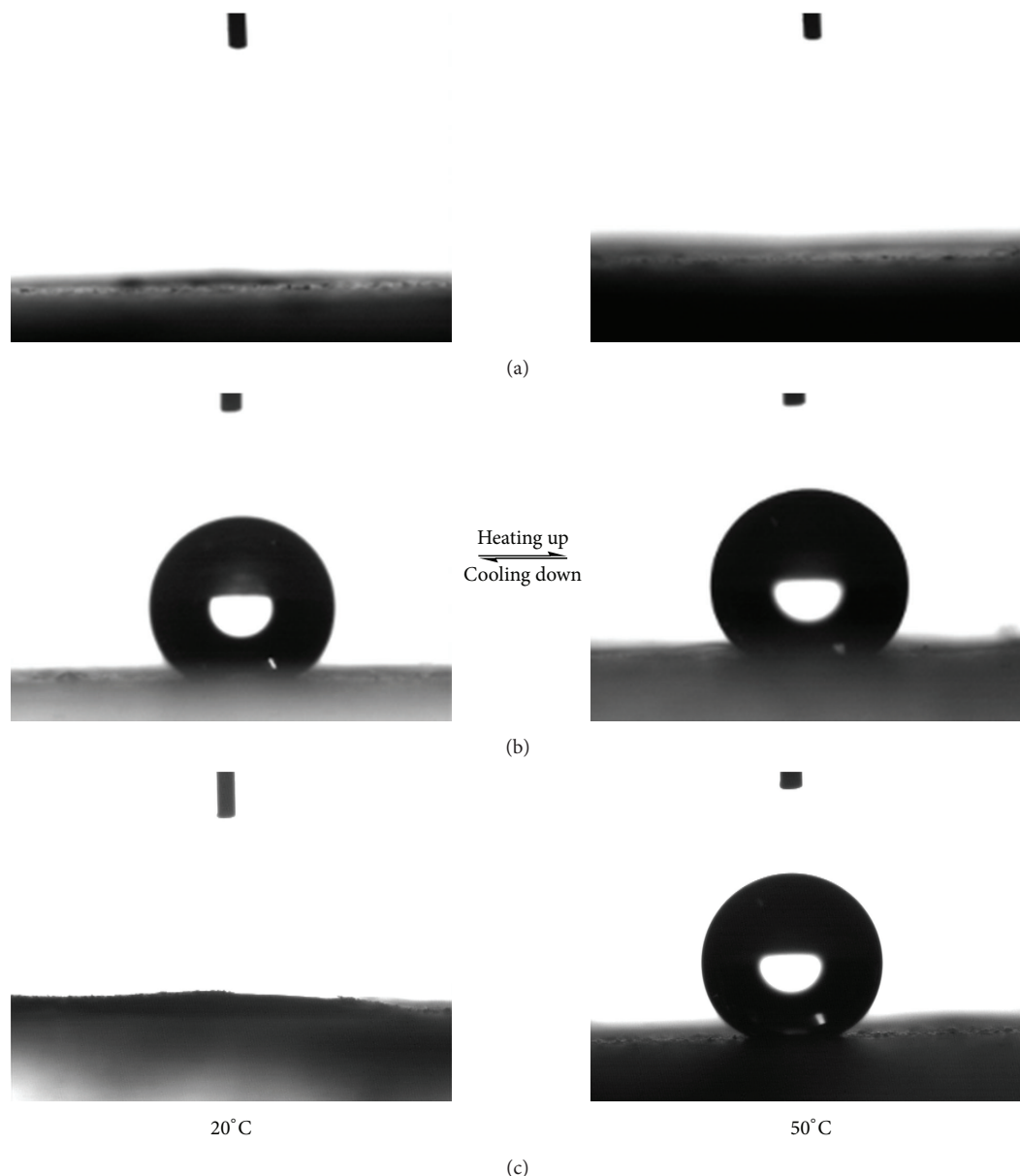


FIGURE 3: Photographs of water-droplet shape on the PNIPAAm/PS composite films at 20°C and 50°C. (a), (b), and (c) correspond to films IV, V, and VI in which the solvent of precursor solution is DMF, CH₂Cl₂, and THF, respectively. The wettability of PNIPAAm/PS composite films prepared from different precursor solutions is completely distinct when increasing the temperature. The wettability of the PNIPAAm/PS films is both superhydrophilic and superhydrophobic and switches from superhydrophilic to superhydrophobic according to the change in the temperature when the solvents are DMF, CH₂Cl₂, and THF, respectively.

solvents and evaporation of the solution droplets during electrospinning process [23–25].

Next, the wetting properties of films IV, V, and VI were investigated. At 20°C, the water CA of the films IV, V, and VI is about 0°, 133 ± 3°, and 6 ± 5°, respectively (Figure 3). Then, the water CA is 0°, 142 ± 5°, and 152 ± 3°, respectively, when the temperature is changed to 50°C (Figure 3). Surprisingly, the change of the water CA along with increasing the temperature is completely distinct. The as-prepared film IV, which was added to PNIPAAm in PS/DMF solution, is superhydrophilic according to heating

up the surface. Differently, the surface of film V from PNIPAAm/PS/CH₂Cl₂ precursor is hydrophobic along with the temperature alteration. While the water CA of the film VI from PNIPAAm/PS/THF precursor switched from 6 ± 5° to 152 ± 3°, the temperature changed from 20°C to 50°C.

It is well known that PNIPAAm is a thermoresponsive polymer which has fabricated many thermoresponsive materials by some methods [19, 29, 30]. The mechanism of the stimuli-responsive is explained by the competition between intermolecular and intramolecular hydrogen bonding below and above the lower critical solution temperature (LCST) of

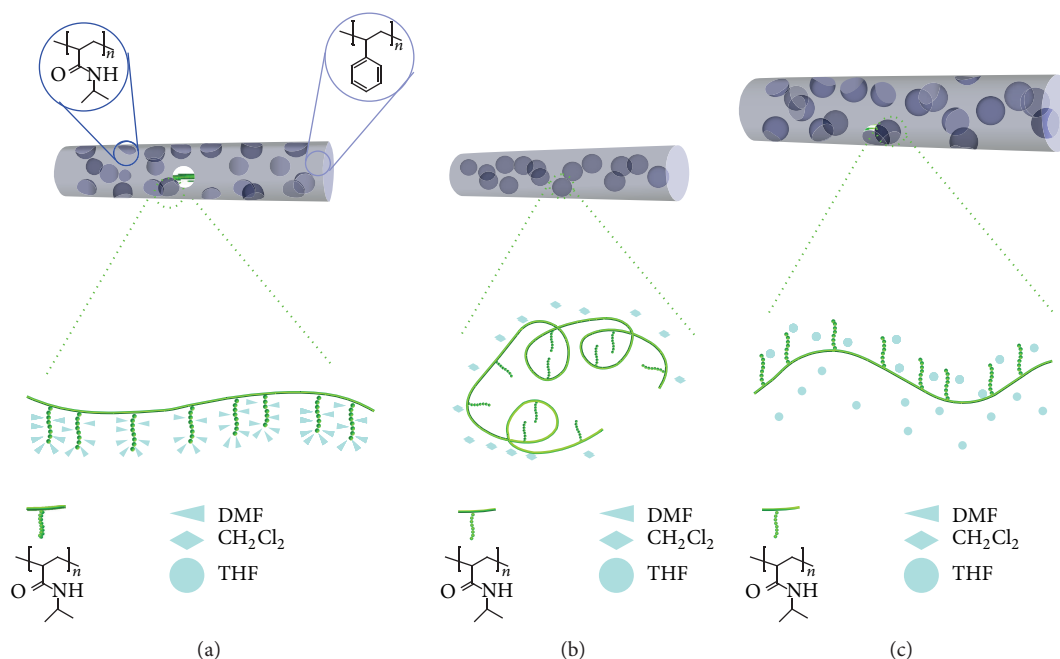


FIGURE 4: The diagram of mechanism of the various wetting properties of the as-prepared electrospun films. (a), (b), and (c) represent films IV, V, and VI in which the solvent of precursor solution is DMF, CH_2Cl_2 , and THF, respectively. PS mainly formed the fabric structures of the composited films, while the spheres which represent PNIPAAm are distributed differently in composite films IV, V, and VI. The chain diagram represents the idealized conformation between the PNIPAAm chain and solvent molecules in precursor solutions. The polar solvent DMF is likely to form intermolecular hydrogen bonding with PNIPAAm chain. Inversely, the PNIPAAm chain forms easily intramolecular hydrogen bonding when the nonpolar solvent CH_2Cl_2 is used. There is not evident hydrogen bonding interaction in the PNIPAAm/PS/THF precursor solution.

about 32 to 33° [31–33]. The fantastic wettability alteration of PNIPAAm/PS surface has been studied in our previous work and has been explained by the combination of the individual properties of PS and PNIPAAm with the appropriate surface roughness of the film [19]. The PNIPAAm/PS surface exhibits reversible superhydrophilicity and superhydrophobicity by changing the temperature due to freely swell and shrink of the PNIPAAm chains. However, the further results above give us a new assumption that the solvent plays a significant role in the transformation from precursor solution into microspheres/nanofibers through the process of electrospinning.

Figure 4 outlines the proposed mechanism of various wetting property of the as-prepared electrospun films. The fabric structure of the film is mainly made from PS as a result of the majority proportion of precursor solution. While the spheres which represent PNIPAAm are distributed distinctly in various films IV, V and VI, the chain diagram represents the idealized conformation between the PNIPAAm chain and solvent molecules in precursor solutions. As shown in Figure 4(a), DMF is a kind of familiar polar solvent and the value of polarity is 6.4. So in the mixture solution of PNIPAAm, PS, and DMF, the polar C=O and N–H groups in the PNIPAAm chain interact easily with the DMF molecules to form intermolecular hydrogen bonding. At the same time, the nonpolar C–H group in the PNIPAAm and PS tend to intertwist together. Then, in the transformation from polymer precursor solution to fibers with rapid solvent evaporation during electrospinning, the PNIPAAm chain is easily distributed on the surface of the fibers with the

polar C=O and N–H groups barely. Although there are hydrophobic C–H groups of PS molecules surrounding the PNIPAAm molecules, the water drops can still move across the PS molecules and interact with C=O and N–H groups to form intermolecular hydrogen bonding. Therefore, the as-prepared film IV exhibits superhydrophilicity with the water CA of 0° at 20°C . Then, when the temperature is changed to 50°C , the PNIPAAm chain cannot go around freely which results in the C=O and N–H groups still exhibiting the surface of the film. Consequently, the film IV is still superhydrophilic with the water CA of 0° when heating up the surface. Surprisingly, the wettability of film V from PNIPAAm/PS/ CH_2Cl_2 precursor solution is completely different according to heating up the surface. The as-prepared film V is superhydrophobic both before and after increasing the temperature. It is well known that CH_2Cl_2 is a kind of nonpolar solvent and the value of polarity is 3.4. Both the C–H groups in PNIPAAm and PS will interact with CH_2Cl_2 molecular easily in the dissolution process (Figure 4(b)). Hence, the PNIPAAm chain is apt to shrink to form intramolecular hydrogen bonding between the C=O and N–H groups. After the process of electrospinning with rapid solvent evaporation, most of the fibers surface is occupied by hydrophobic C–H groups which accords with the water CA of $133 \pm 3^\circ$. When the temperature is raised above the LCST, the PNIPAAm chain more easily shrinks to form of a compact and collapsed conformation. Thus, the film V shows hydrophobicity with the water CA of $142 \pm 5^\circ$ at high temperature. Besides, the wettability of

film VI can be switched between superhydrophilicity and superhydrophobicity when changing the temperature. The polarity value of THF is 4.2 which is between DMF and CH_2Cl_2 and results in the fact that the PNIPAAm chain could distribute more freely in the PNIPAAm/PS/THF precursor solution (Figure 4(c)). Noticeably, the PNIPAAm chain could still swell and shrink freely on the surface of as-prepared film VI. So the wettability of film VI could be explained by the competition between intermolecular and intramolecular hydrogen bonding in PNIPAAm chain according to changing the temperature which have been studied in detail in our previous work [19].

Therefore, solvents play an extraordinary important role in the transformation from precursor polymer solutions to fibers which induce different physicochemical properties of the surface. In this work, the polar solvent DMF is likely to form intermolecular hydrogen bonding with PNIPAAm chain in precursor solution. The C=O and N-H groups are easily bared on the surface of the film. So the film IV is superhydrophilic both before and after increasing the temperature. Inversely, the PNIPAAm chain seems more favorable to form intramolecular hydrogen bonding when nonpolar solvent CH_2Cl_2 is used. And film V is hydrophobic when changing the temperature because most of the surface is occupied by C-H groups. The polarity of THF is between DMF and CH_2Cl_2 ; thus, there is no evident hydrogen bonding interaction in the PNIPAAm/PS/THF solution (Figure 4(c)). The PNIPAAm molecular could freely extend and shrink before and after increasing the temperature. The film VI could switch between superhydrophilicity and superhydrophobicity when the temperature is changed from 20°C to 50°C.

4. Conclusion

Variable responsive wettability films were fabricated by electrospinning by the result of solvents induced distinct distribution of hydrophilic groups and hydrophobic groups. Three kinds of PNIPAAm/PS films with the same polymer composition present extremely different wettability performance. The wettability of the PNIPAAm/PS films is both superhydrophilic and superhydrophobic and switches from superhydrophilic to superhydrophobic according to change in temperature when the precursor solvents are DMF, CH_2Cl_2 , and THF, respectively. It could be explained by the competition between intermolecular hydrogen bonding and intramolecular hydrogen bonding in solutions with different solvents. It is the first example to fabricate composite films with same polymer composition but different properties by electrospinning. It gives us an inspiration that new functional and structure materials could be created with proper substance and solvent. It is quite important for the electrospinning research about the solvent induced factors and lays a foundation for the further application of electrospinning.

Conflict of Interests

The authors declare that there is no conflict of interests regarding the publication of this paper.

Acknowledgments

The authors acknowledge the Natural Science Foundation of China (21374001, 21222309, 21134003, and 21071148), 973 Program (2012CB933200, 2010CB934700, and 2009CB930404), 863 Program (2012AA030305), and Program for New Century Excellent Talents in University of China for continuous financial support.

References

- [1] X. Yao, Y. Song, and L. Jiang, "Applications of bio-inspired special wettable surfaces," *Advanced Materials*, vol. 23, no. 6, pp. 719–734, 2011.
- [2] D. Quéré, "Wetting and roughness," *Annual Review of Materials Research*, vol. 38, no. 1, pp. 71–99, 2008.
- [3] F. Xia, Y. Zhu, L. Feng, and L. Jiang, "Smart responsive surfaces switching reversibly between super-hydrophobicity and superhydrophilicity," *Soft Matter*, vol. 5, no. 2, pp. 275–281, 2009.
- [4] K. Liu and L. Jiang, "Metallic surfaces with special wettability," *Nanoscale*, vol. 3, no. 3, pp. 825–838, 2011.
- [5] X.-M. Li, D. Reinhoudt, and M. Crego-Calama, "What do we need for a superhydrophobic surface? A review on the recent progress in the preparation of superhydrophobic surfaces," *Chemical Society Reviews*, vol. 36, no. 8, pp. 1350–1368, 2007.
- [6] P. Roach, N. J. Shirtcliffe, and M. I. Newton, "Progress in superhydrophobic surface development," *Soft Matter*, vol. 4, no. 2, p. 224, 2008.
- [7] J. Drelich, E. Chibowski, D. D. Meng, and K. Terpilowski, "Hydrophilic and superhydrophilic surfaces and materials," *Soft Matter*, vol. 7, no. 21, pp. 9804–9828, 2011.
- [8] T. Onda, S. Shibuichi, N. Satoh, and K. Tsujii, "Super-water-repellent fractal surfaces," *Langmuir*, vol. 12, no. 9, pp. 2125–2127, 1996.
- [9] W. Chen, A. Y. Fadeev, M. C. Hsieh, D. Öner, J. Youngblood, and T. J. McCarthy, "Ultrasuperhydrophobic and ultrasuperoleophobic surfaces: some comments and examples," *Langmuir*, vol. 15, no. 10, pp. 3395–3399, 1999.
- [10] J. Bico, C. Tordeux, and D. Quéré, "Rough wetting," *Europhysics Letters*, vol. 55, no. 2, pp. 214–220, 2001.
- [11] X. Zhang, F. Shi, J. Niu, Y. Jiang, and Z. Wang, "Superhydrophobic surfaces: from structural control to functional application," *Journal of Materials Chemistry*, vol. 18, no. 6, pp. 621–633, 2008.
- [12] H. Y. Erbil, A. L. Demirel, Y. Avci, and O. Mert, "Transformation of a simple plastic into a superhydrophobic surface," *Science*, vol. 299, no. 5611, pp. 1377–1380, 2003.
- [13] J. Wu, N. Wang, H. Zhang et al., "Acrylic acid grafted porous polycarbonate membrane with smart hydrostatic pressure response to pH," *Journal of Materials Chemistry A*, vol. 1, no. 15, pp. 4642–4646, 2013.
- [14] S. Minko, M. Müller, M. Motornov, M. Nitschke, K. Grundke, and M. Stamm, "Two-level structured self-adaptive surfaces with reversibly tunable properties," *Journal of the American Chemical Society*, vol. 125, no. 13, pp. 3896–3900, 2003.
- [15] N. J. Shirtcliffe, G. McHale, M. I. Newton, C. C. Perry, and P. Roach, "Porous materials show superhydrophobic to superhydrophilic switching," *Chemical Communications*, no. 25, pp. 3135–3137, 2005.
- [16] N. L. Abbott, C. B. Gorman, and G. M. Whitesides, "Active control of wetting using applied electrical potentials and self-assembled monolayers," *Langmuir*, vol. 11, no. 1, pp. 16–18, 1995.

- [17] L. Xu, W. Chen, A. Mulchandani, and Y. Yan, "Reversible conversion of conducting polymer films from superhydrophobic to superhydrophilic," *Angewandte Chemie*, vol. 44, no. 37, pp. 6009–6012, 2005.
- [18] L. Jiang, Y. Zhao, and J. Zhai, "A lotus-leaf-like superhydrophobic surface: a porous microsphere/nanofiber composite film prepared by electrohydrodynamics," *Angewandte Chemie*, vol. 43, no. 33, pp. 4338–4341, 2004.
- [19] N. Wang, Y. Zhao, and L. Jiang, "Low-cost, thermoresponsive wettability of surfaces: poly(N-isopropylacrylamide)/polystyrene composite films prepared by electrospinning," *Macromolecular Rapid Communications*, vol. 29, no. 6, pp. 485–489, 2008.
- [20] X. Lu, J. Peng, B. Li, C. Zhang, and Y. Han, "A polymer composite film with reversible responsive behaviors," *Macromolecular Rapid Communications*, vol. 27, no. 2, pp. 136–141, 2006.
- [21] D. Li and Y. Xia, "Electrospinning of nanofibers: reinventing the wheel?" *Advanced Materials*, vol. 16, no. 14, pp. 1151–1170, 2004.
- [22] X. Lu, C. Wang, and Y. Wei, "One-dimensional composite nanomaterials: synthesis by electrospinning and their applications," *Small*, vol. 5, no. 21, pp. 2349–2370, 2009.
- [23] Z.-M. Huang, Y.-Z. Zhang, M. Kotaki, and S. Ramakrishna, "A review on polymer nanofibers by electrospinning and their applications in nanocomposites," *Composites Science and Technology*, vol. 63, no. 15, pp. 2223–2253, 2003.
- [24] S. Megelski, J. S. Stephens, D. Bruce Chase, and J. F. Rabolt, "Micro- and nanostructured surface morphology on electrospun polymer fibers," *Macromolecules*, vol. 35, no. 22, pp. 8456–8466, 2002.
- [25] K. H. Lee, H. Y. Kim, M. S. Khil, Y. M. Ra, and D. R. Lee, "Characterization of nano-structured poly(ϵ -caprolactone) nonwoven mats via electrospinning," *Polymer*, vol. 44, no. 4, pp. 1287–1294, 2003.
- [26] L. Moroni, R. Licht, J. de Boer, J. R. de Wijn, and C. A. van Blitterswijk, "Fiber diameter and texture of electrospun PEOT/PBT scaffolds influence human mesenchymal stem cell proliferation and morphology, and the release of incorporated compounds," *Biomaterials*, vol. 27, no. 28, pp. 4911–4922, 2006.
- [27] J. Doshi and D. H. Reneker, "Electrospinning process and applications of electrospun fibers," *Journal of Electrostatics*, vol. 35, no. 2-3, pp. 151–160, 1995.
- [28] H. Fong, I. Chun, and D. H. Reneker, "Beaded nanofibers formed during electrospinning," *Polymer*, vol. 40, no. 16, pp. 4585–4592, 1999.
- [29] T. Sun, G. Wang, L. Feng et al., "Reversible Switching between Superhydrophilicity and Superhydrophobicity," *Angewandte Chemie*, vol. 43, no. 3, pp. 357–360, 2004.
- [30] L. Chen, M. Liu, H. Bai et al., "Antiplaetlet and thermally responsive poly(N-isopropylacrylamide) surface with nanoscale topography," *Journal of the American Chemical Society*, vol. 131, no. 30, pp. 10467–10472, 2009.
- [31] Y. G. Takei, T. Aoki, K. Sanui, N. Ogata, Y. Sakurai, and T. Okano, "Dynamic contact angle measurement of temperature-responsive surface properties for poly(N-isopropylacrylamide) grafted surfaces," *Macromolecules*, vol. 27, no. 21, pp. 6163–6166, 1994.
- [32] T. Yakushiji, K. Sakai, A. Kikuchi, T. Aoyagi, Y. Sakurai, and T. Okano, "Graft architectural effects on thermoresponsive wettability changes of poly(N-isopropylacrylamide)-modified surfaces," *Langmuir*, vol. 14, no. 16, pp. 4657–4662, 1998.
- [33] L. Liang, P. C. Rieke, J. Liu et al., "Surfaces with reversible hydrophilic/hydrophobic characteristics on cross-linked poly(N-isopropylacrylamide) hydrogels," *Langmuir*, vol. 16, no. 21, pp. 8016–8023, 2000.